MEASUREMENTS OF THE STATIC AND DYNAMIC FORCE PERFORMANCE ON A FIVE-PAD, SPHERICAL-PIVOT TILTING-PAD JOURNAL BEARING: INFLUENCE OF OIL FLOW RATE

A Thesis

by

HARDIK YOMESH JANI

Submitted to the Office of Graduate and Professional Studies of
Texas A&M University
in partial fulfillment of the requirements for the degree of

MASTER OF SCIENCE

Chair of Committee,	Luis A. San Andrés
Committee Members,	Adolfo Delgado
	Stefan Hurlebaus
Head of Department,	Andreas A. Polycarpou

August 2018

Major Subject: Mechanical Engineering

ABSTRACT

Tilting-pad journal bearings (TPJB) are commonly utilized to support rotors in high-speed rotating machinery. They can provide significant load capacity, reduced drag power loss, and a stable high-speed operation. Over the years, the design of TPJBs has developed to satisfy various performance needs. However, bearing pad high metal temperatures and drag power loss are a matter of concern to support the growing industry demand for high power capacity and efficient machines. For certain conditions involving lightly loaded bearing and/or evacuated housing configuration, TPJBs operate with a reduced oil flow rate which may cause subsynchronous rotor vibration (SSV) hash. In the past, many investigated the influence of supplied oil flow rate on the bearing steady-state characteristics; however, test data for the impact on its dynamic forced performance are scarce.

This thesis presents and discusses the measurements of the static and dynamic forced performance of a TPJB under load-between-pad (LBP) orientation in the floating bearing test rig. In addition, it also discusses the influence of reduced supply oil flow rate (27% and 50% of nominal) and increased supply oil flow rate (150% of nominal) on the bearing static and dynamic forced properties. The test bearing has the following design characteristics: five pads, ball-in-socket (spherical) pivots, L/D = 0.4, pivot offset = 50%, clearance to radius ratio (C_r/R) ≈ 0.0013, preload = 0.42, and pressurized flooded housing (with end seals). The operating test conditions include six shaft surface speeds (15-85 m/s) and seven specific loads (0.17 to 2.1 MPa). ISO VG 32 lubricates the test bearing with speed-dependent flow rate (100% nominal flow = 3.65 to 19.45 Lit/m) and at supply temperature of 49°C.

The bearing steady-state performance parameters include the journal static equilibrium position, attitude angle, oil temperature rise, pad temperature rise, and drag power loss. The experimental drag power loss is obtained by two methods: (1) a direct measurement of drag torque and shaft angular speed, and (2) an estimation based on the oil flow rate and the oil temperature rise at the bearing exit plane. The dynamic forced performance

parameters include rotordynamic force coefficients (stiffness, damping, and virtual-mass) obtained by a multi-frequency dynamic force excitation. Some of the test results are in a dimensionless form to characterize a general trend for TPJBs.

The direct drag power loss is lower by ≈ 20% as compared to the estimated drag power loss for most operating conditions. Interestingly, the measured drag power loss is less dependent on the supplied oil flow rate as compared to the estimated drag power loss. A reduction in oil flow rate up to 50% of nominal magnitude causes an increase in the measured shaft eccentricity, pad temperature up to 6°C and direct stiffness coefficient up to 5%, and a decrease in measured drag power loss up to 15% and direct damping coefficient up to 7%. For a single case of operation with 27% of nominal flow rate, the pad temperature significantly increases up to 15°C and direct damping drastically reduces up to 16%; however, the supplied oil temperature increases by 13°C which falls outside of standard operating conditions. The test bearing operates safely (no significant pad temperature rise) at reduced oil flow rate (by 50% and 73% of nominal) for operation up to 14 krpm (74m/s). Thus, a low oil flow rate only causes a slight degradation in the bearing's static and dynamic forced performance. Furthermore, an increase in supplied oil flow rate causes a slight increase in drag power loss and direct damping up to 10%, a slight decrease in direct stiffness up to 5%, an insignificant increase in shaft eccentricity up to 9% and pad temperatures up to 3°C.

Lastly, this thesis presents a comparison of the experimental test data with predictions from the XLTPJB® model. The model under predicts the journal eccentricity, over predicts the drag power loss and predicts well the maximum pad temperature (for > 12 krpm). For dynamic forced performance, the model predicts well the stiffness and damping coefficients at low Sommerfeld number ($S < 2$) and under predicts the force coefficients for $S > 2$.

DEDICATION

To everyone who cared and supported me.

ACKNOWLEDGEMENTS

I sincerely thank Dr. Luis San Andrés for giving me an opportunity to work at the Turbomachinery Laboratory, and for providing honest support and guidance from the very beginning. I thank Elliott Group for the financial support and allowing to use the test data for the thesis. I will always remember the patience and encouragement shown by Dr. San Andrés and seniors at Elliott during the difficult times. I am also grateful to Manish Thorat of Elliott Group for providing valuable feedback on the thesis.

I am grateful to Dr. Childs, the committee members, Dr. Delgado and Dr. Hurlebaus, and other faculties at Texas A&M who have made this journey worthwhile. I also like to thank all the colleagues and friends at the Turbo Lab especially Hussain, Xuliang, Bonjin, Behzad, Travis, Scott, Jonathan, Trevor, Ovais and Lab manager Carl who made this experience enjoyable and knowledgeable. Lastly, I want to thank my wife, parents, in-laws, and all my family for their love and encouragement.

CONTRIBUTORS AND FUNDING SOURCES

Contributors

This work was supported by the sponsored company Elliott Group, Professor Luis San Andrés and Professor Dara Childs of the Department of Mechanical Engineering.

The students at Turbomachinery Laboratory supported to conduct experiments for this study. Professor Luis San Andrés helped and guided this work and thesis in appropriate direction.

All other work conducted for the thesis was completed by the student independently.

Funding Sources

Graduate study was supported by the sponsored company Elliott Group.

TABLE OF CONTENTS

LIST OF FIGURES

Page

LIST OF TABLES

Page

NOMENCLATURE

A_{ij}	Discrete Fourier Transform (DFT) of the stator acceleration [m/s^2]
C_d	Diametrical bearing clearance [m]
C_{ij}	Direct and cross-coupled damping coefficients [Ns/m]
c_{ij}	Dimensionless damping coefficients
C_{gr}	Groove mixing coefficient
C_p	Radial pad clearance [m]
C_r	Radial bearing clearance [m]
C_s	End seal clearance [m]
D	Bearing diameter [m]
D_{ij}	DFT of the relative rotor-bearing displacement [m]
e	Journal eccentricity [m]
e_x, e_y	Journal eccentricity along x and y axis [m]
f_{bx}, f_{by}	Bearing fluid film reaction forces along x and y axis [N]
f_{dx}, f_{dy}	Dynamic excitation force [N]
F_{ij}	DFT of excitation force on bearing [N]
H_{ij}	Complex dynamic stiffness [N/m]
i	Imaginary unit ($\sqrt{-1}$)
K_{ij}	Direct and cross-coupled stiffness coefficients [N/m]
k_{ij}	Dimensionless stiffness coefficients
K_p	Pivot stiffness [N/m]
L	Bearing pad axial length [m]
M_{bx}, M_{bx}	Mass of bearing and stator [kg]
M_{ij}	Direct and cross-coupled virtual-mass coefficients [kg]
m	pad preload
m_{ij}	Dimensionless virtual-mass coefficients
N	Rotor running speed (Rev/s)
n_p	Number of pads
P	Drag power-loss
$\overline{P}$	Dimensionless drag power-loss
$\dot{Q}$	Lubricant supply flow rate to bearing feed grooves [m^3/s, Lit/s]

R	Journal radius [m]
S	Sommerfeld number
T	Temperature [ºC]
W	Applied static load [N]
α	Pivot offset
α_x, α_y	Bearing stator acceleration along x and y axis [m/s^2]
Δx, Δy	Bearing and rotor relative displacement [m]
μ	Fluid viscosity [Pa.s]
κ	Empirical coefficient denoting amount of heat carried by lubricant
θ	Pad Defect Temperature [ºC]
θ_P	Pad Arclength [deg]
φ	Attitude angle [degree]
ω	Excitation frequency [Hz]
Ω	Rotor running frequency [Hz, rpm]
λ	Hot oil carry-over coefficient

Abbreviations

CC	*Cold* Clearance
DE	Drive End
DFT	Discrete Fourier Transform
HC	*Hot* Clearance
KCM	Stiffness, Damping and Virtual-Mass model
LBP	Load between Pads
LEG	Leading edge groove
LOP	Load on Pad
LPM	Liters per minute
NDE	Non-Drive End
R-B	Rotor-Bearing system
SB	Spray Bar
SBB	Spray Bar with Blocker
SO	Single Orifice
SSV	Subsynchronous Speed Vibration
TEHD	Thermo-Elasto-Hydro-Dynamic
TPJB	Tilting-Pad Journal Bearing

1. INTRODUCTION

In rotating equipment, hydrodynamic fluid-film journal bearings support a (flexible) rotor that may cross multiple critical speeds to achieve its operating condition. A supercritical rotor supported on fixed-geometry journal bearings becomes unstable at a shaft angular speed equal to or greater than twice the natural frequency of the rotor-bearing (R-B) system due to a self-excited phenomenon called oil-whirl and oil-whip [1, 2]. Tilting-pad journal bearings (TPJBs) have significant direct stiffness and damping coefficients, and with nearly null cross-coupling stiffness lead to a stable R-B system [1]. In 1904, Michell (line pivot) and in 1907, Kingsbury (point pivot) independently invented the tilting-pad bearing to carry thrust loads. Presently, radial TPJBs have a broad application in high-speed compressors, steam and gas turbines, pumps, gearboxes, and other rotating machinery equipment.

In a hydrodynamic journal bearing, a spinning rotor drags lubricant into a small converging gap between the rotor and bearing to support the rotor weight through a generated hydrodynamic film pressure. The load capacity in bearings depends on the rotor surface speed, film thickness, lubricant viscosity, and bearing geometry [1]. As shown in Figure 1, a TPJB comprises a number of arcuate pads or segments, typically three to six, or more depending on the application size. Unlike fixed-geometry journal bearings, each pad in a TPJB is free to rotate about its pivot.

Due to cross-coupling forces in journal bearings, rotor experiences displacements orthogonal to the applied load. Such cross-coupled forces add energy to the shaft forward whirling motion and may destabilize the R-B system [1]. On the contrary, the net moment about a pivot in TPJBs is zero due to the tilting motion of each pad, when oriented as shown in Fig. 1, and thus reduce an orthogonal rotor movement. However, a rotor supported by TPJBs can become unstable due to other mechanisms such as seals and aerodynamic forces. Hence, the knowledge of bearing rotordynamic coefficients (stiffness and damping) is essential to determine the critical speeds, synchronous response to imbalance, and stability of the R-B system [2].

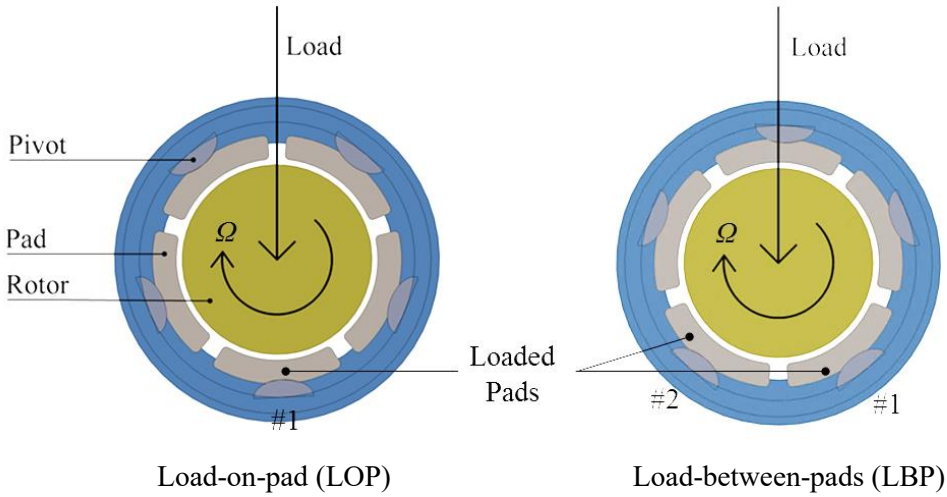

Figure 1. Schematic diagrams of five-pad tilting-pad journal bearings in two common arrangements (a) Load-on-pad (LOP) and (b) Load-between-pads (LBP).

For small amplitude rotor motions about an equilibrium position, a linearized spring, damper, and mass (K-C-M) model represents a reaction force in an oil-film bearing as,

$$-\begin{bmatrix} f_{bx} \\ f_{by} \end{bmatrix} = \begin{bmatrix} K_{xx} & K_{xy} \\ K_{yx} & K_{yy} \end{bmatrix} \begin{Bmatrix} \Delta x \\ \Delta y \end{Bmatrix} + \begin{bmatrix} C_{xx} & C_{xy} \\ C_{yx} & C_{yy} \end{bmatrix} \begin{Bmatrix} \Delta \dot{x} \\ \Delta \dot{y} \end{Bmatrix} + \begin{bmatrix} M_{xx} & M_{xy} \\ M_{yx} & M_{yy} \end{bmatrix} \begin{Bmatrix} \Delta \ddot{x} \\ \Delta \ddot{y} \end{Bmatrix} \quad (1)$$

where (Δx, Δy) are the relative rotor-bearing displacement, and (f_{bx}, f_{by}) are the bearing reaction force components. The terminology x and y refer to displacements and forces along the x (non-load) and y (load) axes, respectively. The diagonal terms K_{ii}, $C_{ii,}$ and M_{ii} (i=x,y) represent the direct force coefficients that generate a reaction force opposing shaft motion along the same direction i.e. K_{xx} (= $-\Delta f_{bx}/\Delta x$). The off-diagonal terms K_{ij}, $C_{ij,}$ and M_{ij} ($i \neq j$) represent cross-coupled coefficients that generate a reaction force orthogonal to the shaft motion. For example, K_{xy} (= $-\Delta f_{bx}/\Delta y$) refers to the stiffness along the x-axis due to a load along the y-axis.

The design of TPJBs has many choices to suit various applications and requirements. Figure 2 depicts a schematic diagram of the geometric design parameters in a typical TPJB. Each design parameter significantly influences the steady-state performance

characteristics such as drag power loss, pad temperatures, and film thickness, and also the dynamic force characteristics such as stiffness and damping. Many researchers have examined the effect of pad preload and clearance, pivot type and offset, load orientation, lubrication method, number of pads, slenderness (*L/D*) ratio, and pad material on the static and dynamic force characteristics of TPJBs, see Refs. [3-7].

Rotor Radius	R_s
Bearing Center	B
Bearing Radius	R_b
Pad Center	P
Pad Radius	R_p
Pivot Arc Angle	θ_{PIVOT}
Pad Arc Angle	θ_{PAD}

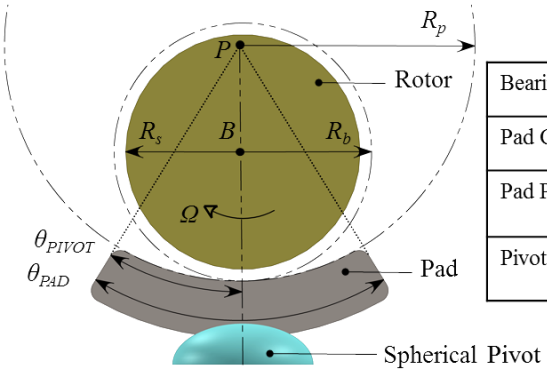

Bearing Clearance (C_b)	$R_b - Rs$
Pad Clearance (C_p)	$R_p - R_s$
Pad Preload (m_b)	$1 - \frac{C_b}{C_p}$
Pivot Offset (α)	$\frac{\theta_{PIVOT}}{\theta_{PAD}}$

Figure 2. Schematic view of a typical pad in TPJB and its geometric parameters.

Figures 2 and 3 present three common pivot types in TPJBs such as ball-in-socket (spherical), rocker-back, and flexure pivot. The ball-in-socket pivot design has a ball (pivot) fixed to a housing of the same size as a socket machined on the back of a pad. The spherical pivot, see Fig. 2, allows tilting (sliding) motion of the pad along two directions (circumferential and axial). The motion in the axial direction allows for shaft misalignment. The rocker-back pivot (line contact) pad, see Fig. 3, has a cylindrical key seat affixed to it's back which allows rolling motion only along the circumferential direction. The spherical pivot has a higher sliding friction force compared to the rocker pivot due to the larger surface contact and tends to lock at high bearing loads [1, 7]. Ref. [7] details the design and influence of the spherical and rocket pivot types on TPJB performance. Flexure pivot has a flexural web machined between pads and bearing housing, and which allows limited tilting of the pad. The flexure pivot bearings are well-known in small and large size rotor applications to avoid tolerance stack-up which is common in TPJBs [8, 9].

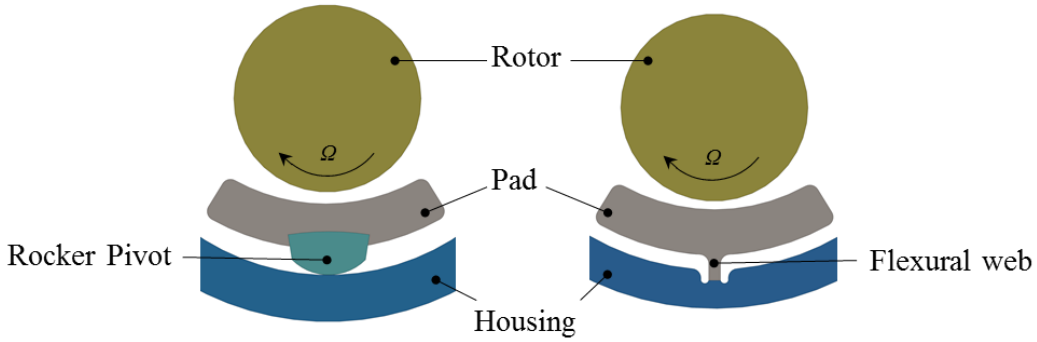

Figure 3. Two common pivot types: rocket pivot and flexure pivot.

Due to operation at increasing shaft surface speeds, shear drag power loss and bearing pads' temperatures also increase. These conditions limit bearings' operation to make them inefficient [4]. A sufficient amount of oil supply flow keeps the bearing pad temperature within an acceptable limit. However, an excess oil flow (in an over flooded bearing) moves out axially or to a sump below the pad to produce churning losses and without effectively cooling the bearing pads. On the other hand, a reduction in oil flow rate results in a lower drag power loss and pumping costs but with a risk of high pad temperatures and oil starvation of the bearing pads. The hot oil carry-over from an upstream pad to a downstream pad increases when the supplied fresh oil flow rate reduces, thus also raising the pad temperature. Moreover, oil starvation in bearing pads can degrade bearing dynamic force coefficients and can produce subsynchronous speed rotor vibrations (SSV) [10, 11]. A bearing with a direct lubrication[1] method is likely to have oil starvation due to the absence of an additional oil in the housing (sump) like that in a flooded configuration bearing [10]. A reduced oil flow rate into a TPJB with either lubrication method, flooded or direct, has a significant influence on the bearing stiffness and damping coefficients along with the bearing steady-state characteristics [10]. The current industry trend moves

[1] Direct lubrication method refers to a design where oil is delivered closer to a pad's leading edge by some mechanism such as nozzle, spray bar, or leading-edge groove on pad.

towards increasing power delivery with greater mechanical efficiency, and hence to supply a minimal amount of oil to a bearing without affecting its performance is essential.

2. OBJECTIVE

The present work experimentally investigates the static and dynamic forced performance of a ball-in-socket (spherical) pivot, five-pad tilting-pad journal bearing for a compressor application. In particular, the study focuses on the following tasks:

1. Measurement of the bearing steady-state characteristics such as shaft eccentricity, attitude angle, pads' temperature, oil supply and exit temperature, and drag power loss and also the dynamic parameters like stiffness, damping and added-mass coefficients over a set of excitation frequencies (10-300 Hz). The test bearing has five pads, ball-in-socket (spherical) pivots, 50% pivot offset, smooth end-seals with diametral clearance of 0.57 mm on each side of bearing, a nominal diametral bearing clearance (C_d) of 0.125 mm, slenderness ratio (L/D) of 0.4, and a mean pad preload of 0.42 as listed in Table 1. The operating conditions include six shaft speeds (16 to 85 m/s), seven specific loads[2] (0.17 to 2.1 MPa), and speed-dependent oil flow rate as detailed in Table 2. The lubricant for the bearing is a light turbine oil ISO VG 32 supplied at an inlet temperature of 49℃.

   Most prior experimental works present bearing drag power loss based on the global temperature rise of the lubricant. The current study conducted a direct measurement of the drag torque for accurate calculation of the drag power loss.
2. Quantify the effects of a both reduced (27%-50%) and increased (150%) oil supply flow rate on the steady-state as well as dynamic performance parameters of the test TPJB. This study focuses only on specific operating conditions[3] to examine the influence of the oil supply flow rate, as shown in Table 2.
3. Comparison of the experimental results against predictions from XLTPJB® [12] bearing model. The prediction model can account for both pad and pivot flexibility,

[2] The bearing specific load equals the applied static load (W) divided by the bearing projected area (L x D).
[3] The test conditions marked with an asterisk (*) in Table 2.

includes temporal fluid inertia effects in the film, thermal induced pad deflection, and an improved feed groove thermal mixing coefficient based on flow demand.

Table 1. Test bearing geometry, lubricant properties and operating conditions.

Bearing Geometry	
Load Orientation	Load-between-pads (LBP)
Number of Pads	Five
Pivot Type	Ball-in-socket
Shaft diameter, D	101.590 ± 0.005 mm
Bearing axial length, L	41 mm
Slenderness ratio (L/D)	0.4
Pad arc length	63°
Pad material	Steel
Pad mass	0.25 kg
Pad moment of inertia about pivot	1.14 kg.cm^2
Pivot offset	50%
Preload (m)	0.42 (± 0.03)
Pad nominal radial clearance (C_p)	0.112 ± 0.005 mm
Bearing nominal radial clearance (C_r)	0.0625 ± 0.00025 mm
End seal diametric clearance (C_s)	0.570 mm
Fluid Properties	
Lubricant	ISO VG 32
Viscosity at supply temperature 49°C, μ	19.7 mPa.s
Viscosity temperature coefficient	0.0296/°C
Density @ 49°C	851 kg/m^3
Specific heat capacity @ 49°C	1980 kJ/(kg.K)
Nominal inlet oil temperature	49°C (120°F)
Lubricant supply configuration	Flooded (pressurized)
Oil insert type	Orifice
Operating Conditions	
Applied load range, W	710 - 8540 N (160 - 1920 lbf)
Specific load range, $W/(LD)$	0.17 – 2.1 MPa (25 - 300 psi)
Rotor speed range, Ω	3k - 16k rpm
Surface speed, ½ Ω D	16 - 85 m/s

Table 2. Matrix of tests for the experimental investigation.

Speed-dependent oil flow rate (LPM) →	27%	-	-	-	✓	-	-
	50%	-	-	✓	✓	✓	-
	100%	✓	✓	✓	✓	✓	✓
	150%	-	-	✓	✓	✓	-
Target rotor speed (Ω)→	RPM	3000	6000	9000	12000	14000	16000
Target surface speed (ΩR) →	m/s	16	32	48	64	74	85
Target applied specific load $W/(LD)$ (MPa) →	0.17	✓	✓	✓	✓	✓	✓
	0.34	✓	✓	✓*	✓*	✓*	✓
	0.69	✓	✓	✓*	✓*	✓*	✓
	1.03	✓	✓	✓*	✓*	✓*	✓
	1.38	✓	✓	✓	✓	✓	
	1.72	✓	✓	✓	✓		
	2.07		✓	✓	✓		

3. PAST LITERATURE REVIEW

There are numerous papers discussing measurements of the steady-state and dynamic forced characteristics of various TPJB design configurations. This review discusses literature relevant to the experimental work on TPJB configuration similar to the one in the current study.

In a conventional rotordynamic analysis, frequency reduced stiffness and damping coefficients of the TPJB are commonly considered at a frequency equal to shaft angular speed (1x) i.e. synchronous speed. However, the TPJB force coefficients could be different at the damped natural frequency of the system. Henceforth, researchers began to explore non-synchronous shaft speed excitation methods to study the frequency dependency of the force coefficients. In 1999, Ha and Yang [13] use hydraulic shakers to independently excite a five-pad bearing with frequency ratios[4] of 0.5 and 2 along the horizontal direction, and 0.6, 0.7, 0.8 and 0.9 along the vertical (load) direction. The authors find that the bearing stiffness and damping coefficients have a slight or negligible dependency on excitation frequency. However, due to the limited operating conditions and excitation frequency range, the test results did not provide complete insight about the frequency dependency of TPJB force coefficients.

Later in 2004, Al-Ghasem and Rodriguez [8, 9] extensively assess the frequency dependency of rotordynamic coefficients by independently performing series of tests on flexure-pivot TPJBs. They utilize a multi-frequency force excitation method and a frequency domain approach to obtain the bearing force coefficients over a range of excitation load frequencies (10-290 Hz). The authors find that ignoring the virtual-mass term in a K-C-M model (Eq. 1) for obtaining the measured force coefficients make them frequency dependent. Based on the test results, they settled that the rotordynamic force coefficients are frequency independent when the dynamic stiffnesses are curve fitted to a K-C-M model (for $\omega/\Omega < 2$ only).

[4] Frequency ratio equals excitation frequency (ω)/shaft angular speed frequency (Ω).

The frequency independent force coefficients determined in Refs. [8, 9] do not correlate well with predictions from a computational model (over predicts stiffness and under predicts damping), in particular for excitation frequencies above the shaft angular frequency (1x). To bridge the gap between theory and experiments, Dmochowski [14] first account for pivot stiffness, and Wilkes [15] later account for both pad and pivot stiffness in their computational models and compare predictions against their experimentally obtained bearing stiffness and damping coefficients. The estimated pivot stiffness is based on the Hertzian contact stress method detailed in Ref. [7]. As per Ref. [14], the stiffness coefficients either increase or decrease with an increase in excitation frequency for a bearing with pivot softer (less stiff) than the oil-film. The variation in stiffness coefficients with excitation frequency is mostly dependent on bearing operating conditions and geometry. Moreover, the damping coefficient reduces significantly at excitation frequencies higher than the shaft angular frequency for a bearing with a soft pivot (pivot stiffness equal to or lower than the oil film stiffness).

San Andrés and Tao [16] and San Andrés and Li [17] present a parametric study using a bulk-flow thermo-hydrodynamic model for TPJBs to further address the question on the effects of pivot and pad flexibility, respectively, on the bearing dynamic force properties. A bearing with soft pivots significantly reduces the bearing force coefficients [16]. The reduction is significant with a decrease in the pivot stiffness ratio (pivot stiffness/oil film stiffness) and an increase in the excitation frequency (especially at frequencies above synchronous speed). Pad flexibility also has a substantial influence on the journal eccentricity and dynamic force coefficients, particularly at large bearing loads (S<0.8) [17]. The inclusion of both pivot and pad flexibility in the model lower the predicted bearing stiffness and damping coefficients. While excluding them in the model under certain operating conditions result in overpredicted dynamic force results. References [16, 17] report a good correlation between the predictions from their improved models and the experimental results from other researchers [18, 19].

Table 3 details few experimental works that are most relevant to the current study on spherical pivot TPJBs. Wygant et al. [20, 21] present a comparison of the static and

dynamic force characteristics of two 5- pad TPJBs with two different pivot types; spherical and rocker pivot. The operating conditions include three rotor speeds 0.9, 1.65, and 2.25 krpm (max. shaft surface speed 8 m/s) and unit loads up to 0.7 MPa. The bearing has a flooded housing configuration; however, the authors did not state the details on the oil flow rate and housing pressure. The authors present the static and dynamic force results as a function of the Sommerfeld number[5] (S) [1]. The bearing with spherical pivots exhibits a positive attitude angle that increases with speed (13°-33°) whereas the bearing with rocker pivot shows negligible attitude angle. Applied synchronous speed force excitations (15, 27.5 and 37.5 Hz) deliver bearing stiffness and damping coefficients. As evident from the shaft attitude angle, the bearing with spherical pivots shows a presence of cross-coupling stiffness, whereas the bearing with rocker pivots shows negligible cross-coupling. The cross-coupling stiffnesses (K_{xy} and K_{yx}) for the spherical pivot bearing have same sign for S<0.8 but change to opposite signs for S>0.8. The opposite signs of the cross-coupling stiffnesses (K_{xy} and K_{yx}) can destabilize the R-B system [1]. For both the pivot types, the direct stiffness (K_{xx}) along the horizontal (orthogonal to applied load) direction increases whereas the direct stiffness (K_{yy}) along the vertical (applied load) direction decreases with an increase in the Sommerfeld number (S). The authors mention that a coefficient of sliding friction in a spherical pivot (surface contact) is two orders of magnitude larger than a coefficient of rolling friction in a rocker pivot (line contact), and which is responsible for the non-zero attitude angle and cross-coupling stiffnesses in a bearing with spherical pivots. The authors suggest that a pivot type (and its friction coefficient) plays a vital role in the static and dynamic force performance of a TPJB.

[5] Sommerfeld number is a parameter widely used for bearing design, i.e. $S = \frac{\mu N L D}{W} \left(\frac{R}{C_r}\right)^2$

Table 3. Relevant prior experimental works on TPJBs.

	Wygant et al. [20, 21] 1999		Pettinato and De Choudhury [22, 23] 1999		Delgado et al. [24] 2011	Kukla et al. [25] 2013	Coghlan and Childs [26, 27] 2015	Present study
Number of pads	**5**[6]	**5**	**5**	**5**	4 & **5**	**5**	4-Pad	5-Pad
Pivot type	**Ball-in-Socket**	Rocker	**Ball-in-Socket**	Rocker	Rocker	**Rocker**[7]	**Ball-in-socket**	Ball-in-socket
Load orientation	LOP	LOP	LBP	LBP	LBP & LOP	**LBP**	LBP	LBP
Pad arc length (deg)	**60**	52	**65**	55.5	x	56	72	63
Preload, m	0.348	0.303	0.345	0.351	0.16 & 0.30	0.23	0.3	0.43
Pivot offset	**50**	**50**	**50**	**50**	**50** & 60	60	**50**	50
Bearing clearance, C_b (mm)	x	x	0.193	0.194	0.2	0.6	0.18	0.13
Length, L (mm)	52.5	52.5	**38.1**	**38.1**	**43.6**	350	61	40.6
Shaft diameter, D (mm)	70	70	126.9	126.9	109	500	101.6	101.6
L/D ratio	0.75	0.75	**0.3**	**0.3**	**0.4**	0.7	0.6	0.4
Bearing material			Babbitt	Babbitt	x		Babbitt	Babbitt
Backing material	Bronze	Steel	**Steel**	**Steel**	x		Steel	Steel
Lubrication method	**Flooded**	**Flooded**	**Flooded**	**Flooded**	**Flooded**	Spray-bar, **Flooded**	**Flooded,** LEG, SBB, SB	Flooded
Seal dia. clearance, C_s (mm)	x	x	**0.559**	**0.559**	x	1	0.34	0.57
Seal Length, L_s (mm)	x	x	9.14	7.62	x		X	x
Max. operating surface speed (m/s)	8	8	72	72	93	**79**	**85**	85
Max. specific load (MPa)	0.7	0.7	1.7	1.7	0.3	**2**	2.9	2.1

[6] Bearing design parameters and operating conditions similar to the present study are displayed in red color.
[7] The rocker pivot in Ref. [25] has arches along the axial direction which allow axial rolling motion similar to that in a spherical pivot.

In 1999, Pettinato and De Choudhury [22, 23] report another experimental work for two TPJBs with spherical and rocker pivots. The test operating conditions are different compared to that in Refs. [20, 21] which include three rotor speeds 5, 7, and 12 krpm (max. shaft surface speed 72 m/s) and a bearing unit load up to 1.7 MPa. The test bearing has a pressurized housing design where the oil enters the bearing between the pads via feed holes (at a constant flow rate of 26 LPM) and exits the bearing through end seals on both sides. Similar to work in Refs. [20, 21], the authors notice a higher attitude angle for the spherical pivot bearing compared to the rocker pivot bearing indicating the presence of dynamic cross-coupling forces. The authors obtain bearing dynamic force coefficients using an unbalance mass excitation (1x) method. However, they present only the direct stiffness and damping coefficients and do not report any cross-coupled coefficients. The authors present the force coefficients as a function of the Sommerfeld number (S) as well as the bearing specific load for each rotor speed. The stiffness and damping coefficients are higher for the bearing with rocker pivots compared to the bearing with spherical pivots along the horizontal and vertical directions indicating a better dynamic performance with rocker pivots. An iso-viscous computational model overpredicts the force coefficients in the bearing with rocker pivots against the experimental results whereas it underpredicts for the bearing with spherical pivots for most operating conditions. The authors also present the measured radial pivot stiffness which is lower than a calculated value based on Hertzian contact stresses but still is higher than the oil film stiffness.

In 2011, Delgado et al. [24] present an experimental investigation of the dynamic characteristics of four different rocker-pivot TPJB configurations. The test bearings include a 4-pad (LBP) and 5-pad (LOP) bearings, each with 50% and 60% pivot offset. The operating conditions include three rotor speeds (max. 15 krpm with a shaft surface speed of 93 m/s) and a low specific load of 0.3 MPa. The measured direct force coefficients under LOP orientation show orthotropy with larger magnitude along the load direction, whereas the coefficients for LBP orientation show symmetry along both the directions. The orthotropy in the bearing coefficients is beneficial for the stability of the R-B system. However, the bearing under LOP orientation can have higher synchronous

(unbalance) response along the low stiffness direction while traversing the critical speed [1]. On changing the bearing orientation from LBP to LOP, the force coefficients increase (≈ 14% for direct stiffness and ≈ 44% for direct damping coefficients) along the load direction. However, the measurement uncertainties are high for the LOP compared to the LBP configuration. The authors report that the measured bearing pad temperatures do not match well with prediction due to the transient nature of the measurements and an inability to achieve a thermal steady-state. Regardless, the maximum pad temperature in the LBP configuration is lower than that in the LOP configuration as predicted and similar to that in Ref. [6].

In 2013, Kukla et al. [25] present a comparison of experimental and predicted dynamic force characteristics of a large size (0.5 m diameter) TPJB for a power generation application. The authors followed a different (complex) approach to determine the dynamic force coefficients by measuring the oil film pressures along the bearing circumference over a range of harmonic force excitation with frequency ratio equal to 0.5, 1 and 2. Ref. [25] presents the synchronous speed and non-synchronous speed stiffness and damping coefficients as a function of rotor surface speed (up to 79 m/s) and specific load (2 MPa). The numerically predicted stiffness and damping coefficients differ from the experimentally obtained coefficients by 70% and 40 % respectively. In most cases, the numerical method overpredicts the direct stiffness coefficient whereas it underpredicts the direct damping coefficient. The experimentally obtained stiffness coefficients remain constant or reduce with an increase in the frequency ratio while the predictions suggest otherwise. The difference between the experimental and predicted results increase with an increase in the frequency ratio, specific load and rotor speed. The authors mention that complexity in the experimental procedure and post-processing can significantly influence the bearing force coefficients and is the possible reason for the discrepancy between the experiments and predictions.

In 2015, Coghlan and Childs [26, 27] present experimental static and dynamic force performance results of 4-pad TPJBs in LBP orientation with spherical pivots and four lubrication methods such as single-orifice flooded, leading-edge-groove (LEG), spray-

bar-blocker (SBB) and spray-bar (SB). The operating test conditions comprise shaft surface speeds up to 85 m/s and a unit load up to 2.9 MPa. The oil flow rate (ISO VG 46) and supplied pressure for the flooded configuration are 38 LPM and 2.2-2.5 bar, respectively. The authors compare the experimental results with predictions from a thermo-hydrodynamic computational model (XLTPJB®) which accounts for fluid inertia and pivot stiffness along with the thermal expansion of the journal and bearing pads. The authors utilize a novel method to determine the operational (hot) bearing center by measuring the bearing clearance immediately after stopping a spinning rotor. Refs. [26, 27] also obtain the bearing center by a conventional method based on the journal position at zero load condition. The authors present the shaft eccentricity based on both the methods for locating the bearing center and finds that attitude angle changes from -10° to 5° with a new (hot) method. As expected, the direct lubrication method with evacuated housing design leads to a reduction in maximum pad temperatures by up to 14℃ for the LEG, 10℃ for the SBB and 13℃ for the SB. A thermal mixing coefficient (λ) of 0.8 in the model, which determines the amount of hot oil carry-over, produces predictions for maximum temperature for all configurations despite different lubrication methods. The dynamic load excitation procedure is similar to that adopted in Refs. [8, 9]. The direct stiffnesses correlate well with predicted results for all the bearing configurations. The direct damping coefficients decrease with an increase in the unit load and shaft speed. Except, the direct damping coefficients in flooded lubrication bearing configuration change negligibly with an increase in shaft speed. The cross-coupled stiffnesses are quite high, about 20-50% of the direct coefficients and have opposite signs at low unit loads and high rotor speeds. The direct virtual mass coefficients along the load direction are negative for all operating conditions. The authors report a reduction in the direct stiffnesses by up to 15%, 25% and 20% for the LEG, SBB, and SB direct lubrication methods, respectively, compared to the SO flooded configuration. Similarly, the direct damping coefficients reduce by up to 24%, 45% and 29% for the respective direct lubrication methods compared to the flooded configuration. The reduced magnitude of bearing stiffness and damping coefficient with direct lubrication methods is a matter of concern for the stability of the R-B system.

Table 4 summarizes the variation of stiffness and damping coefficients obtained experimentally by various research works discussed in this section. Most of the obtained coefficient results are conflicting except for the direct stiffness along the direction perpendicular to the load (non-load direction) and the direct damping along the load direction as highlighted.

Table 4. Stiffness and damping coefficients in various TPJB experimental works.

Parameter variation	Direction	Force coefficient	Wygant et al. [20, 21]	Pettinato and De Choudhury [22, 23]	Delgado et al. [24]	Kukla et al. [25]	Coghlan and Childs [26, 27]
Increasing rotor speed	Load direction	Direct stiffness	=	↑	↑	↓/=	↑/=
		Direct damping	↓	↓	↓	↓	↓/=
	Non-load direction	Direct stiffness	↓	↑	↑	↓/=	↑
		Direct damping	↓	↓	↑	↓	↓/=
Increasing specific load	Load direction	Direct stiffness	↑	↑	-	↑	↑
		Direct damping	↓	↑	-	↑/=	↓
	Non-load direction	Direct stiffness	↓	↑	-	↑	↑
		Direct damping	↓	↑	-	↑/=	↓/=

In 2017, Abdollahi [12] improves a thermohydrodynamic computational model XLTPJB® to predict the TPJB pads leading edge temperature by including the effect of lubricant mixing in the groove region. The author states that the amount of oil flow entering the loaded pads is lower compared to unloaded pads at high bearing loads due to resistance from high oil film pressure. Oil flow rate requirement also varies depending on whether a bearing has end seals (flooded) or not (evacuated). Such flow variations in a bearing pad are not considered by a conventional thermal mixing (hot oil carry-over) model. The computational model in Ref. [12] requires an empirical coefficient (C_i) which determines the portion of oil flow required for each pad based on the operating speed and applied static load. Additionally, an empirical groove mixing efficiency parameter (C_{gr}) in the model can characterize the portion of hot oil carry-over that either contributes to side leakage (C_{gr} = 1) or generates churning loss in the groove region between pads (C_{gr} = 0). The improved thermal mixing model can accurately represent various lubrication

methods including flooded or evacuated bearings as well as reduced or increased oil flow rates and deliver precise predictions for oil film temperature at leading edge of the pad. Ref. [12] compares the predictions from the improved model with the experimental results in Refs. [25, 26]. The author finds a good correlation between the theoretical predictions from the model and measured pads' surface temperature, film pressure along a circumferential and axial direction, and oil film thickness. The current study will compare the experimental results for the test TPJB with the improved thermo-elasto-hydro-dynamic (TEHD) computational model discussed in Ref. [12].

The heat dissipated in a bearing due to viscous shear drag (power loss) is mainly removed by the incoming fresh oil. However, a part of the energy is also conducted to the bearing housing and journal resulting in high metal temperature. A tin-based babbitt layer (on the top of a bearing pad) starts to soften at 125-135°C, while it melts at 235°C [4]. The oil flow rate plays a significant role in keeping the bearing pad temperatures within the limit (<125°C). The oil flow rate (Q) requirement in a bearing pad varies with a changing rotor speed, fluid film thickness, supply configuration and bearing geometry.

Early in 1985, Heshmat and Pinkus [28] investigate the influence of oil flow starvation on the performance of a rigid journal bearing. The authors supplied oil flow rate ranging from that required for the full-fluid film (nominal) to 30% of nominal flow. Additionally, the bearing also ran with an oil-ring lubrication which fell in the category of starved condition (20-30% of nominal flow rate). The authors report the oil flow reduction produced a continuous decrease in the hydrodynamic oil film arc-length, attitude angle, and drag power loss, and an increase in the journal eccentricity and exit oil temperature. The shaft vibrations (speed synchronous response) increase continuously with an increase in the degree of oil starvation and attributed to a decrease in the horizontal stiffness (normal to the load direction). The optimum load capacity shifted to a lower L/D ratio with an increase in the extent of oil starvation.

Later, many researchers experimentally study the influence of oil flow rate on the steady-state characteristics of TPJBs. Tanaka [29] finds that doubling oil flow rate (from 8 to 16 LPM) has an insignificant influence on pad temperatures since the calculated

requirement for the bearing was less than 3 LPM. Dmochowski et al. [30] find a negligible difference in maximum pad temperatures and dynamic force coefficients on reducing oil flow rate in a 5-pad TPJB with a sealed configuration. However, the drag power loss decreases by 12% due to lower churning loss in the bearing. DeCamillo and Brockwell [6] also report the influence of 50% reduced oil flow rate in a 5-pad TPJB. The flow reduction has a minimal effect on the pads' maximum temperature for operation at low rotor speeds (<6000 rpm; 48 m/s), whereas there is a significant increase in pads' temperature at high rotor speeds (>8000 rpm; 63 m/s). On reducing oil flow rate, the drag power loss reduces by up to 21%, thus demonstrating an improved mechanical efficiency, similar to that reported in Ref. [30]. In general, a reduced oil flow rate in TPJBs increases the oil and pad temperatures and increases journal eccentricity while reducing the drag power loss.

DeCamillo et al. [10] discuss random low-frequency (up to 30 Hz) low-amplitude (up to 0.2 mil peak-to-peak) vibrations, which they refer as 'subsynchronous vibration (SSV) hash,' witnessed in various turbomachinery supported by TPJBs using either a conventional or evacuated lubrication method. The authors speculate that the periodic pulse excitation originates in the starvation zone at the leading edge of the pad, as witnessed through the transparent bearing shell in Ref. [28], which might be responsible for SSV hash. Based on laboratory testing, the authors suggest that such random vibrations may be due to unloaded pads and can be more significant during reduced oil flow rate condition. SSV hash can be eliminated by replacing a bearing with a flooded housing, a centered pivot, and operating under a LOP orientation. However, a slight increase in synchronous rotor vibration also surfaced on the elimination of SSV hash. The authors mention that turbomachinery operating with SSV hash can be trouble-free for years, but such simplification might need further research.

In 2015, Whalen et al. [11] present a case study on SSV due to oil starvation in a turbine supported on TPJBs. The initial bearing design was a 5-pad TPJB with an evacuated housing which experienced high subsynchronous speed vibration when loaded at 100% operating speed (5500 rpm). Based on the analysis, the authors predict a negative log decrement at the damped natural frequency of the system. Subsequently, the authors

change the bearing geometry to a 3-pad TPJB oriented under LOP to achieve asymmetry in the force coefficients and thus to enhance stability. However, the turbine did not show any exclusion of SSV with the new bearing design. On further analysis, the authors find that the horizontal stiffness and damping are null when the top two pads are fully starved. The model assumes a fully starved condition in the pad when the supplied oil is insufficient to fill the entire gap. Based on the findings, the authors change their bearing with a flooded configuration which eliminated SSV at the desired operating condition.

In 2017, Nichols et al. [31] measured the effects of a reduced oil flow rate on SSV in a 5-pad TPJB (L/D=0.75, LBP, preload = 0.3, pad offset = 50%, L=52mm). The test conditions include rotor angular speeds from 8 to 12 krpm and specific load ranging from 124 to 265 kPa. The supplied oil flow rate is varied from 60 to 120% of nominal oil flow rate (3.79 LPM) based on the operating conditions. The test rotor experiences higher SSV at 0.45x to 0.55x of the shaft angular frequency particularly at supercritical rotor speeds (>10 krpm) and reduced oil flow rate (70-80% of nominal oil flow rate). The authors report a broad band of low frequency (0-75 Hz) SSV hash similar to that in Ref. [10] for all the operating conditions.

San Andrés et al. [32] predict the dynamic force performance of TPJBs (4-pad LBP and 5-pad LOP) using a starved fluid flow model which accounts for an effective pad arc length instead of full length. With oil starvation, the oil film does not cover the entire pad arc length, and thus hydrodynamic pressure generates over a shorter (effective) arc length in a bearing pad. The authors predict the operation of a 4-pad TPJB (LBP) with 100%, 71%, and 41% of nominal oil flow rate which reduces the effective pad arc length from 100% to 92% and 68% of the actual pad arc length, respectively. With a lower oil flow rate (41% & 71%), unloaded (top) pads do not generate any hydrodynamic pressure while loaded (bottom) pads generate a higher hydrodynamic pressure field compared to that in a full film condition. The authors notice an increase in the predicted direct stiffness and mass coefficients, along with a drastic reduction in the damping coefficients for the oil-starved bearing. Ref. [32] also predicts a frequency response of the rotor lateral vibration amplitude along the vertical (load) direction. The bearings operating with a starved flow

condition shows larger vibration peak amplitudes compared to the bearing operated with 100% oil flow. The bearing with a 40% reduced flow rate shows a vibration peak at a frequency close to the rotor speed due to a drastically reduced damping ratio. The authors further find that a TPJB operating under LOP orientation suffers more impact on its force coefficients and stability due to oil starvation as compared to that in a LBP bearing.

Based on the review of the prior relevant literature, the author realizes that the oil supply flow rate can have a significant influence on bearing performance. There is the need of extensive experimental work to examine the influence of the oil flow rate on the static as well as the dynamic characteristics of TPJBs. Additionally, this study will complement previous experimental works in Refs. [20-23, 25, 26] on a spherical pivot TPJBs by testing at various operating conditions, with different geometric parameters as shown in Table 3.

4. DESCRIPTION OF TEST RIG AND TEST BEARING

The test rig to evaluate TPJB performance is a revamped version of the one used in Refs. [8, 9, 15, 26]. The test facility utilizes a well-known floating bearing[8] test rig concept. This section presents the detailed summary of the major components and recent notable changes.

4.1 Mechanical System

Figures 4 and 5 present a schematic diagram and an isometric/sectional view of the updated test rig, respectively. The test rig consists of a main test-section supported on a steel bed plate, a rotor, and a driver air turbine motor. A 65 kW-power air turbine motor, running on medium pressure (8 bar) compressed air, drives the test shaft through a high-speed bellow coupling, a torque-limiter, and a torque meter. The maximum speed of the air turbine is 17,000 rpm. The test shaft (Fig. 6) is made from AISI 4140 material and machined to a precise diameter of 101.590 ± 0.003 mm (3.9996 ± 0.0002 in.) at the test bearing section. Two angular contact ball bearings placed in a back-to-back orientation support the shaft. Two stiff pedestals hold the ball bearings, both being 406 mm (16 in) apart. An oil-mist lubrication system lubricates the ball bearings.

A pneumatic static loader applies a load only along the (-) *y* direction, whereas the hydraulic shakers apply dynamic loads along both the *x* and *y* directions as shown in Figure 7. A cable, connected to the bearing stator assembly through a pulley and a yoke, apply a static load along the (-) *y*-direction. A load cell attached to the cable measures the applied load. The rated maximum available load is 22 kN. The soft spring (K_{spring} = 0.26 MN/m) in the static loading system eliminates transmission of the vibration from the bearing stator to the static loader.

[8] Contrary to a typical operating physical condition, a floating bearing experiences the applied static and dynamic force externally via a loading mechanism attached to a bearing housing; hence the static load due to gravity and excitation due to shaft imbalance are insignificant.

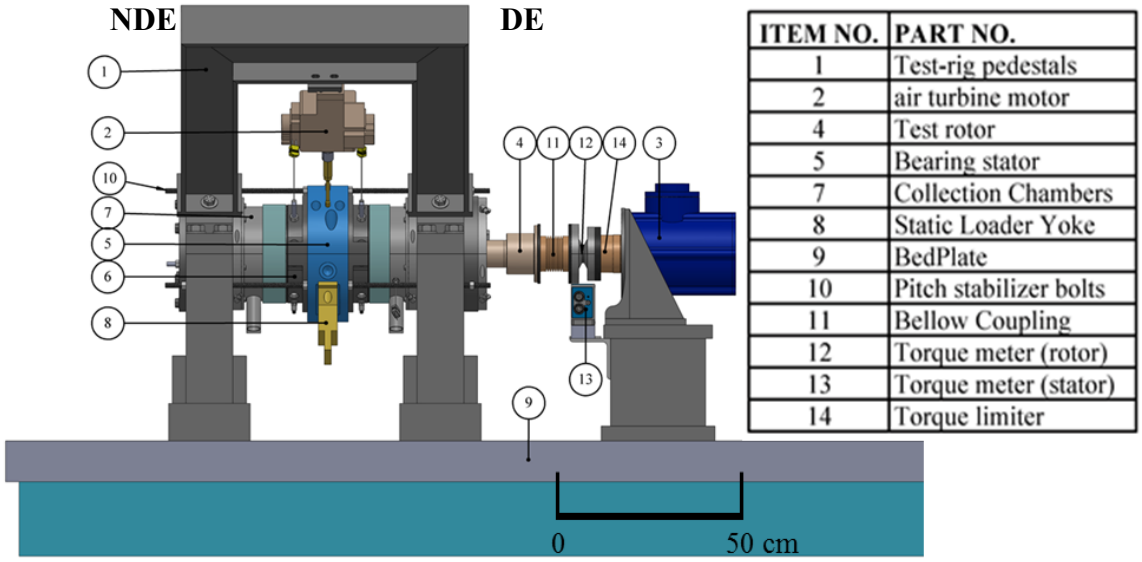

ITEM NO.	PART NO.
1	Test-rig pedestals
2	air turbine motor
4	Test rotor
5	Bearing stator
7	Collection Chambers
8	Static Loader Yoke
9	BedPlate
10	Pitch stabilizer bolts
11	Bellow Coupling
12	Torque meter (rotor)
13	Torque meter (stator)
14	Torque limiter

Figure 4. Schematic diagram of test rig.

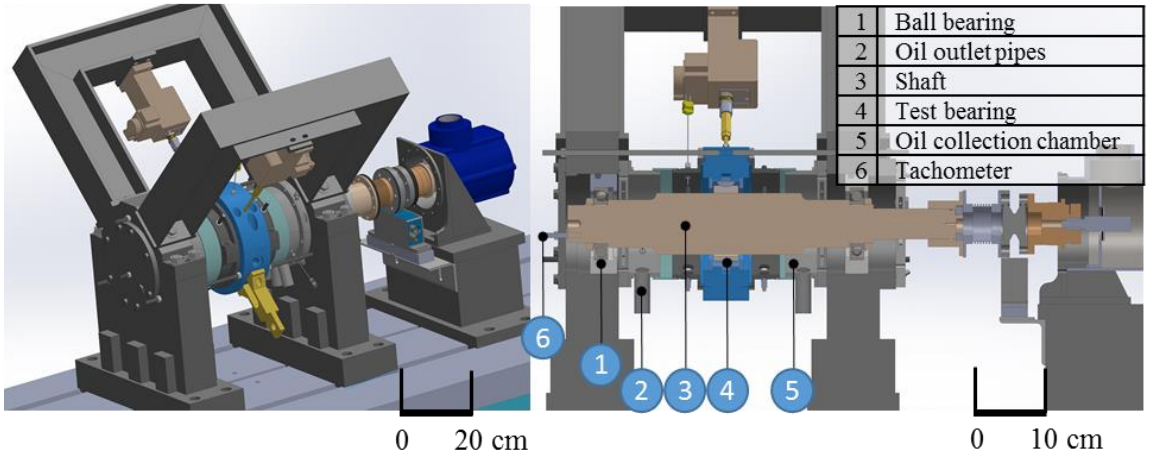

1	Ball bearing
2	Oil outlet pipes
3	Shaft
4	Test bearing
5	Oil collection chamber
6	Tachometer

Figure 5. (Left) Isometric view and (right) sectional view of test rig.

Two orthogonally mounted electro-hydraulic shaker heads attached to the bearing housing (stator) (a) deliver dynamic loads, and (b) aid to position the bearing relative to the shaft. Each shaker head consists of a hydraulic valve and a linear variable differential transformer (LVDT) sensor. Hydraulic-pump power a shaker head, while an electronics master-controller precisely controls the stator static and dynamic motion. The shakers can

exert a maximum load of 4.4 kN and excitation frequencies of up to 1000 Hz (e.g., 440 N dynamic force up to 600 Hz), as shown in Figure 8. Along each direction (*x*, *y*), a stinger connects the shaker head to the bearing stator and transmits the static and dynamic load.

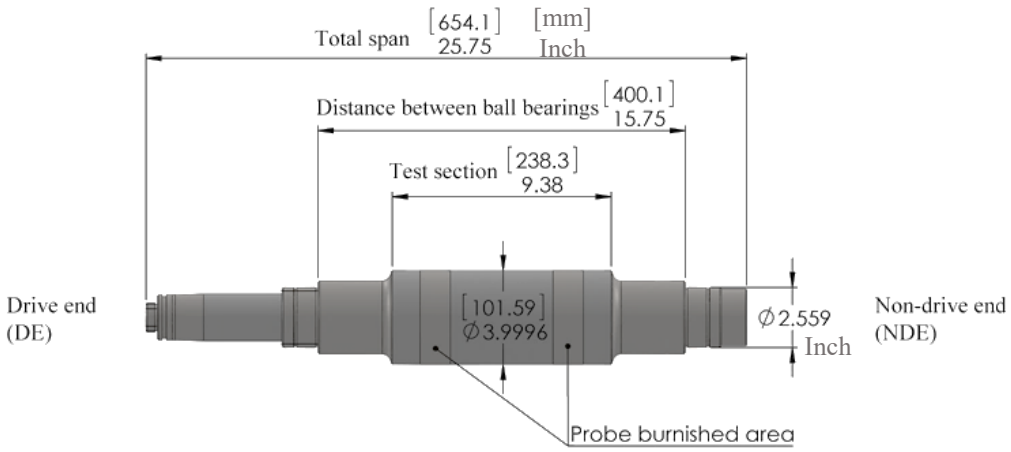

Figure 6. Dimensional drawing of test shaft.

Figure 9 shows the bearing stator that holds the test bearing, two end caps, and all the associated instrumentation. The oil enters the bearing from the bottom of the bearing stator via the oil chamber. Three pairs of tensioned stabilizer bolts connect the bearing stator to the pedestals. These bolts restrain pitch motions of the bearing housing, allow alignment of the R-B system, and negate the loading due to gravity.

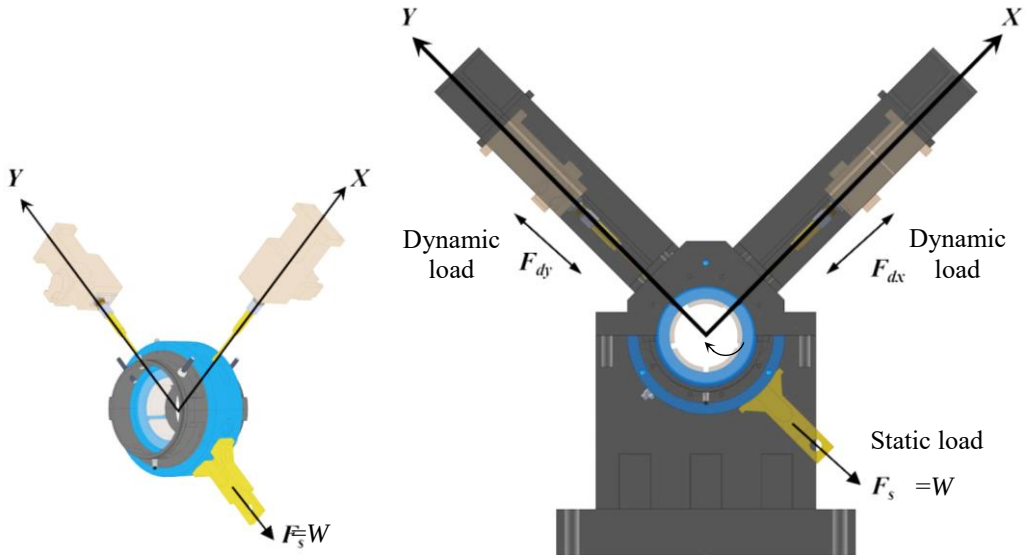

Figure 7. (Left) Isometric and (right) front view from the NDE side of test rig loading arrangement.

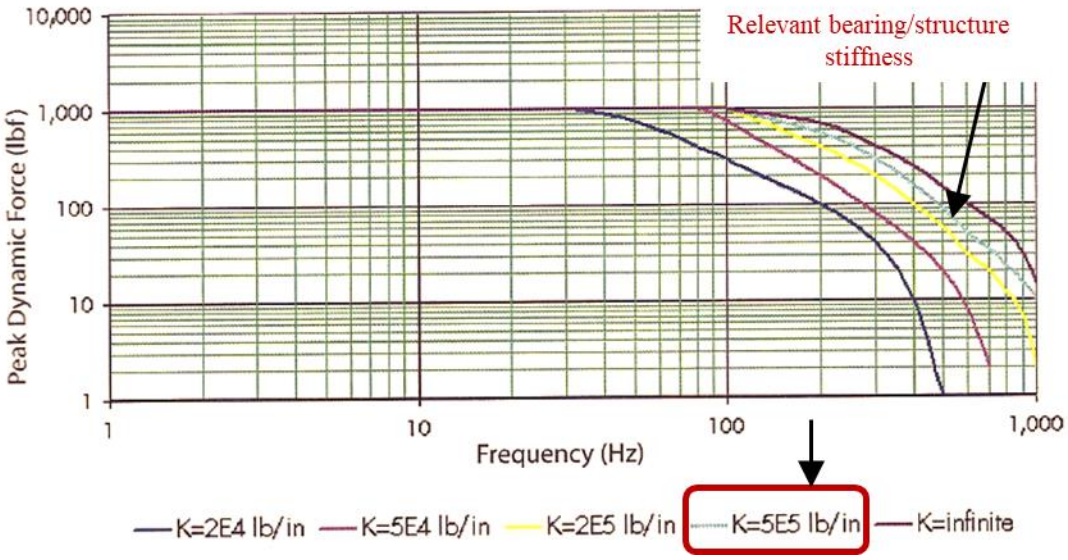

Figure 8. Peak dynamic force vs. frequency of shaker system. (Source: Xcite systems manual)

The oil supply system in the facility consists of a positive displacement gear pump that delivers the oil (ISO VG 32) from the main tank (capacity: 946 Liter) to the test bearing.

The oil exiting the test bearing flows to a sump tank (capacity: 378 Liter) due to gravity. A similar gear pump returns the oil to the main tank. The oil system can supply a maximum flow rate of 208 liters per minute (55 gpm) to the test rig. A pneumatic globe valve precisely controls the oil supply flow rate. The oil system also includes two heat exchangers, an air-cooled oil cooler and a 15-kW oil heater. The combined operation of both the heat exchangers maintains the required oil temperature at the inlet of the test bearing. The accumulator stores oil up to 27 bar (400 psi) in the system which can deliver oil to the test bearing during an emergency coast down.

4.2 Instrumentation

Table 5 lists the measurement sensors and their type. Four eddy-current sensors, located in the end caps, arranged in two mutually perpendicular directions measure the relative displacement between the shaft and bearing in *x* and *y*-axes, see Figure 9. Two sets of the eddy-current sensors on each side of the test bearing allow monitoring of its pitch and yaw. Three J-type thermocouples measure oil temperature in the oil-inlet chamber as well as in the downstream end-caps. Three piezoresistive strain gauge-type pressure sensors installed on the bearing stator, and two end caps measure the oil pressure at the inlet and outlet of the bearing, respectively.

Two force sensors mounted on the hydraulic shaker heads along the *x* and *y* directions measure the applied dynamic forces. One force sensor attached to the pneumatic static-loader cable measures the static load applied to the test bearing. Two accelerometers mounted on the bearing stator in the *x* and *y*-axes measure the acceleration of the bearing, respectively. A displacement sensor (not shown) facing the key phasor on the shaft measures the shaft angular speed. A strain-gauge type torque-meter installed in-line with the shaft measures the driving torque. A turbine-type flow meter mounted upstream of the test rig measures the oil flow rate (max. 100 gpm) delivered to the test bearing.

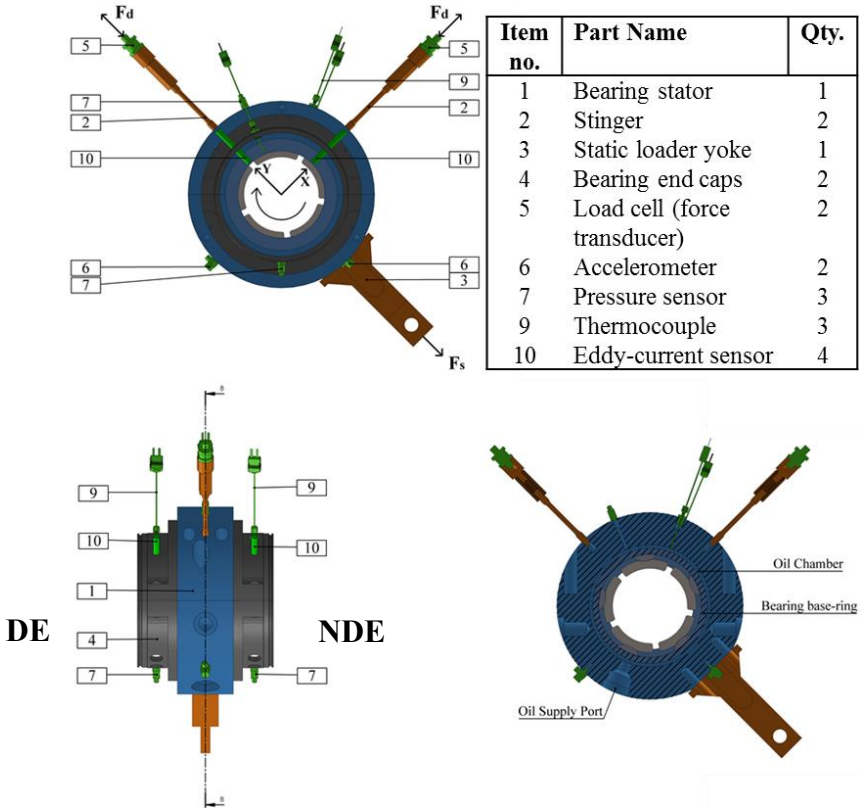

Item no.	Part Name	Qty.
1	Bearing stator	1
2	Stinger	2
3	Static loader yoke	1
4	Bearing end caps	2
5	Load cell (force transducer)	2
6	Accelerometer	2
7	Pressure sensor	3
9	Thermocouple	3
10	Eddy-current sensor	4

Figure 9. Front view (top), side view (bottom left) and section view (bottom right) of bearing stator with instrumentation.

Figure 10 shows the layout of 30 thermocouples (K-type) instrumented in the five pads of the test bearing. The depth of the sensors from the top Babbitt surface of each pad is about 2.4 mm. Pad 4 and 5 are the loaded-pads for the LBP orientation, while Pad 2 is the loaded-pad for the LOP orientation of the bearing. Each pad has total six embedded thermocouples; four at different pad arc-length (10, 25, 75 and 90%) on the bearing mid-plane, and two along the axial direction on 75% of the pad arc-length. Note that the designation X-Y for the thermocouple corresponds to X=pad number and Y=location on the pad, one is near to the leading edge and six near to the trailing edge of the pad as shown in Figure 10.

Table 5. List of measurement sensors and their measurement uncertainty in test rig.

Measurement Type	*Sensor Type*	*Uncertainty*	*Range*
Oil pressure	Piezo resistive strain gauge	0.5 kPa	0-690 kPa
Oil temperature	J-type thermocouple	0.5 °C	(-184)-260 °C
Rotor-Bearing displacement	Eddy-current sensor	2.5 µm	0-1000 µm
Force	Strain-gauge load cell	2 N	0-44,000 N
Acceleration	Uni-axial piezo-sensor	0.00015 g	0-100 g
Rotor speed	Eddy-current sensor / key phasor	5 RPM	-
Torque	Strain-gauge type in-line sensor	0.1 Nm	0-100 Nm
Oil flow rate	Turbine-type flow meter	0.05 LPM	0-378 LPM
Pad metal temperature	K-type thermocouple	0.5 °C	(-184)-260 °C

4.3 Test Bearing Configuration

Table 1 (shown on page 7) details the test bearing geometry, lubricant properties, and operating conditions. Figure 11 shows a photograph of the test bearing, a five-pad TPJB (L/D = 0.4) with a ball-in-socket pivot and 50% pivot offset. The pads have a mean preload of 0.42 at room temperature. The outer dimension of the shaft for the test bearing is 101.6 mm. The design bearing diametric clearance is 0.122 mm, whereas the measured average (assembled) clearance (at 25°C) is 0.125 mm. The clearance to radius ratio (C_r/R) of the bearing is ≈ 0.0013. The bearing base-ring has two end seals on each side of a diametric clearance of 0.570 mm. An oil feed-groove between each pad on the outer ring delivers the oil to the test bearing under pressurized (flooded) configuration.

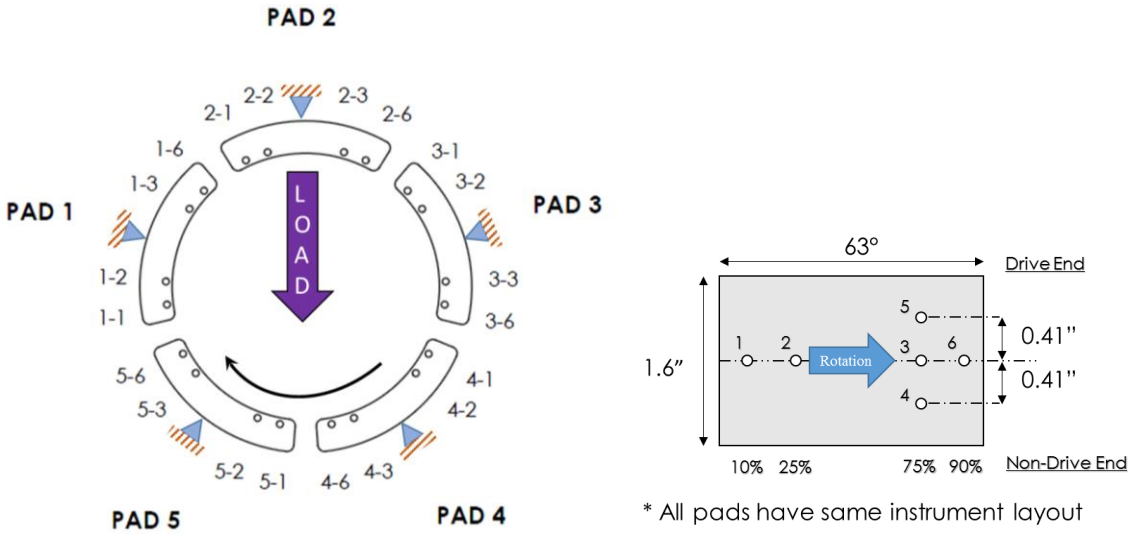

Figure 10. Bearing pad thermocouple layout in test bearing.

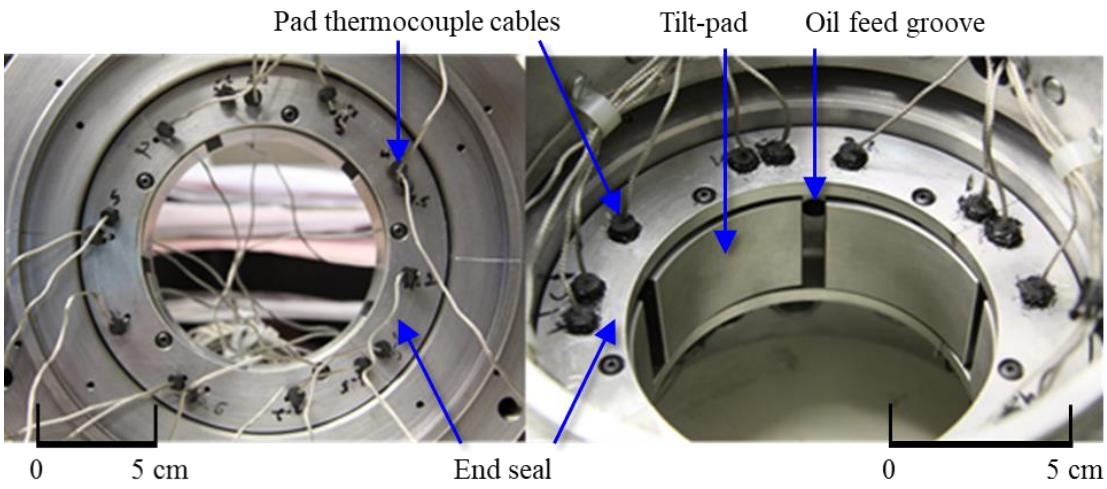

Figure 11. Photographs of test bearing.

5. TASK ACCOMPLISHED

This thesis accomplishes the following primary tasks:

- Revamping of an existing seal test rig. Major modifications include: (1) replacing the variable-frequency drive (VFD) electric motor with an air-turbine motor, and (2) designing and installing a torque-meter sensor and flexible coupling.
- Designing a bearing stator for its integration into the modified test rig.
- Commissioning various equipment and sensors in the test rig and troubleshooting their installation and operation.
- Calculation of the pivot stiffness using Hertz method [7].
- For operation under various applied unit load (max. 2.1 MPa), rotor speed (max. 16 krpm) and oil flow rate, conduct measurements of the static load parameters such as shaft equilibrium position, oil temperature at the exit plane of bearing, pad metal temperature and frictional drag torque.
- Conduct measurements of the dynamic load parameters such as dynamic force, acceleration, and relative displacement during a pseudo-random excitation (10-300 Hz) of the bearing at the operating test conditions.
- Estimation of the test bearing force coefficients using the frequency-domain complex stiffness method utilized in Refs. [8, 9, 26].
- Comparison of the measured test results (static and dynamic) with predictions from XLTPJB® [12].

6. EXPERIMENTAL PROCEDURE

6.1 Bearing Clearance and Center Measurement

This section explains the procedure for the bearing stator-shaft alignment, bearing clearance and center measurement. A proper alignment between the bearing and shaft is essential prior to obtaining the bearing clearance and center. Two sets of displacement sensors located along the *x* and *y*-axes on each side of the bearing, as shown in Figure 9, align the test bearing relative to the shaft. Six pitch stabilizer studs holding the bearing stator against the rig pedestals, as shown in Figure 4, to adjust for the misalignment. Figure 12 presents the schematic diagrams of pitch and yaw angle of the bearing stator. Four pitch stabilizer studs in the bottom plane of the bearing stator adjust the yaw angle, while two pitch stabilizer studs on top of the bearing stator adjust the pitch angle. A good alignment will measure a perfectly identical bearing clearance from both sets of eddy-current probes.

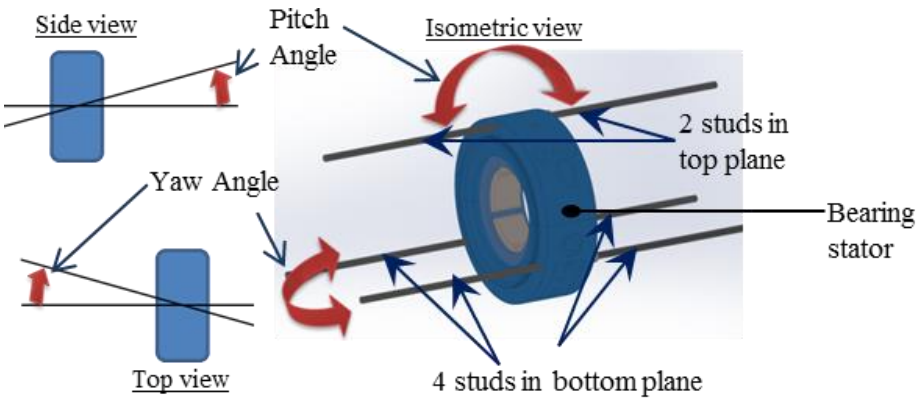

Figure 12. Schematic diagrams representing the pitch and yaw angle of the bearing stator.

A clearance measurement procedure is complex for a TPJB due to the bearing moving tilting-pads on their pivots. The basic method to measure clearance involves a dial indicator, attached to the bearing outer body, to measure displacements due to a small load

applied by hand [1]. For a bearing with an even number of pads, the clearance is equal to the displacement whereas for bearing with an odd number of pads the clearance is smaller than the measured displacement due to a static shaft sink between two adjacent pads. During the procedure, the shaft or mandrel is stationary and the bearing has no oil. This simple method measures the clearance of individual pads, and hence an average of each pad clearance provides a mean bearing clearance.

In the present study, two hydraulic shakers mounted orthogonally push and pull the bearing stator with a light load (≈ 200 N) around the stationary shaft until contact is achieved. Two eddy-current displacement sensors located along the *x* and *y*-axes, as shown in Figure 9, measure the relative displacement between the shaft and bearing stator while the bearing is forced to precess around the journal by making a slight contact. This method provides a complete periphery (shape) of the bearing clearance. The resulting shape of the clearance is a pentagon, where each side represents an individual pad in the TPJB. The coordinates of the corners (vertex) and pivots are extracted from the measured clearance shape. A best-fit circle of the derived pivot coordinates delivers an estimated circular bearing clearance and a bearing center.

Additionally, the distance (B), see Figure 13, between a corner (vertex) and an opposite side (or a pivot) in TPJB with an odd number of pads also provides the bearing diametrical clearance (C_d) based on a trigonometric function given as,

$$C_d = B\,\frac{\text{Cos}\,\theta_P}{(1+\text{Cos}\,\theta_P)} \;=\; (0.894)\,B \quad \text{[for a 5 pad TPJB]} \tag{2}$$

Above $\theta_p = 180/n_p$. For a five pad ($n_p = 5$) tilting-pad journal bearing, $\theta_p = 32^o$

Figure 13 depicts the measured diametrical clearance (C_d), 'cold' and 'hot', for the test bearing under a light applied load (<200 N). The '*cold*' clearance (CC) refers to the measurement at room temperature (24°C), whereas the '*hot*' clearance (HC) refers to the measurement at a higher rotor-bearing temperature immediately after a test. The bearing pads' temperatures during a hot clearance measurement are not similar to operating temperatures; however, this method yields a better clearance estimate compared to a cold

clearance measurement. The journal static equilibrium position is calculated based on the hot bearing center or near a zero applied load position.

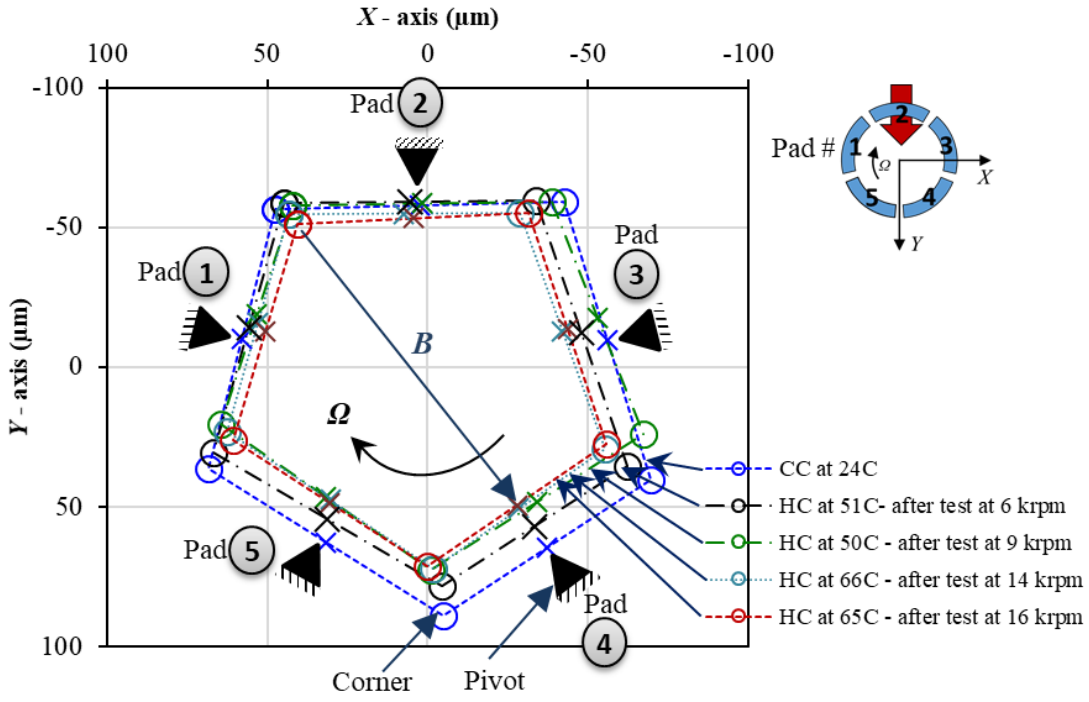

Figure 13. Bearing clearance measurement conducted at ambient temperature (24°C) and at warm temperature (50-66°C) after a test at various rotor speed (6, 9, 14 and 16 krpm) for a five-pad TPJB.

Table 6 lists the recorded diametrical clearance of the individual bearing pads of the test bearing. The nominal or average bearing clearance is the average of the five bearing pad clearances. Pads number 4 and 5 are the loaded ones for the LBP orientation and represented by the bottom two sides in Figure 13. All the thermocouples in the bearing pads read the same temperature after shutting down the turbine, as mentioned in Table 6.

The rotor, pads and housing material expand when operating at an elevated temperature. Each bearing pad has a different operating temperature and experiences a different thermal growth which gives a dissimilar nominal bearing clearance at the load operating condition. The bearing clearance becomes smaller or larger depending on the relative thermal expansion coefficient of the housing and shaft, respectively.

In the present study[9], the measured nominal *hot* clearance ($T \approx 65°C$) is 16% smaller in size compared to the *cold* clearance ($T \approx 24°C$) after continuous operation at 16 krpm.

Table 6. Bearing diametric clearance (C_d) measurement under various operating conditions.

	Measured Diametric Bearing Clearance ($C_d = 2C_r$)				
Pad temp. (ºC)	25	51	50	66	65
Rotor speed prior recording (RPM)	0	6000	9000	14000	16000
Pad number	(μm)	(μm)	(μm)	(μm)	(μm)
1	132	124	116	113	108
2	127	117	112	104	107
3	121	113	114	103	101
4	131	123	117	113	111
5	118	109	110	98	99
Average of 5 pads (C_d)	**125 ± 2.5**	**117 ± 2.5**	**113 ± 2.5**	**106 ± 2.5**	**105 ± 2.5**

Figure 14 depicts the geometric bearing center and operating 'hot' bearing center for operation at 6 and 9 krpm rotor speed. The center of the best-fit circle, derived from the measured pivot locations, is referred to as the 'geometric bearing center' in a stationary condition. However, the bearing center changes with the operating condition due to thermal expansion or contraction of both the journal and the bearing pads. The shaker system in the test-rig maintains the bearing stator at its static equilibrium position without any additional applied force and thus balances the effect of its weight. Hence, the bearing position changes from geometric center to a *hot* operating center which is considered to be an initial (zero) shaft position before applying a static load for a specific operating rotor speed. At a high rotor speed (>10 krpm), operation near the bearing center location could not be recorded with a null applied load on the bearing due to high vibration amplitude at the coupling. However, the bearing center is estimated based on the *hot* bearing clearance

[9] Wilkes and Childs [15] obtained about a 30% reduced hot clearance for a test after a pad temperature rise of 50°C; whereas, Coghlan and Childs [27] obtained about 20% reduced hot clearance after tests were completed at 12 krpm (ΔT not mentioned).

measurement immediately after shut down. The shaft eccentricity at a distinct shaft surface speed and applied load are referenced either to a recorded or an estimated *hot* bearing center.

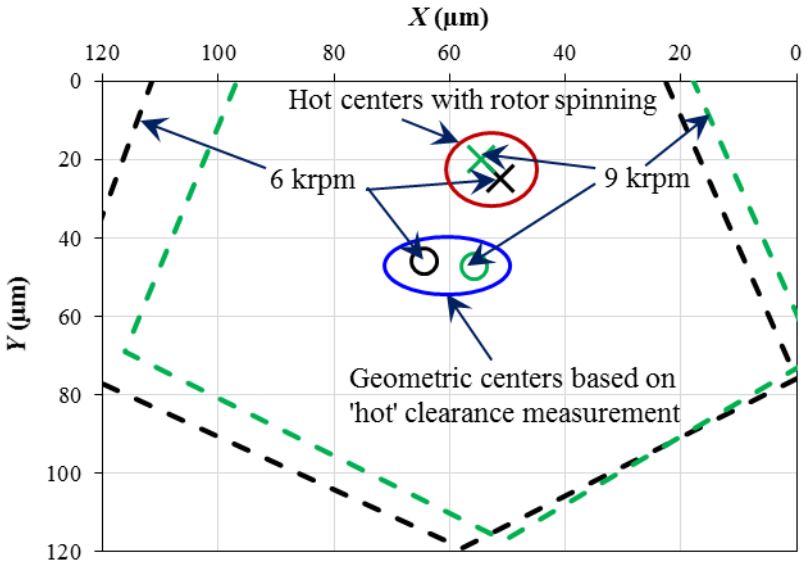

Figure 14. Measured geometric and operating bearing center location after the operation at 6 and 9 krpm rotor speed, under null applied load, and 100% oil flow rate.

6.2 Pivot Stiffness Calculation

The pivot stiffness (K_p) and its deflection (δ_p) for a ball-in-socket pivot, see Figure 15, are functions of the applied load (W) and the geometry of the surfaces in contact. As per Ref. [7]

$$K_p(W)=1.442\sqrt[3]{\left(\frac{C_1\,W}{C_2{}^2}\right)} \tag{3}$$

$$\delta_p=1.040\left(\frac{C_2{}^2\,W^2}{C_1}\right)^{1/3} \tag{4}$$

where, $C_1=\dfrac{D_b\,D_s}{D_s-D_b}$, $\quad C_2=\left(\dfrac{1-\nu_b{}^2}{E_b}\right)+\left(\dfrac{1-\nu_s{}^2}{E_s}\right)$

Above D_b and D_s are the diameters of the ball (pivot) and socket, respectively. E = Young's modulus and v = Poisson's ratio for the ball (subscript b) and socket (subscript s) material.

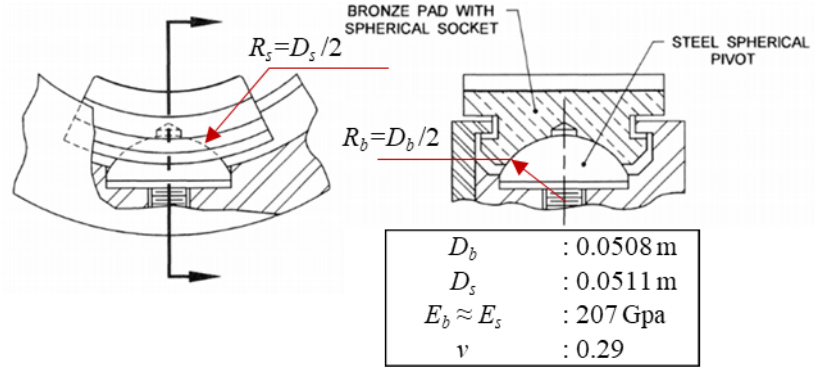

Figure 15. Schematic diagram of a ball-in-socket pivot adapted from Ref. [7].

Figure 16(a) presents the calculated pivot deflection (δ) as a function of applied radial force (W), and Figure 16(b) presents the calculated pivot stiffness (K_p) as a function of both applied radial load and pivot deflection. The calculation for pivot deflection is based on nominal dimensions of the pivot and socket as shown in Fig. 15 (accurate dimensions are proprietary information).

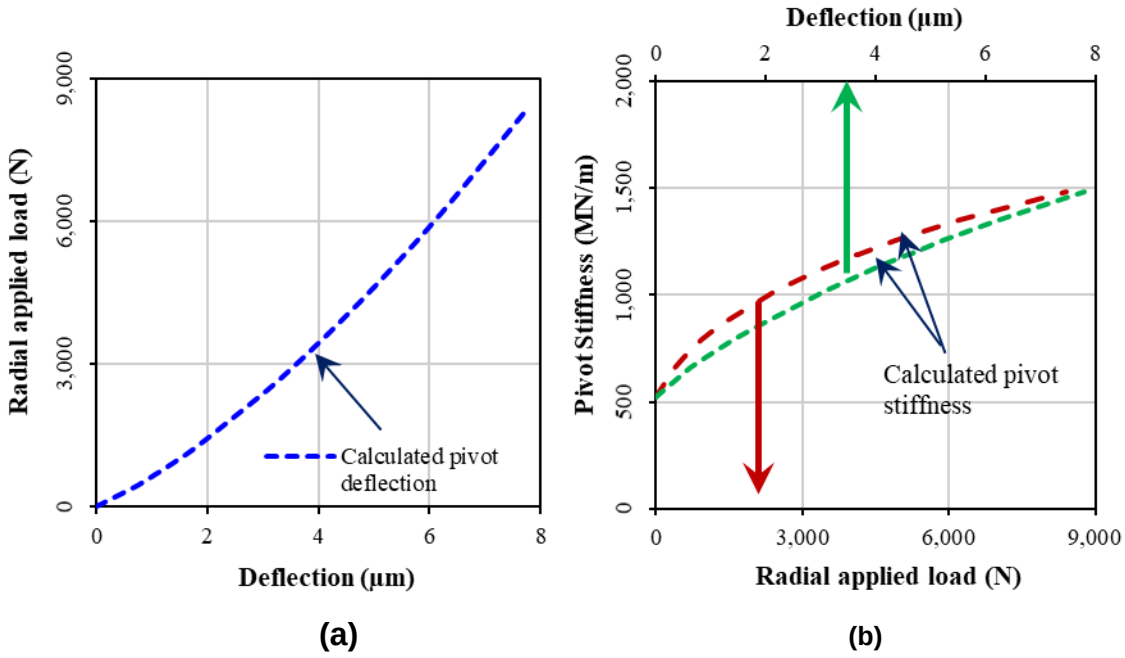

Figure 16. (a) Applied radial load vs. calculated pivot deflection and (b) calculated pivot stiffness (K_p) vs. applied radial load and vs. pivot deflection.

6.3 Parameter Identification Procedure

This section explains the parameter identification method adopted from Childs and Hale [33] and utilized in Refs. [8, 9, 15, 26]. The method considers the test-bearing as a mechanical system with two degrees of freedom subjected to lateral motion along x and y directions as shown in Fig. 17. The equation of motion (EOM) for the bearing stator along both the directions can be represented as,

$$\begin{bmatrix} f_{dx} \\ f_{dy} \end{bmatrix} + \begin{bmatrix} f_{bx} \\ f_{by} \end{bmatrix} + \begin{bmatrix} f_{sx} \\ f_{sy} \end{bmatrix} = \begin{Bmatrix} M_b\, \alpha_x \\ M_b\, \alpha_y \end{Bmatrix} \tag{5}$$

where M_b (≈ 24 kg) is the mass of the bearing stator, (f_{dx}, f_{dy}) are the external dynamic excitation load, (f_{bx}, f_{by}) are the bearing reaction forces, (f_{sx}, f_{sy}) are the structural (baseline) reaction forces, and (α_x, α_y) are the acceleration of the bearing stator along x and y directions, respectively.

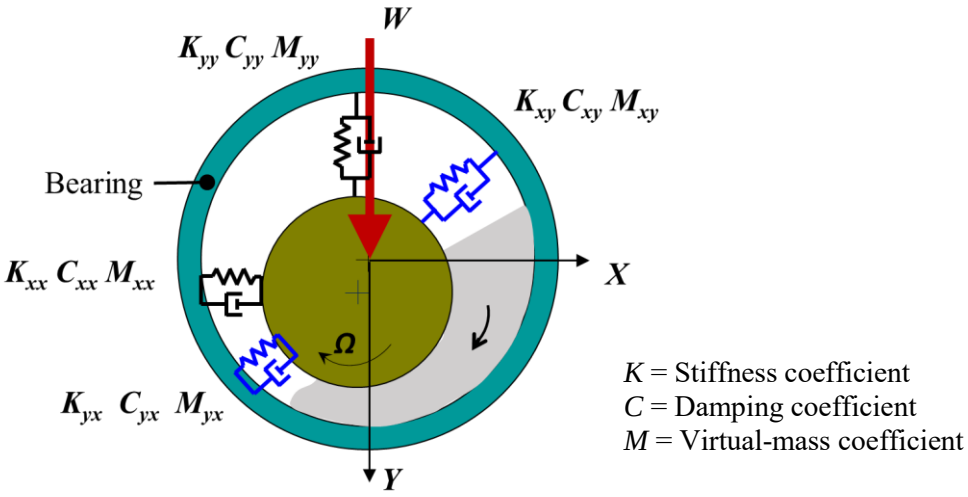

Figure 17. Schematic diagram representing force coefficients in a fluid film bearing.

The reaction forces generated by the structure are represented as,

$$\begin{bmatrix} f_{sx} \\ f_{sy} \end{bmatrix} = \begin{bmatrix} K_{xx\_s} & 0 \\ 0 & K_{yy\_s} \end{bmatrix} \begin{Bmatrix} \Delta x \\ \Delta y \end{Bmatrix} + \begin{bmatrix} C_{xx\_s} & 0 \\ 0 & C_{yy\_s} \end{bmatrix} \begin{Bmatrix} \Delta \dot{x} \\ \Delta \dot{y} \end{Bmatrix} \tag{6}$$

where K_{ij_s} and C_{ij_s} ($i, j = x, y$) are the stiffness and damping force coefficients generated due to stingers and other structural members.

On combining three equations, the KCM model [Eqs. (1,6)] and EOM [Eq. (5)], gives a complete equation of motion for the bearing stator in time-domain as

$$\begin{aligned} \begin{bmatrix} f_{dx} - M_{bx}\,\alpha_x \\ f_{dy} - M_{by}\,\alpha_y \end{bmatrix} &= \begin{bmatrix} K_{xx} & K_{xy} \\ K_{yx} & K_{yy} \end{bmatrix} \begin{Bmatrix} \Delta x \\ \Delta y \end{Bmatrix} + \begin{bmatrix} C_{xx} & C_{xy} \\ C_{yx} & C_{yy} \end{bmatrix} \begin{Bmatrix} \Delta \dot{x} \\ \Delta \dot{y} \end{Bmatrix} + \begin{bmatrix} M_{xx} & M_{xy} \\ M_{yx} & M_{yy} \end{bmatrix} \begin{Bmatrix} \Delta \ddot{x} \\ \Delta \ddot{y} \end{Bmatrix} \\ &+ \begin{bmatrix} K_{xx\_s} & 0 \\ 0 & K_{yy\_s} \end{bmatrix} \begin{Bmatrix} \Delta x \\ \Delta y \end{Bmatrix} + \begin{bmatrix} C_{xx\_s} & 0 \\ 0 & C_{yy\_s} \end{bmatrix} \begin{Bmatrix} \Delta \dot{x} \\ \Delta \dot{y} \end{Bmatrix} \end{aligned} \tag{7}$$

Two linearly independent load excitation tests are required to determine the four unknown force coefficients of stiffness, damping, and virtual-mass. This is done by exciting the system along each direction (x and y) separately while keeping the forces in the other direction to null. Next, the Discrete Fourier Transform (DFT) of the measured

dynamic forces, relative displacements, and relative accelerations is performed to transform the measured time domain data to the frequency domain. This transforms Eq. (7) in the frequency domain for two independent excitation tests ($j = x, y$) as

$$\begin{bmatrix} F_{dxx} - M_{bx} \times A_{xx} & F_{dxy} - M_{bx} \times A_{xy} \\ F_{dyx} - M_{by} \times A_{yx} & F_{dyy} - M_{by} \times A_{yy} \end{bmatrix} = \left\{ \begin{array}{c} \begin{bmatrix} K_{xx} & K_{xy} \\ K_{yx} & K_{yy} \end{bmatrix} + \begin{bmatrix} K_{xx\_s} & 0 \\ 0 & K_{yy\_s} \end{bmatrix} \\ + i\omega \left(\begin{bmatrix} C_{xx} & C_{xy} \\ C_{yx} & C_{yy} \end{bmatrix} + \begin{bmatrix} C_{xx\_s} & 0 \\ 0 & C_{yy\_s} \end{bmatrix} \right) \\ - \omega^2 \begin{bmatrix} M_{xx} & M_{xy} \\ M_{yx} & M_{yy} \end{bmatrix} \end{array} \right\} \times \begin{bmatrix} D_{xx} & D_{xy} \\ D_{yx} & D_{yy} \end{bmatrix} \tag{8}$$

where ω is the excitation frequency in rad/s, (F_{dxx}, F_{dyx}, F_{dxy}, F_{dyy}) are the DFT of the dynamic forces, (A_{xx}, A_{yx} A_{xy}, A_{yy}) are the DFT of the bearing stator accelerations, and (D_{xx}, D_{yx}, D_{xy}, D_{yy}) are the DFT of the relative displacements between the bearing and the journal along the x and y directions for two different excitation loads (j=x, y).

The bearing impedance or complex dynamic stiffness (H_{ij}) can be determined directly from Eq. (8) as

$$[H_{ij}] = [F_{dij} - M_b A_{ij}] [D_{ij}]^{-1} \tag{9}$$

The complex dynamic stiffness matrix can be expressed, based on Eqs. (8-9), as

$$\begin{bmatrix} H_{xx} & H_{xy} \\ H_{yx} & H_{yy} \end{bmatrix} = \begin{bmatrix} (K_{xx} + K_{xx\_s} - \omega^2 M_{xx}) + i\omega (C_{xx} + C_{xx\_s}) & (K_{xy} - \omega^2 M_{xy}) + i\omega C_{xy} \\ (K_{yx} - \omega^2 M_{yx}) + i\omega C_{yx} & (K_{yy} + K_{yy\_s} - \omega^2 M_{yy}) + i\omega (C_{yy} + C_{yy\_s}) \end{bmatrix} \tag{10}$$

where $H_{ij} = (K_{ij} - \omega^2 M_{ij}) + i\omega C$

The experimental force (K, C, and M) coefficients are identified by curve-fitting the KCM model to the experimental (real and imaginary) complex stiffness measured over a wide excitation frequency range (10-300 Hz). The real part of the complex dynamic stiffness gives the stiffness (K) and virtual-mass (M) coefficients, whereas the imaginary part gives the damping coefficient (C).

The stiffness and virtual-mass coefficient are obtained by curve fitting Re (H_{ij}) as a quadratic function of excitation frequency (ω), such as $y = m\,\omega^2 + b$, and then calculating the zero-frequency intercept and curvature of the curve fit, respectively. The damping coefficient is obtained by curve fitting Im (H_{ij}) as a linear function of ω and then calculating the slope of the linear regression.

$$\text{Re}\,(H_{ij}) \rightarrow (K_{ij} - \omega^2\, M_{ij}) \tag{11}$$

$$\text{Im}\,(H_{ij}) \rightarrow \omega\, C_{ij} \tag{12}$$

The slope and the y-intercept of a linear regression function are given by

$$m = \frac{n\sum_{k=1}^{n} x_k y_k - \sum_{k=1}^{n} x_k \sum_{k=1}^{n} y_k}{\sum_{k=1}^{n} x_k^2 - \left(\sum_{k=1}^{n} x_k\right)^2} \tag{13}$$

$$b = \left(\frac{1}{n}\sum_{k=1}^{n} x_k\right) - m\left(\frac{1}{n}\sum_{k=1}^{n} y_k\right) \tag{14}$$

where n is the number of data points (or excitation frequencies) and (x_k, y_k) is the coordinate of the data points i.e. (excitation frequency, the amplitude of complex stiffness). The least squares regression method is used to calculate a total of 12 force coefficients, which includes direct and cross-coupled stiffness, damping, and virtual-mass coefficients, from real and imaginary parts of the bearing complex stiffness.

In the actual experiment, the estimated force coefficients include the force coefficients of the test bearing (fluid film) as well as the test-rig structure. The dry shake (baseline test) of the bearing stator, i.e. without oil and without running the rotor, delivers the stiffness

(K_{ij_s}) and damping (C_{ij_s}) coefficients of the support structure. The complex dynamic stiffnesses due to structural peripherals such as stabilizers bolts, static loader, and flexible pipes are subtracted from the combined bearing complex dynamic stiffnesses for an accurate estimation of the oil film properties. Later in the results section, the complex dynamic stiffness (H_{ij}) refers to that of a fluid film, $(H_{ij})_{fluid\ film}$, after subtracting the baseline properties $(H_{ij})_{baseline}$ unless otherwise stated.

$$(H_{ij})_{combined} = (H_{ij})_{fluid\ film} + (H_{ij})_{baseline}\ ;\ [i, j{=}x, y] \tag{15}$$

The baseline excitation test also delivers a bearing mass (M_b) which is used in the Eq (9) to calculate the complex dynamic stiffness (H).

Figure 18 shows the real and imaginary part of the complex dynamic stiffness $(H)_{baseline}$ from the dry shake test of the bearing stator. Table 7 lists the baseline force coefficients estimated from the complex dynamic stiffness $(H)_{baseline}$ along with other structural properties. The measured structural stiffnesses are quite low amounting to (1.2 MN/m ± 100%) and (3.5 MN/m ± 40%) along the *x* and *y*-direction respectively, and the damping coefficients are about (15 kNs/m ± 25%) along both the directions. The estimated mass of the bearing stator is about (33 ± 4) kg along the *x*-direction and about (34 ± 3) kg along the *y*-direction. The estimated stator mass (M_b) is calculated by inputting a guess magnitude in Eq. (9) until the slope of real part of the direct complex dynamic stiffness, $\mathrm{Re}(H_{ij})_{baseline} \rightarrow (K_{ij\_s} - \omega^2 M_{ij\_s})$, becomes null. The actual measured mass of the bearing stator with the end caps and instrumentation is about 24 kg.

The parameter identification procedure ignores the data at 60 Hz and its multiples, and the operating synchronous speed frequency (in most cases) due to electrical noise and run out.

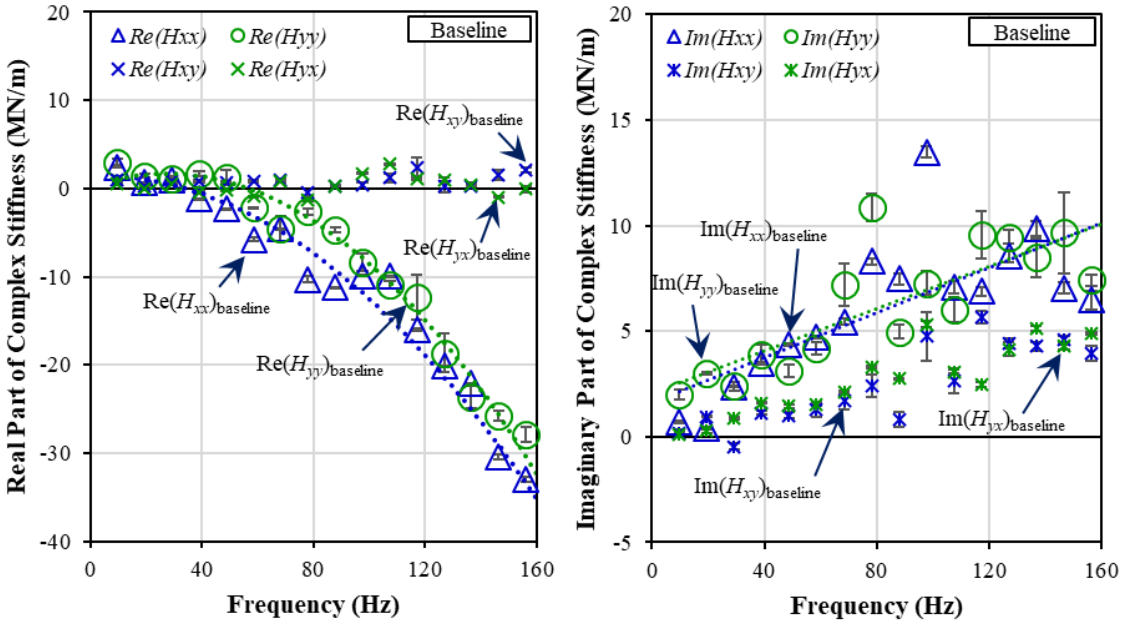

(a) Re(H)$_{baseline}$ **(b) Im(H)$_{baseline}$**

Figure 18. Baseline (oil free) complex dynamic stiffness (H)$_{baseline}$ vs. excitation frequency (Hz). [Left] Real (H)$_{baseline}$ and [right] Imaginary (H)$_{baseline}$ parts.

Table 7. Experimental baseline structural properties.

K_{xx_s}	1.2 ± 1.2 MN/m
K_{yy_s}	3.5 ± 1.3 MN/m
C_{xx_s}	15 ± 4 kNs/m
C_{yy_s}	15 ± 4 kNs/m
$(M_{bx})_s$	33 ± 4 kg
$(M_{by})_s$	34 ± 3 kg

K_{load_spring}	0.26 MN/m
Actual stator mass (bearing stator + accessories)	24 kg
Natural frequency of structure	~ 220 Hz

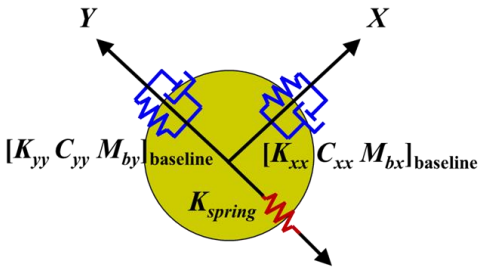

6.4 Steady State and Dynamic Load Excitation Tests

After the baseline excitation test, the lubricant (ISO VG 32) is supplied to the test bearing with a set oil flow rate. Two hydraulic shakers center the bearing with respect to the shaft. Thereafter an air motor is slowly accelerated to a pre-determined rotor speed, as per the test matrix in Table 2. The oil inlet temperature is maintained at ($T_{in} = 49 \pm 0.5$) °C throughout all the tests by a combined operation of two heat exchangers i.e. an air-cooled cooler and oil heater. The heated oil and the spinning rotor dragging the oil act to increase the temperature of the bearing and test rig which initially achieves a thermal steady state in about 45-60 minutes. Next, the pneumatic loader applies a static load on the bearing as soon as the system achieves the desired rotor speed.

For subsequent test points, the time taken to achieve thermal steady state reduces to 10-20 minutes based on operating conditions. Figure 19 presents a timeline of sensor readings for rotor speed, applied static load and pad temperature for operation at 6 krpm, and changes in applied load from 700 to 2800 N while operating with 100% nominal flow. The pad temperature (measured on loaded pad #4) stabilizes in about 10-15 minutes after an increase in applied load from 700 to 1400 N, as shown in Figure 19. A similar time frame is observed for most operating conditions in this study.

Upon achieving thermal equilibrium for a particular operating condition, the Data Acquisition System (DAQ) acquires test data from all the sensors for the static load performance of the bearing. Subsequently, a separate program performs a dynamic load excitation test by inputting and measuring an excitation voltage to the shaker and measuring the dynamic response from the eddy-current sensors and accelerometers. The dynamic measurements are sampled at 10,000 Hz. The load excitation test shakes the bearing stator for 10 times (each iteration has 32 waveforms) in each direction and it lasts for about 75 seconds.

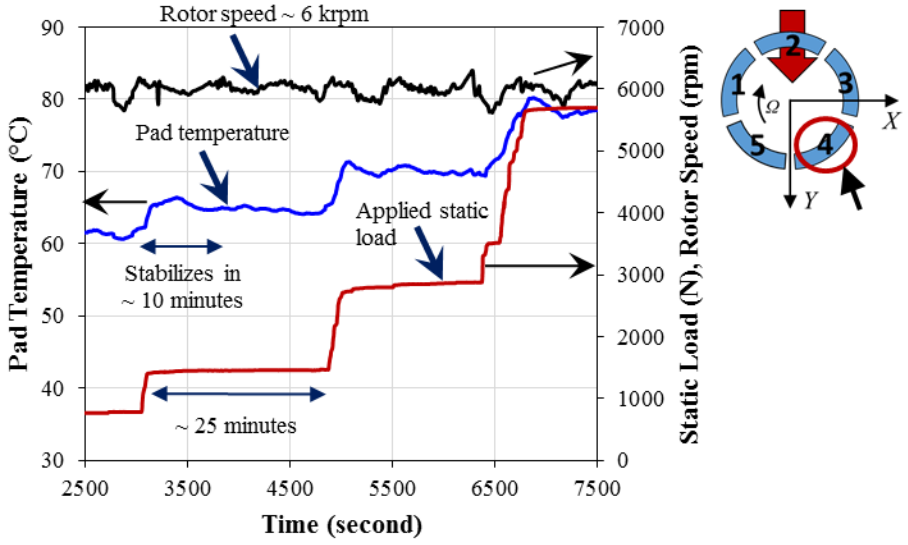

Figure 19. Example of the timeline of rotor speed (rpm), applied static load (N) and pad temperature (°C) measured on pad #4 at 75% location for operation at 6 krpm, applied static load from 700 to 2800 N (LBP) and 100% nominal flow.

6.5 Data for Prediction Model

The XLTPJB® [12] model utilizes a thermo-hydrodynamic (THD) analysis or thermo-elasto-hydrodynamic (TEHD) analysis to deliver bearing static and dynamic force performance predictions. The model accounts for both pad and pivot flexibility and includes temporal fluid inertia effects in the film, thermal and pressure induced deflection of the pads, and an improved thermal mixing model in a feed groove region [12, 16, 17].

Table 8 presents the geometry parameters, lubricant properties and analysis option utilized to generate prediction results from the physical model. The calculated preload (m) at 25°C is 0.42 ± 0.03 based on bearing cold clearance (62.5 ± 2.5 µm) and pad clearance (112 ± 5 µm). An input preload in the model is based on the hot bearing clearance measurements and increases with an increase in the operating shaft speed.

Table 8. Bearing geometry, lubricant, and operating conditions for analysis.

Bearing Geometry	
Rotor Diameter	0.1016 m
Bearing Axial Length	0.0406 m
Number of pads on bearing	5
Pad leading edge	22.50º
Pad thickness	0.0124 m
Preload (m) @ 25ºC	0.42 ± 0.03
@ 3, 6, 9, 12, 14, 16 krpm	0.44, 0.46, 0.48, 0.51, 0.52, 0.53
Pad arc length	63º
Pad radial clearance (C_p) @ 25ºC	0.112 ± 0.005 mm
Bearing radial clearance (C_r) @ 25ºC	0.0625 ± 0.00025 mm
Mass of each pad	0.25 kg
Pad moment of inertia about pivot	1.14 kg.cm^2
Pivot and socket nominal radius	0.0254 m
Lubricant (ISO VG 32) Properties	
Supply pressure	Measured (0.07-0.37 bar)
Cavitation pressure	0.00 bar
Supply temperature	49ºC
Viscosity at supply temp. (25ºC)	19.7 cP
Density	849 kg/m^3
Specific Heat	1990 J/kg °C
Thermal conductivity	0.13 W/m°C
Viscosity temperature coef.	0.0296 1/°C

Table 8 Continued.

Analysis option	
Fluid Inertia Option	Accounts for fluid inertia effects
Thermal Analysis Type - Known sump temperature - Pad thermal conductivity - Reynolds number in the back of pad - Housing inner diameter - Groove heat convection coefficient	Heat convection model by Haussen Measured (50-74ºC) 42.6 W/m°C 5000 (default) 0.1448 m 1750 W/m^2 °C (default)
Analysis Model	Thermo-hydro-dynamic (THD)
Pivot-type -Radius of pivot and housing -Young's modulus of pivot and housing -Applied radial load(W) vs. pivot deflection(δ) function	Sphere on a sphere 0.0254 m 207 GPa $W = 6E10^{13}\,\delta^2 + 6E10^{8}\,\delta$ -52 N
Groove Lubricant mixing model - Groove mixing efficiency (C_{gr}) - Total supply flow rate	 0.5-0.6 Measured (3.65-19.45 LPM)

7. STATIC FORCE CHARACTERISTICS: TEST RESULTS AND DISCUSSION

This section presents and discusses the static force performance of the test bearing at various operating conditions such as static applied load, shaft rotational speed, oil supply flow rate and temperature. The static performance parameters include shaft eccentricity and attitude angle, oil temperature rise, pads temperature rise, drag torque and power loss.

7.1 Nominal Oil Flow Rate

The nominal (100%) oil supply flow rate ($\dot{Q}$) for bearing operation at each speed is a function of rotor speed, bearing geometry and oil properties, and it is not dependent on the applied load. The actual oil flow rates are proprietary to the sponsor.

7.2 Exit Oil Temperature Rise

The oil supplied to the bearing is at a measured temperature (T_{in}) of 49.0 ± 0.5 ºC (120ºF). After lubricating the pads, a warm oil exits the test bearing along an axial plane through the end seals. Two thermocouples located on each side of the bearing discharge, DE and NDE side as shown in Figure 9, measure the exit oil temperature (T_{exit}). Recall, the DE and NDE refer to the drive end side and non-drive end side, respectively.

Figure 20 presents the measured oil temperature-rise ($\Delta T = T_{exit} - T_{in}$) at the bearing exit plane on each side (DE and NDE) and the arithmetic average of both DE and NDE sides temperatures versus specific load for operation at five rotor speeds (6 to 16 krpm) and 100% nominal oil flow rate. The discharge oil temperature rise at the exit plane does not vary significantly with an increase in applied static load, whereas the oil temperature rises consistently with an increase in rotor speed. Additionally, the measured exit oil temperature rise is higher on the DE side (ΔT_{DE}) compared to the NDE side (ΔT_{NDE}), particularly at surface speed > 48 m/s (9 krpm). Under 1.0 MPa specific load, the oil temperature rises from 8 ºC to 27 ºC (ΔT = 19 ºC) on the DE side, and from 9 ºC to 25 ºC (ΔT = 16 ºC) on the NDE side with an increase in rotor speed from 6 krpm (32 m/s) to 16

krpm (85 m/s). The error bars in Figure 20 (a) and 21 (b) denote the measurement uncertainty (± 0.5 ºC), while those in Figure 20 (c) denote the difference in temperatures measured on the DE and NDE sides (ΔT_{DE} - ΔT_{NDE}).

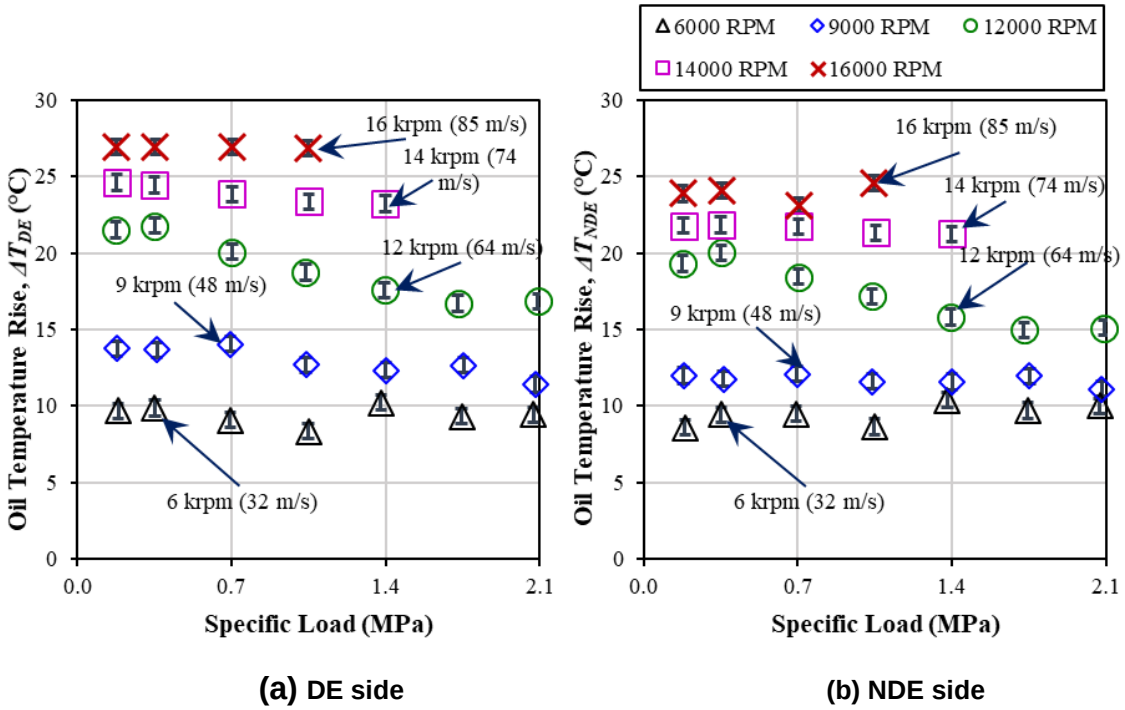

(a) DE side (b) NDE side

Figure 20. Measured oil temperature-rise (°C) at the discharge plane on (a) drive end side (DE), (b) non-drive end side (NDE) and (c) arithmetic average of both sides vs. specific load (MPa) for operation at rotor speed 6 to 16 krpm (32-85 m/s) and 100% nominal flow. (Oil supply temp.=49°C)

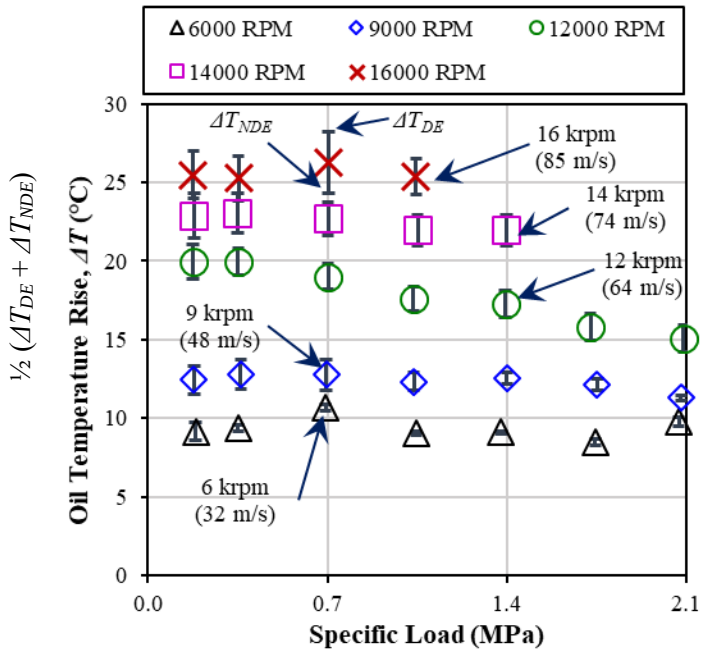

(c) Average temperature rise

Figure 20 Continued. Measured oil temperature-rise (°C) at the discharge plane on (a) drive end side (DE), (b) non-drive end side (NDE) and (c) arithmetic average of both sides vs. specific load (MPa) for operation at rotor speed 6 to 16 krpm (32-85 m/s) and 100% nominal flow. (Oil supply temp.=49°C)

Figure 21 compares the average oil temperature rise measured at the bearing exit plane for operation with the test bearing supplied with oil flow rates at 27%, 50%, 100% and 150% of nominal flow. The test conditions include operation at a surface speed of 48, 64 and 74 m/s (9, 12 and 14 krpm), and under a specific load of 0.35 and 1.0 MPa. On reducing the oil flow rate to 50% of nominal, ΔT increases by 4 ºC, whereas on increasing the oil flow rate to 150% of nominal, ΔT lowers by 2 ºC for operation at 74 m/s and under specific load of 0.35 MPa and 1.0 MPa. The ΔT results on changing the oil flow rate at 48 m/s and 64 m/s are similar to those observed at 74 m/s or with insignificant variation.

For 27% of nominal flow, ΔT is lower by 8ºC at 12 krpm (64 m/s) and under 0.35 MPa specific load as compared to those at nominal (100%) flow rate. However, the oil supply temperature rose up to 61ºC at the bearing entrance for such a low oil flow rate i.e. the operating conditions are out of the normal test conditions.

In theory, the supplied oil flow reduction decreases the oil film thickness and thus causing a larger shear drag force and a temperature rise in the oil film. Conversely, an increase in oil flow will lower the oil temperature at the bearing discharge planes, up to certain extent, due to the removal of dissipated heat in the oil film [34].

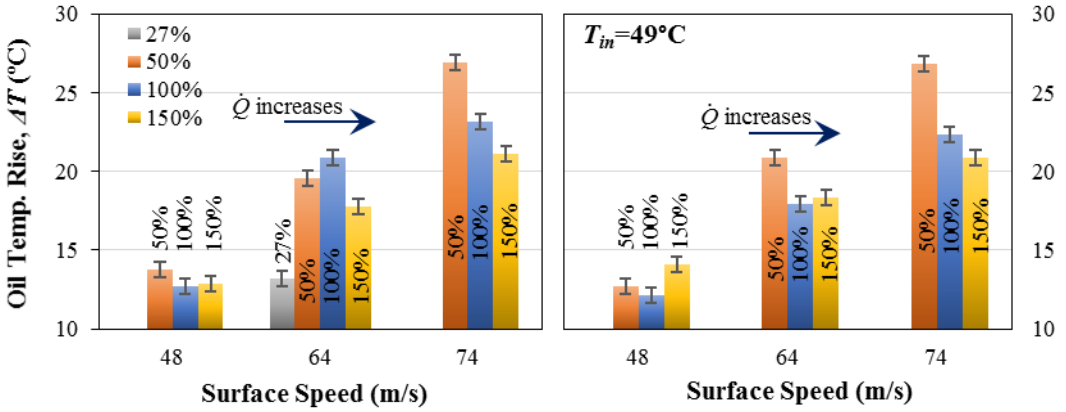

(a) Specific load: 0.35 MPa **(b) Specific load: 1.0 MPa**

Figure 21. Measured discharge oil temperature rise (°C) vs. surface speed (48, 64 and 74 m/s) for operation under a specific load of (a) 0.35 MPa and (b) 1.0 MPa, and at four oil flow rates (27%, 50%, 100%, and 150%). [Average of temperatures on the DE and NDE sides]

7.3 Shaft Eccentricity and Attitude Angle

The shaft static equilibrium position (SEP) or eccentricity (e) at a particular operating condition is obtained from the eddy-current displacement sensors (x_s, y_s) along the x and y directions. To obtain e, a distance between the two coordinates i.e. the shaft center (x_s, y_s) and the bearing center (x_c, y_c) is calculated as

$$e = \sqrt{(x_s - x_c)^2 + (y_s - y_c)^2} = \sqrt{e_x^2 + e_y^2} \tag{16}$$

The attitude angle (φ) is a measure of shaft motion in a bearing perpendicular to the load axis (y-direction) and is calculated from the shaft eccentricity along the x and y-axes as,

$$\varphi = \tan^{-1}\left(\frac{e_x}{e_y}\right) \tag{17}$$

Figure 22 depicts the loci of the shaft position for operation at four shaft rotational speeds and under an increasing specific load (LBP orientation). The coordinate (e_x, e_y) indicates the shaft eccentricity along the x and y-axes. The shaft position is referenced to a zero-static load condition which is designated as coordinate (0, 0) in Fig. 22. Upon increasing the static load on the bearing, the journal moves downward along the $+y$ direction. The shaft motion along the x-direction indicates cross-coupled force in the bearing and will be reflected in attitude angle. Please note during an actual test in this study, the bearing floats (moves) around the stationary shaft.

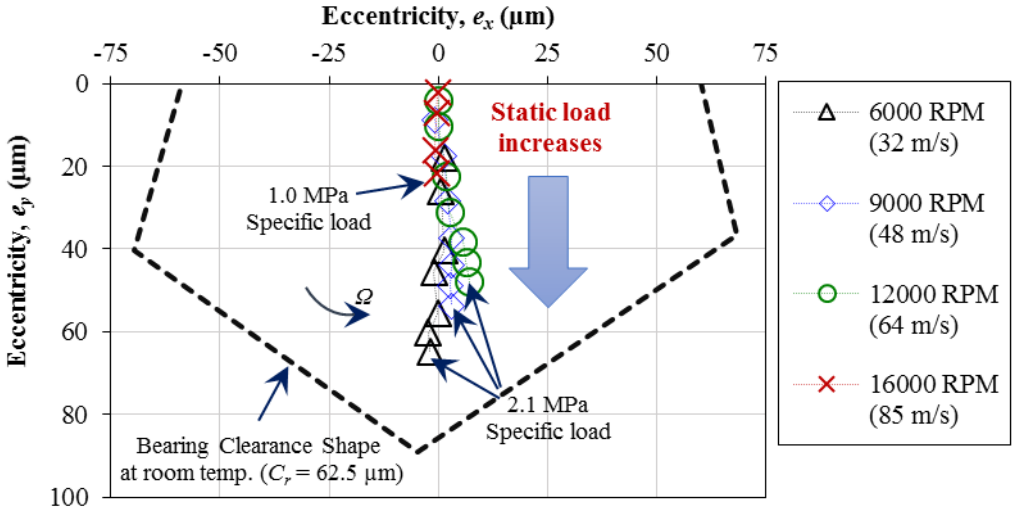

Figure 22. Measured shaft centerline as a function of applied load (along *y* direction) for operation at four rotor speeds (3, 9, 14 and 16 krpm).

Calculation of the shaft eccentricity and attitude angle is referenced to a zero-load condition for operation at rotor speed up to 9 krpm (48 m/s). At rotor speed > 9 krpm, the air-turbine shows a high synchronous speed vibration on the flexible coupling. However, a measured shaft position under a light applied load (0.1-0.4 MPa) delivers a good estimate of the operational bearing center at the rotor speed > 9 krpm. Refs. [15, 27] report

calculating the shaft eccentricity and attitude angle based on a bearing center obtained through cold and hot clearance measurements. However, based on the tests in this study, the actual operating bearing center (referred to a zero-static load condition) differs from the bearing center obtained from *cold* and *hot* clearance measurements.

Figure 23 presents the measured and predicted shaft eccentricity (e) as a function of bearing specific load, $W/(LD)$, for operation at five rotor speeds (6-16 krpm) and nominal (100%) oil flow rate. The shaft eccentricity depends on both rotor speed and applied static load. However, the eccentricity is a non-linear function of the applied static load which denotes an increase in pad-pivot structure stiffness with the load. For example, under 1.0 MPa specific load, the shaft eccentricity decreases from 43 μm to 22 μm (by 50%) with an increase in rotor speed from 6 krpm (32 m/s) to 16 krpm (85 m/s). However, at a constant rotor speed of 9 krpm (48 m/s), the shaft eccentricity increases from 9 μm to 54 μm (6 fold) with an increase in specific load from 0.17 MPa to 2.1 MPa. The shaft eccentricity at 6 krpm and 2.1 MPa is about 65 μm. Recall the hot radial clearance (C_r) of the test bearing at 50°C is 58.5 μm ($C_d = 2C_r = 117$ μm). For a LBP bearing, the shaft eccentricity can exceed the bearing radial clearance due to tilting motion of the pads.

The THD model predicts a shaft eccentricity that correlates well with the measured results for most operating conditions; except for operation at 6 krpm (32 m/s) which is under predicted by the model.

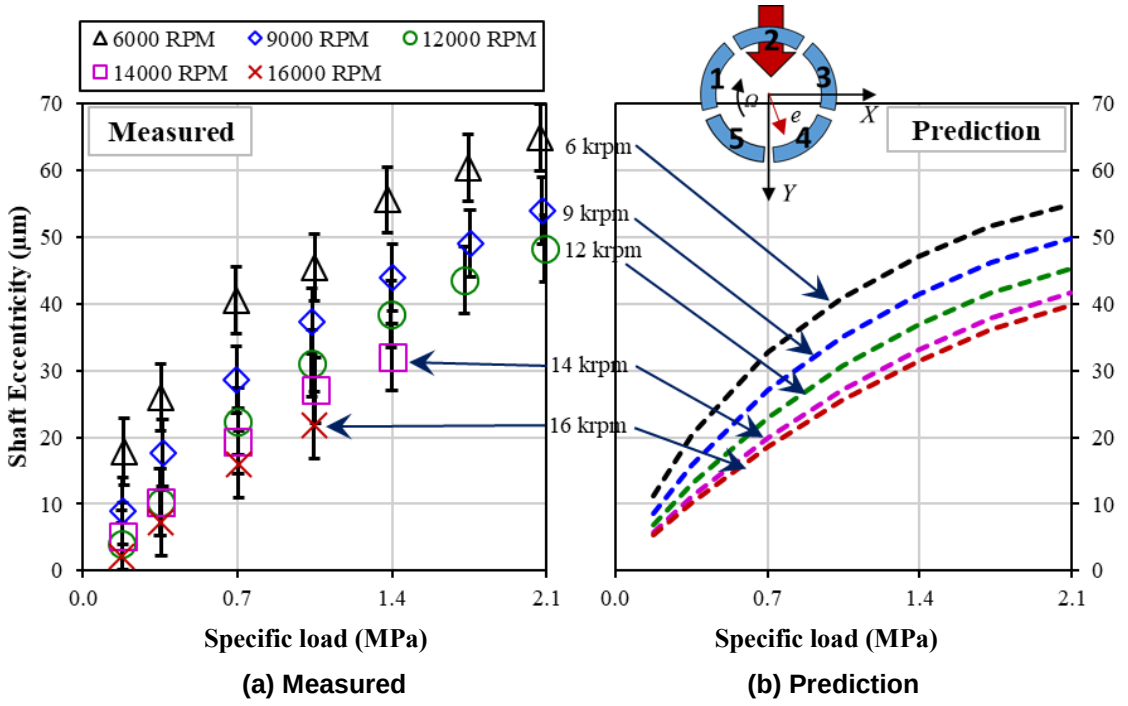

Figure 23. (a) Measured and (b) predicted shaft eccentricity (µm) vs. specific load (MPa) for operation at six rotor speeds (3 to 16 krpm) and 100% nominal flow. [C_r = 62.5µm]

Figure 24 presents a comparison of measured and predicted shaft eccentricity as a function of the Sommerfeld number (S). Recall, the Sommerfeld number (S) is a dimensionless parameter relating bearing static performance characteristics,

$$S = \frac{\mu N L D}{W}\left(\frac{R}{C_r}\right)^2 \tag{18}$$

where $\mu = \mu_{ref}\ e^{-\alpha_v(T_{eff} - T_{ref})}$ is an effective fluid viscosity[10], N = shaft speed (rev/s), D = shaft diameter, W = applied static load, and C_r = cold bearing radial clearance (m). As shown in Figure 24, the test at low rotor speed (< 9 krpm) and under high specific load (> 1.4 MPa) falls in a low range of the Sommerfeld number ($S < 5$) and thus results in a highly eccentric shaft position ($e > 50$ µm), and vice-versa.

[10] μ = f (T_{eff}) is an effective viscosity at effective temperature [$T_{eff} = T_{in} + ¾\ (T_{exit} - T_{in})$]

The shaft eccentricity increases with a reduction in S, i.e., increasing the static load (W) and decreasing the shaft speed (N). The measured and predicted shaft eccentricity (e) follow a similar trend for S = 0.3 to 10, and thus match well with each other.

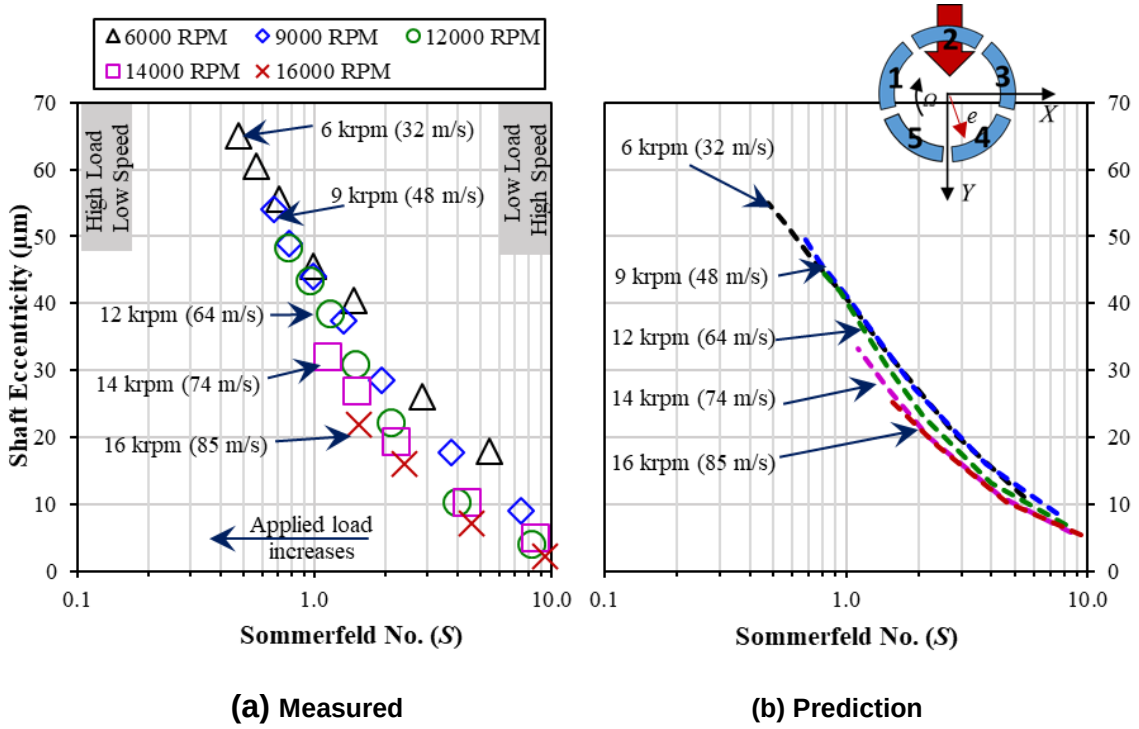

Figure 24. (a) Measured and (b) predicted shaft eccentricity (μm) vs. Sommerfeld number (*S*) for operation at various shaft surface speed (16 to 85 m/s), specific load (0.17 to 2.1 MPa), and 100% nominal flow rate.

Figure 25 presents the attitude angle (φ) as a function of specific load (0.17 to 2.1 MPa) for operation at rotor speed ranging from 6 to 16 krpm (32-85 m/s) and nominal (100%) oil flow rate. Typically, the attitude angle is small (< 10°) for the set operating conditions. The highest attitude angle is about 9º for operation at 12 krpm and a high specific load (> 1.4 MPa). The measurement uncertainties are large at a low applied load (< 0.7 MPa) due to the small eccentricities (e_x and e_y) and a constant measurement error of ±2.5 μm. The small attitude angle indicates low or negligible cross-coupling force which is a typical characteristic of the TPJB.

A variation in oil supply flow rate (50-150%) causes an insignificant change in the attitude angle (not shown) which remains fairly small (< 10°) for operation up to 14 krpm (74 m/s) and 1.0 MPa specific load.

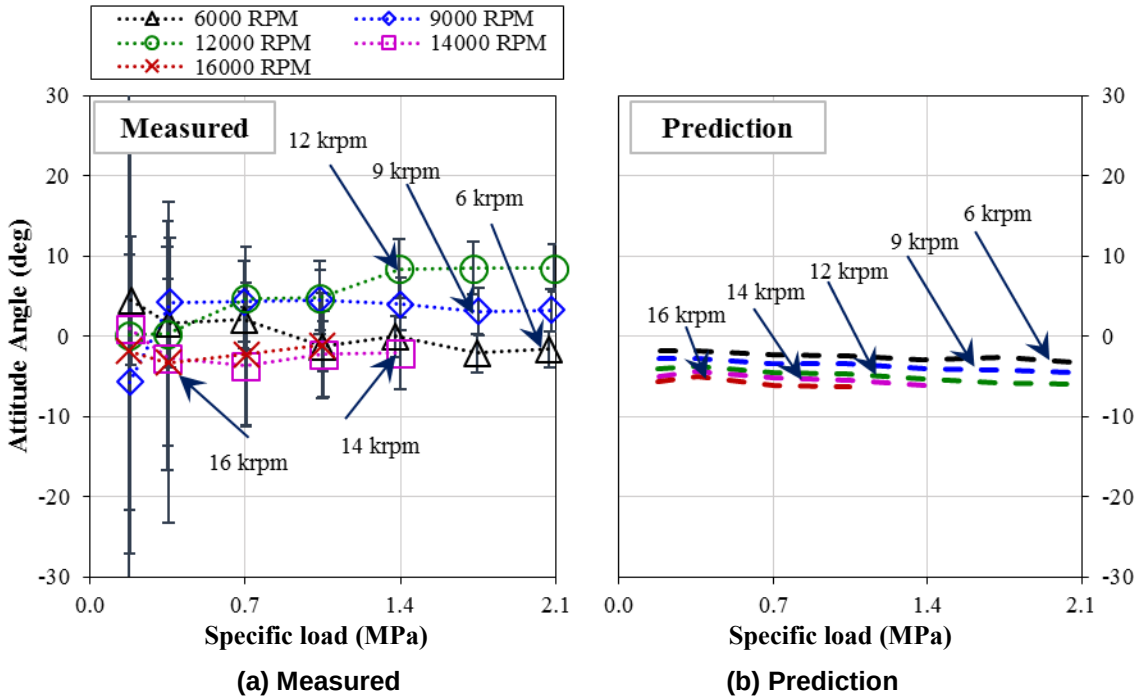

Figure 25. (a) Measured and (b) predicted attitude angle (degree) vs. specific load (MPa) for operation at five rotor speeds (6, 9, 12, 14 and 16 krpm) and 100% nominal flow.

Figure 26 presents a comparison of the shaft eccentricity for operation with the test bearing supplied with oil flow rate at 27% to 150% of nominal flow. The test conditions are the surface speed of 48, 64 and 74 m/s (9, 12 and 14 krpm), and under a specific load of 0.35 and 1.0 MPa[11]. For operation at 12 krpm (64 m/s) and 1.0 MPa specific load, the shaft eccentricity compared to that at 100% nominal flow increases by 22% at 50% of nominal flow and increases by 9% at 150% of nominal flow. Similar shaft eccentricity

[11] As per sponsor's requirement, the test data for operation at various oil flow rate (50% and 150% of nominal flow rate) is only up to 1.0 MPa specific load (not higher).

trends are observed for operation at a rotor speed of 9 krpm (48 m/s) and 14 krpm (74 m/s) and with a specific load of 0.35 MPa.

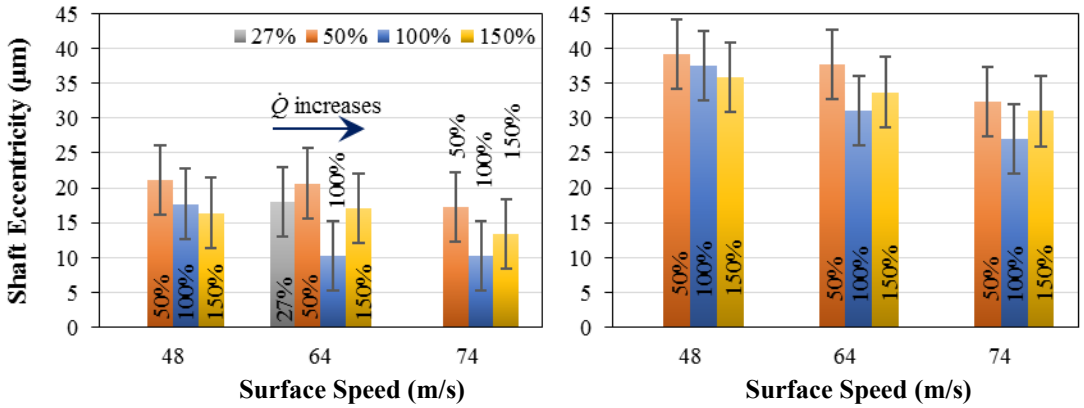

Figure 26. Measured shaft eccentricity (μm) vs. shaft surface speed (48, 64 and 74 m/s) for operation under specific load of (a) 0.35 MPa and (b) 1.0 MPa, and for four oil flow rates (27%, 50%, 100%, and 150% of nominal flow).

The model predicts the shaft eccentricity to increase for operation with reduced oil flow rate (50%) and to decrease for operation with increased oil flow rate (150%). As expected, the shaft eccentricity for operation at 50% (reduced) oil flow rate is higher compared to that at a nominal flow rate due to the reduced oil film thickness on the loaded pads. However, the shaft eccentricity for operation at 150% of nominal flow, in most cases, is also large compared to that for 100% nominal flow. This increase may be attributed to an excess amount of cold oil supplied to the unloaded pads as compared to the loaded pads. From a moderate load to a high load, the lubricant faces a larger resistance to enter the loaded pads as compared to the unloaded pads due to the higher hydrodynamic pressure in the film lands [32]. Such difference between theory and measurement could be due to large measurement uncertainty (± 5 μm)

7.4 Drag Torque and Power Loss

The bearing drag power loss ($P_{measured}$) is calculated from the measured drag torque (T) and the shaft angular speed (Ω) as

$$\begin{aligned} P_{measured} &= P_{system} - P_{baseline} \\ &= (T_{system} - T_{baseline}) \times \Omega \end{aligned} \tag{19}$$

where P_{system} and T_{system} are the drive power and torque for the shaft supported on two ball bearings and test bearing, and $P_{baseline}$ and $T_{baseline}$ are the drive power and torque for the shaft with ball bearings (without test bearing), respectively. Typically, the measured baseline torque from the in-line torque sensor is about 0.5 Nm, and thus $P_{baseline}$ = 0.4 kW, for the test at 8 krpm.

For operation at 9 krpm rotor speed, the baseline torque was not measured due to a high amplitude synchronous speed vibration on the flexible coupling location. Hence, the baseline torque is estimated from a linear regression of the measured torque up to 8 krpm. The estimated baseline drive power for operation at 9, 12, 14 and 16 krpm are 0.5, 0.7, 0.8 and 0.9 kW, respectively.

Figure 27 presents the measured drag torque of the system versus shaft surface speed for operation under 0.35 MPa and 1.7 MPa specific loads and at a 100% nominal flow rate. The drag torque varies from 1 Nm at 3 krpm (16 m/s) to 8.5 Nm at 14 krpm (74 m/s).

Typically, in the present study, the measured torque increases by ≈ 0.1 Nm with a step increment of the specific load by 0.35 MPa for operation at each rotor speed. The measured drag torque for operation at < 9 krpm is identical for the bearing under both LBP and LOP orientations. Please note, the drag torque at 12 and 14 krpm refer to measurements with the bearing under a LOP orientation, and which may not change significantly compared to those under the LBP orientation (particularly at light load conditions). Moreover, a torque could not be measured for operation at 16 krpm (under both LBP and LOP) due to too large amplitude synchronous speed vibrations at the flexible coupling-torquemeter location, and hence operated without the torquemeter in place for its safety. Based on the

curve-fit, the estimated drag torque for operation at 16 krpm and under 0.35 MPa specific load is ≈ 9.5 Nm.

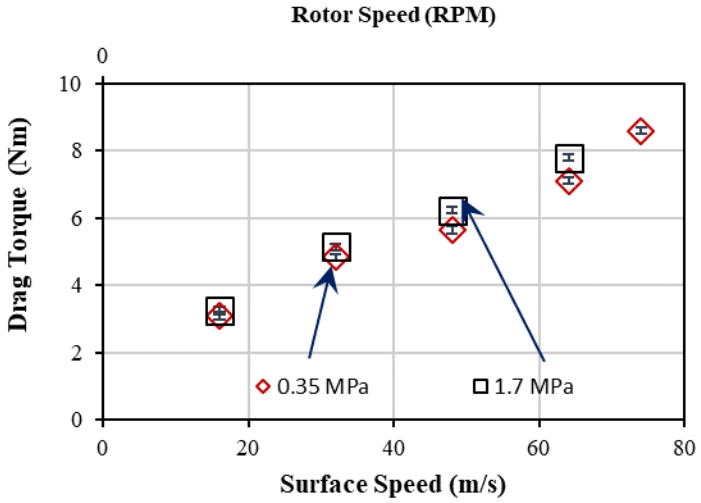

Figure 27. Measured drag torque (Nm) vs. surface speed (m/s) for operation at various specific load (0.35, 1.0 and 1.7 MPa) and 100% nominal flow.

The bearing drag power loss ($P_{estimated}$) is traditionally estimated from the amount of heat carried away by the lubricant from [35]

$$P_{estimated} = \frac{\rho\, C_p\, \dot{Q}}{\kappa}\,(\Delta T) \tag{20}$$

where $\dot{Q}$ is the volumetric flow rate supplied to test bearing, ΔT is the oil temperature rise at the bearing exit, ρ is oil density, C_p is oil specific heat, and κ is an empirical coefficient denoting the fraction of mechanical power removed by a supplied oil flow. Typically, the empirical coefficient (κ) is low (< 0.8) for a bearing with end seals, due to a high churning loss, and high for a bearing with an evacuated housing ($0.8 < \kappa < 1$).

Define a dimensionless drag power loss ($\overline{P}$) as

$$\overline{P} = \frac{P_{measured\ or\ estimated}}{P_{theory}} \tag{21}$$

where $P_{theory} = \dfrac{\Omega^2 D^3 L \mu}{8 C_r} (n_p \theta_p)$

Above μ = f (T_{eff}) is an effective viscosity at effective temperature [$T_{eff} = T_{in} + ¾ (T_{exit} - T_{in})$], and n_p and θ_p are the number of pads and pad arc length (radian), respectively.

Figure 28 depicts the dimensionless measured and estimated bearing drag power loss ($\overline{P}$) versus specific load (0.35 to 2.1 MPa) for operation at four rotor speeds (9-16 krpm) and 100% nominal flow. The drag power loss is mostly a function of shaft rotational speed and nearly independent of the applied load. For example, at 9 krpm (48 m/s), the measured drag power loss ($\overline{P}$) varies little (≈ 5%) with an increase in applied load from 0.17 to 2.1 MPa. Conversely, at 1.0 MPa specific load, the measured $\overline{P}$ increases from ≈ 0.9 to 1.3 (45% increase) with an increase in the rotor speed from 9 to 16 krpm (48 to 85 m/s).

The estimated drag power loss ($\overline{P}$), as shown in Figure 28, is also a function of rotor speed and nearly independent of the applied load. An empirical coefficient $\kappa = 0.8$ delivers a comparable drag power loss against the measured test data for operation up to 12 krpm (64 m/s). The estimated $\overline{P}$ at 14 and 16 krpm is about 1.37 and 1.5 which is around 20% and 25% larger than the measured power loss, respectively. Please note the supplied oil flow rate is not constant and increases with an increase in rotor speed and thus directly influences the estimated $\overline{P}$.

A flooded bearing (with end seals) has high churning losses due to the oil being pressurized in the housing [4], and which suggests a lower amount of heat carried away by the lubricant ($\kappa < 0.8$) compared to the one considered in this study ($\kappa = 0.8$).

Overall, the measured $\overline{P}$ is close (within 20%) to the theoretical magnitude (based on film shear stress) for the most test operating conditions. However, the estimated $\overline{P}$ with a single factor for κ (= 0.8) in Eq. (20) does not correlate with the theoretical magnitude,

especially for high rotor speed (>12 krpm) conditions. The estimated $\overline{P}$ delivers a greater drag power loss compared to the measured value and thus provides poor estimate. On the other hand, the XLTPJB model over predicts the dimensional drag power loss by ≈ 45% (max.) as compared to the direct measured drag power loss for most operating conditions (not all shown).

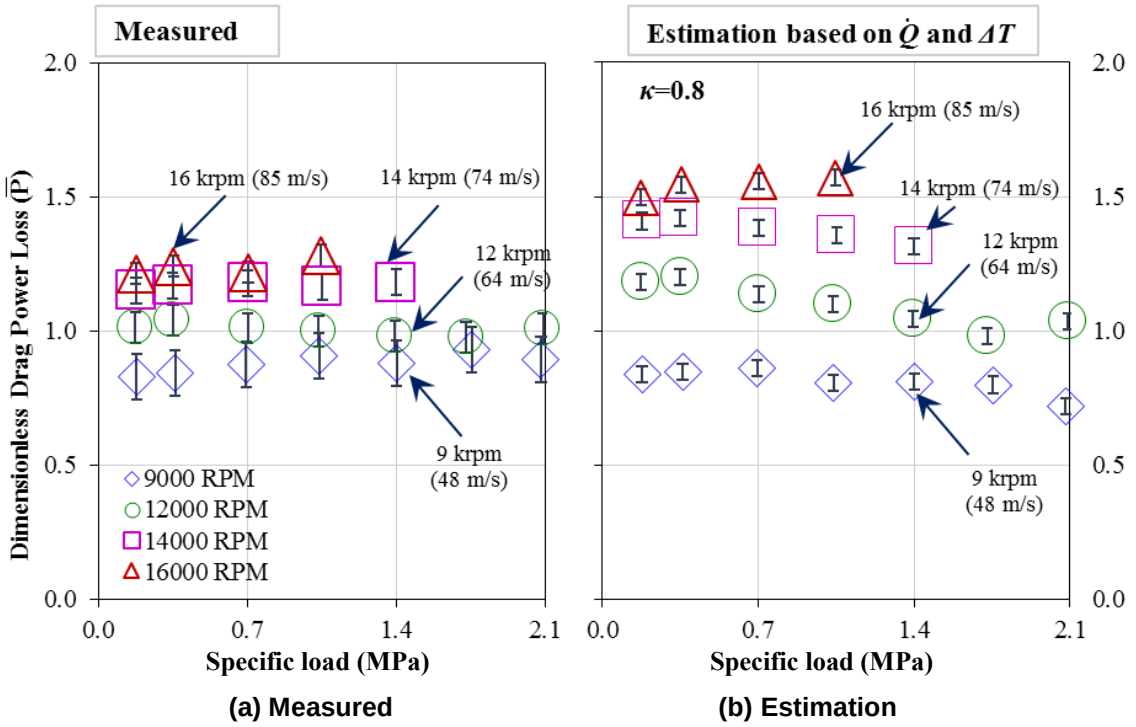

Figure 28. Measured and estimated dimensionless bearing drag power loss ($\overline{P}$) vs. specific load (MPa) for operation at five rotor speeds (6 to 16 krpm) and 100% nominal flow.

Figure 29 depicts the circumferential flow Reynolds number[12] (R_e) of the fluid flow inside the bearing clearance for operation at distinct rotor speeds, under various specific loads, and at 100% oil flow rate. R_e increases with an increase in shaft surface speed and

[12] Reynolds number (R_e) is a flow property that measures the ratio of inertial forces to viscous forces. $R_e = \frac{\rho \Omega R C_r}{\mu}$, where ρ=fluid density, C_r = *cold* bearing radial clearance. $R_e < 2000$ indicates laminar flow, and $R_e > 2000$ indicates turbulent flow.

is maximum at 16 krpm (R_e = 484). The fluid flow in the bearing clearance is laminar (R_e < 500) for all the operating conditions. The drag power loss is directly impacted by the flow condition and hence the knowledge of R_e is essential.

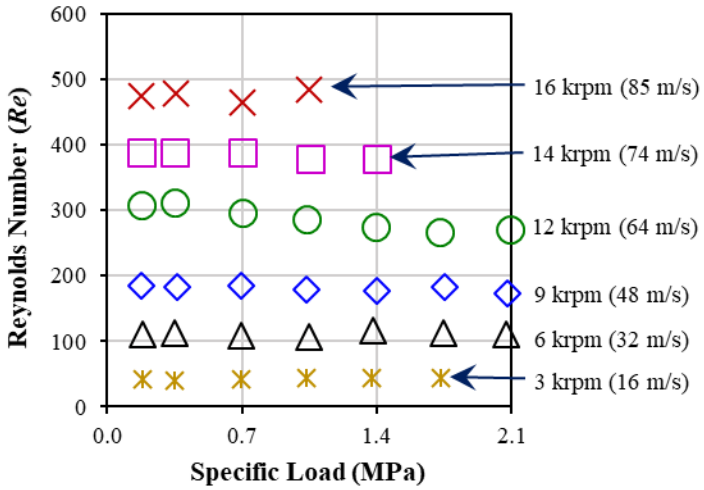

Figure 29. Circumferential flow Reynolds number (*Re*) vs. specific load for operation at various rotor speed (3-16 krpm) and 100% oil flow rate.

The drag torque measurement for operation at 9, 12, and 14 krpm and with various oil flow (50-150% of nominal flow) is unavailable due to high amplitude synchronous speed vibration as mentioned earlier. However, a few tests at a low rotor speed, up to 8 krpm (42 m/s), show the variation in measured drag power loss ($\overline{P}$) with changing oil flow rate (50% to 150%).

Figure 30 presents a comparison of the measured and estimated drag power loss ($\overline{P}$) for test at three surface speeds (16, 32 and 43 m/s), under 1.0 MPa specific load, and at three oil flow rates (50%, 100%, and 150%). On reducing the oil flow rate from 100% to 50% of nominal, the direct measured $\overline{P}$ slightly reduces by ≈ 15 % whereas the estimated reduces by ≈ 54%. The test results demonstrate that the direct $\overline{P}$ is less sensitive to supplied oil flow rate as compared to the estimated $\overline{P}$.

The XLTPJB® model predicts significant reduction in drag power loss by 20% (average) on reducing the oil flow rate by 50%, while it predicts increase in drag power loss by about 15% (average) on increasing the oil flow rate by 50% as compared to

nominal oil flow rate for operation at 9, 12 and 14 krpm rotor speed.

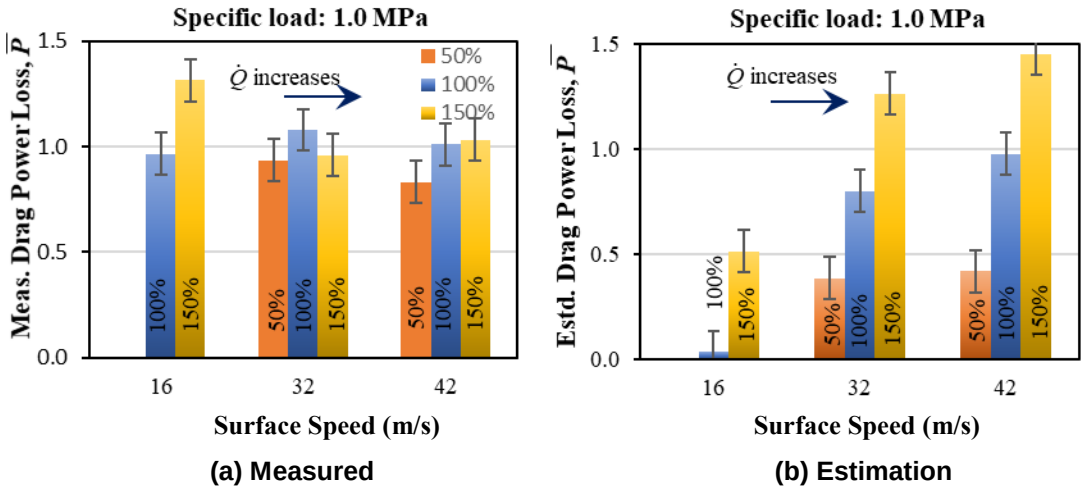

Figure 30. (a) Measured and (b) estimated dimensionless drag power loss ($\bar{P}$) vs. surface speed (16, 32 and 42 m/s) for operation at 1.0 MPa and three oil flow rates (50%, 100%, and 150%).

7.5 Bearing Pad Temperatures

A total of 30 embedded thermocouples at a depth of about 2.5 mm below a pad surface (pad thickness ≈ 9 mm) record its sub-surface temperature. Each steel pad has 6 thermocouples located circumferentially at 10%, 25%, 75% and 90% of a pad arc length, as shown in Figure 10. Note, pads # 4 and 5 are the loaded pads under a LBP orientation.

Define a dimensionless pad defect temperature (θ) as

$$\theta = \frac{T_{pad} - T_{in}}{T_{exit} - T_{in}} = \frac{\Delta T_{pad}}{\Delta T_{oil}} \tag{22}$$

where T_{pad} is the measured pad sub-surface temperature, and T_{in} and T_{exit} are the oil temperature at the inlet and outlet (average of DE and NDE sides) planes of the test bearing, respectively. The pad defect temperature (θ) delivers the rise in pad temperature (ΔT_{pad}) relative to the rise in oil temperature at the discharge (ΔT_{oil}) plane. For example, a test with ΔT_{oil} = 50ºC and $\theta \approx 2$ denotes an actual pad temperature rise of 100ºC.

Figure 31 depicts the pad defect temperature (θ) versus circumferential location in the

bearing for operation at three specific loads (0.35, 1.0 and 2.1 MPa), four rotor speeds (6, 9, 12 and 16 krpm), and 100% nominal flow. Each box in the graph represents the temperature measured in a particular pad, starting from pad 1 on the left to pad 5 on the right. At the leading edge (10% arc length) of each pad, the supplied (cold) oil produces a low pad surface temperature ($\approx T_{in}$). As the oil travels along the pad in the convergent wedge, the oil temperature rises due to viscous heating to produce high surface temperature near the trailing edge (75-90% arc length) of each pad.

Under a specific load of 0.35 MPa and at four surface speeds (32-85 m/s), $\theta = 0.5$ (less than 1) at the leading edge (10% and 25% pad arc length) in all five pads. $\theta \approx 0.5$ indicates that half of the oil temperature rise (ΔT_{oil}) occurs at a pad leading edge due to an excessive churning loss in the groove region between pads. For a test under 1.0 MPa specific load, $\theta > 1$ at the leading edge in pads 4 and 5 indicates excessive churning losses in the groove and hot oil carry-over from the upstream pad. It is interesting to note that the leading edge temperatures for all five pads are not identical at various operating conditions, as shown in Figure 31, which suggests an uneven oil flow distribution and unequal hot oil carry-over in all five pads, as discussed in Ref. [12].

The (near) maximum pad defect temperature (θ_{max}) is about 2.5 as measured on pad-5 (2^{nd} loaded pad) at 75% pad arc length for a test at 6 and 9 krpm and under 0.35 MPa specific load. As stated in a classic TPJB tutorial, "A good rule-of-thumb to record maximum temperature is to locate sensor at 75% location in a loaded pad" [4]. With an increase of specific load from 0.35 to 1.0 and 2.1 MPa at surface speed 32 m/s, θ_{max} increases from 2.5 to 3.5 and 3.9, respectively, on loaded pad-5, and from θ_{max} =1.8 to 3.2 and 3.8, respectively, on loaded pad-4. With an increase in shaft surface speed from 32 m/s to 85 m/s under a specific load of 1.0 MPa, θ_{max} reduces from 3.5 to 2.7. For operation under 2.1 MPa specific load, θ_{max} = 4.3 at 9 krpm (48 m/s) shaft speed and decreases to 3.9 at both 6 (32 m/s) and 12 krpm (64 m/s) shaft speed. The decrease in θ does not mean an actual drop in pad temperature. Recall, the oil temperature rise (ΔT_{oil}) for operation at 85 m/s is higher by ≈ 16ºC than that at 32 m/s, and which eventually produces high pad temperatures for operation at high speed.

Moreover, with an increase of specific load from 0.35 to 1.0 MPa and 2.1 MPa, θ_{max} over the unloaded pads changes insignificantly for operation at all surface speeds as shown in Figure 31. At a high specific load (> 1.0 MPa), the resistance of the fluid to enter a pad's leading edge is greater in the loaded pads as compared to those in the unloaded pads, and which results into more fresh oil flow available on the unloaded pads and to eventually cause a low θ over them [12].

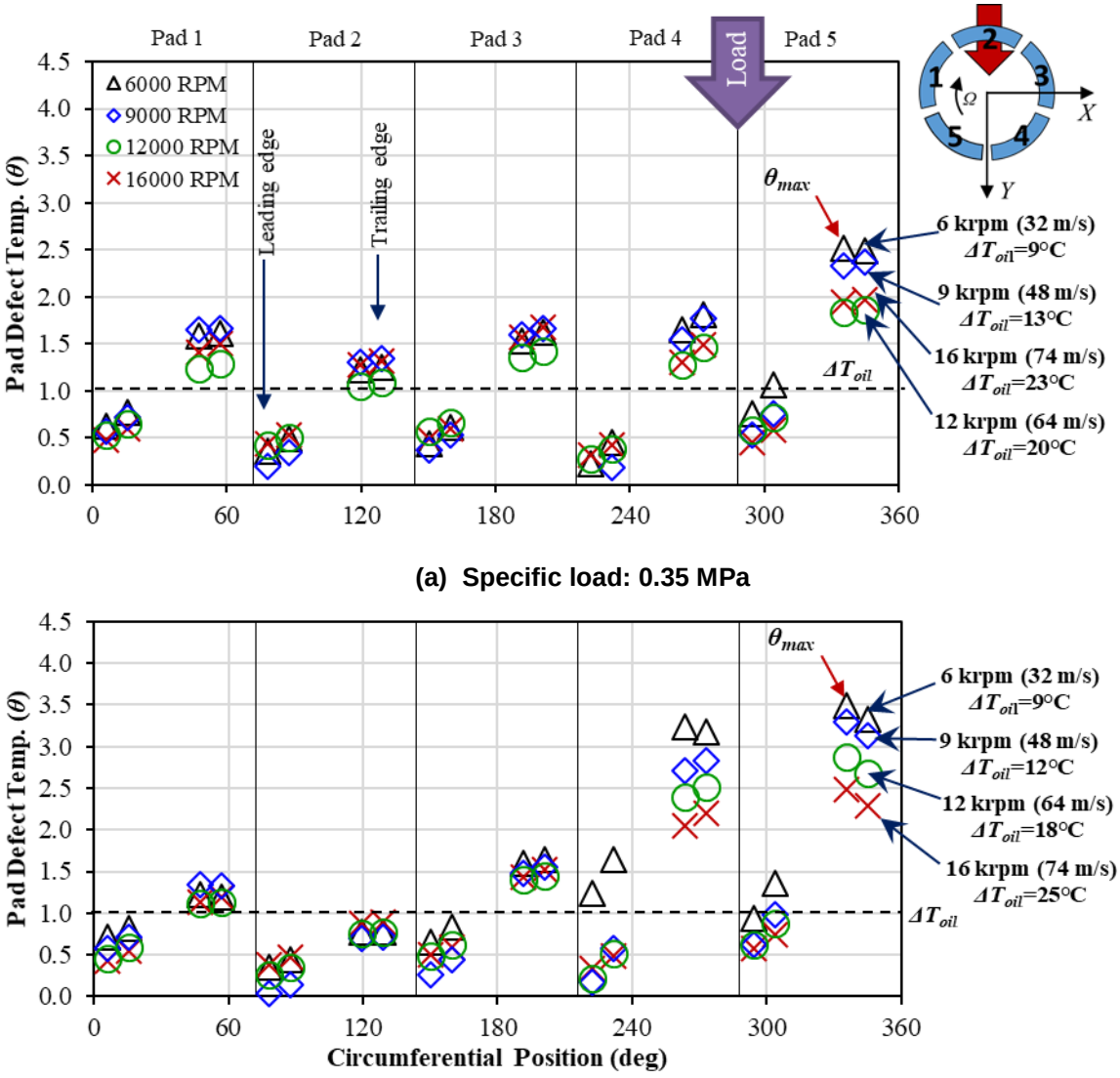

(a) Specific load: 0.35 MPa

(b) Specific load: 1.0 MPa

Figure 31. Measured pad defect temperature (θ) at 20 circumferential locations along mid-plane for operation under (a) 0.35 MPa, (b) 1.0 MPa and (c) 2.1 MPa specific load, at four rotor speeds (3 to 16 krpm), and 100% nominal flow rate.

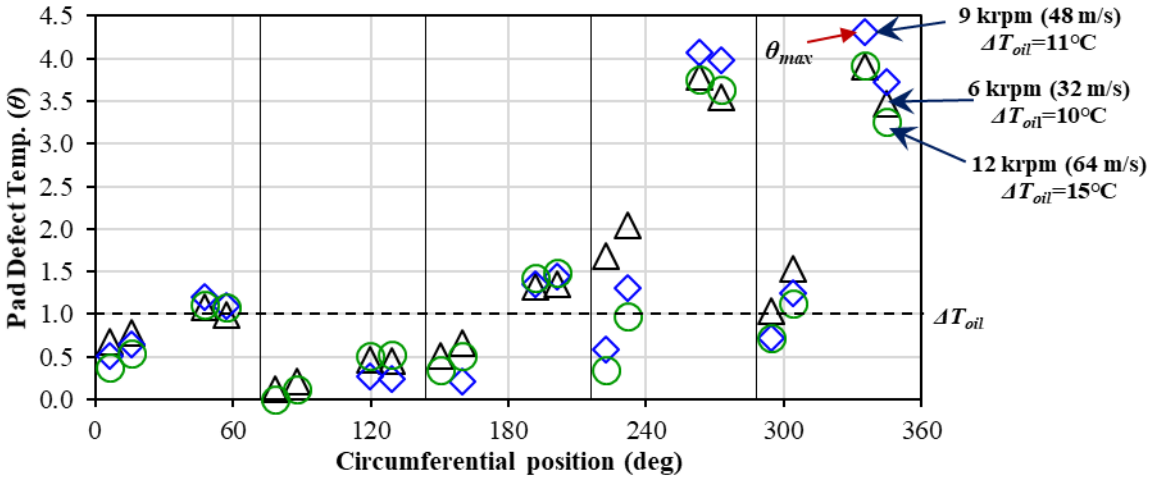

(c) Specific load: 2.1 MPa

Figure 31 Continued.

Figure 32 presents a comparison of measured and predicted maximum pad defect temperature (θ_{max}) in the test bearing at various operating conditions as a function of the Sommerfeld number (S). The test conditions include rotor operation at five speeds (6 - 16 krpm), under six specific loads (0.35 - 2.1 MPa), and 100% nominal oil flow rate. In most cases, θ_{max} locates on pad number 5 (75% arc length). The operation at high rotor speed and under a light load produce a large Sommerfeld number (S) and produces a low θ_{max} and vice versa. For S = 4, $\theta_{max} \approx 2$. As S decreases from 4 to 0.5 (i.e. decrease in shaft surface speed and increase in specific load), θ_{max} increases two-fold from ≈ 2 to 4. The model significantly over predicts θ_{max} for all S for operation below 12 krpm (64 m/s), whereas it predicts well for operation at 14 and 16 krpm when compared to the measured defect temperature (θ_{max}).

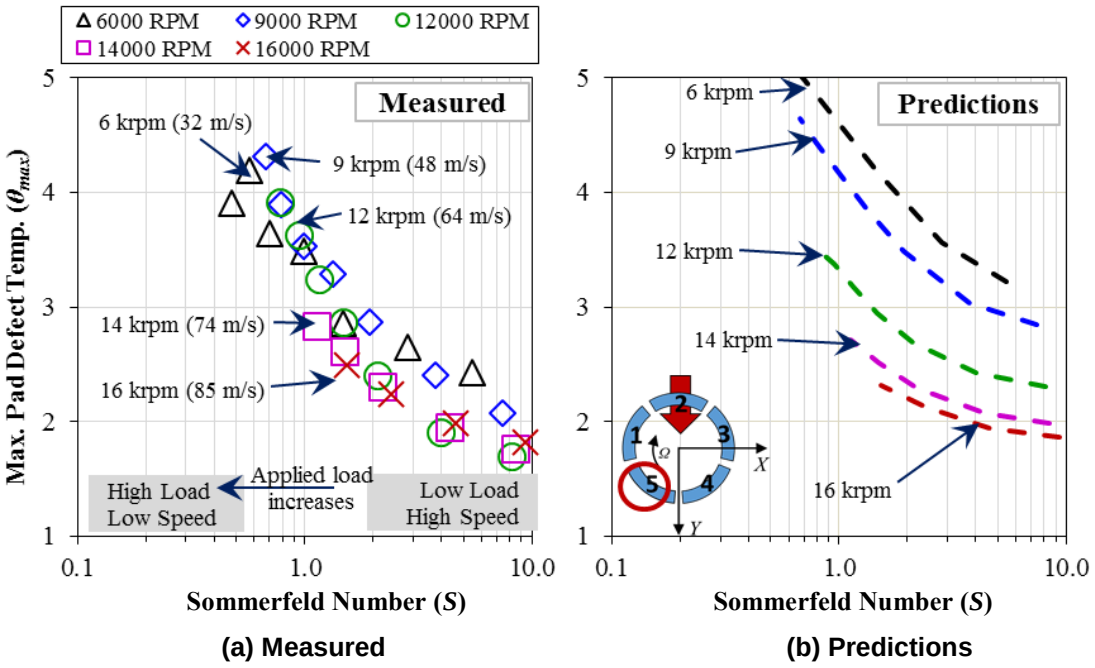

Figure 32. (a) Measured and (b) predicted maximum pad defect temperature (θ_{max}) vs. Sommerfeld number (S) for operation at five rotor speeds (6 to 16 krpm), under various specific load (0.17 to 2.1 MPa) and with 100% nominal oil flow rate. [Typically, θ_{max} locates on pad #5]

Figure 33 shows the pad defect temperature (θ) profile recorded by the axially located thermocouples (#3, #4 and #5) at 75% arc length location on each pad. The test conditions include a test at rotor speed up to 16 krpm (85 m/s) and under a specific load of 1.0 MPa. Please note NDE, C, and DE refer to the non-drive end, center (mid) plane, and drive end sides. The defect temperature in pads number 1, 3 and 5 have a difference of about 0.4 along the axial direction for operation at 16 krpm and under 1.0 MPa. This temperature difference increases with rotor speed (32 to 85 m/s) as shown in the figure. Pad #2 and #4 show a negligible temperature difference for most operating conditions, thus denoting both good rotor-pad alignment and an effective self-aligning characteristic of those pads.

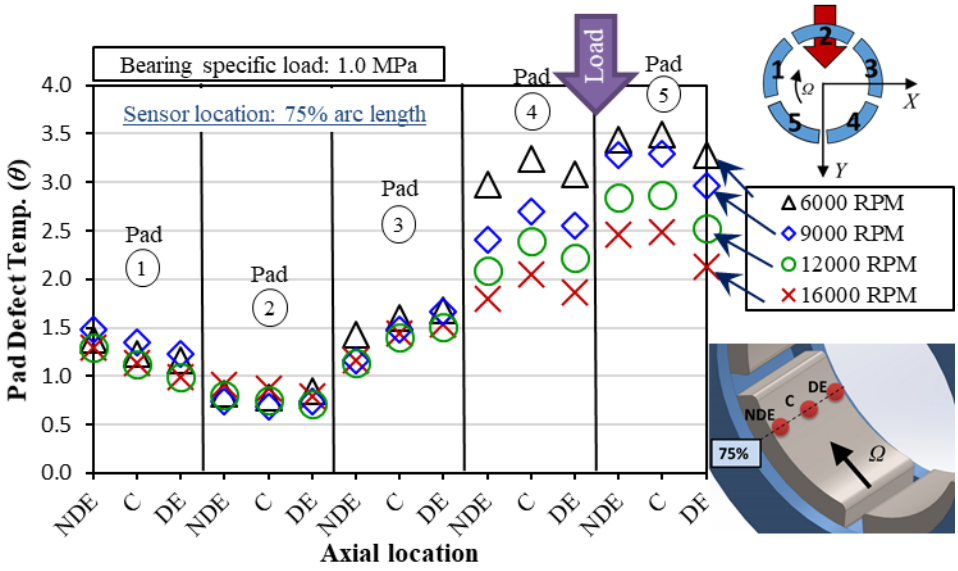

Figure 33. Pad defect temperature (θ) measured at 3 locations along an axial plane (at 75% arc length) for operation with a specific load of 1.0 MPa, at four rotor speeds (6, 9, 12 and 16 krpm) and 100% nominal flow. [NDE: non-drive end, C: center line, DS: drive end]

Figure 34 presents a comparison of the measured pads' defect temperature (θ) for operation with the bearing supplied with oil flow rate at 50%, 100% and 150% of nominal flow. The test conditions include the operation at a surface speed of 48, 64 and 74 m/s (9, 12 and 14 krpm), and under a specific load, $W/(LD)$, of 0.35, 0.7 and 1.0 MPa. On changing the oil flow rate to 50% and 150% of nominal value, θ varies by ± 0.3 (max.) compared to that at nominal oil flow rate. The increase or decrease in θ depends on the relative rise in oil temperature and pad temperature. A small change in θ as shown in the figure also indicates that a rise in pad temperature is likely proportional to a rise in discharge oil temperature. However, the actual pad temperature slightly increases (≈ 5°C max.) with a reduction in oil flow rate (50%) and decreases insignificantly (≈ 2°C max.) with an increase in oil flow rate (150%) compared to the pad temperature with nominal (100%) oil flow rate.

The XLTPJB® model predicts a rise in θ_{max} of about 15% on reducing the oil flow rate from 100% to 50%. On the other hand, the model predicts a decrease in θ_{max} of about 10% on increasing the oil flow rate by 50%.

(a) 9 krpm

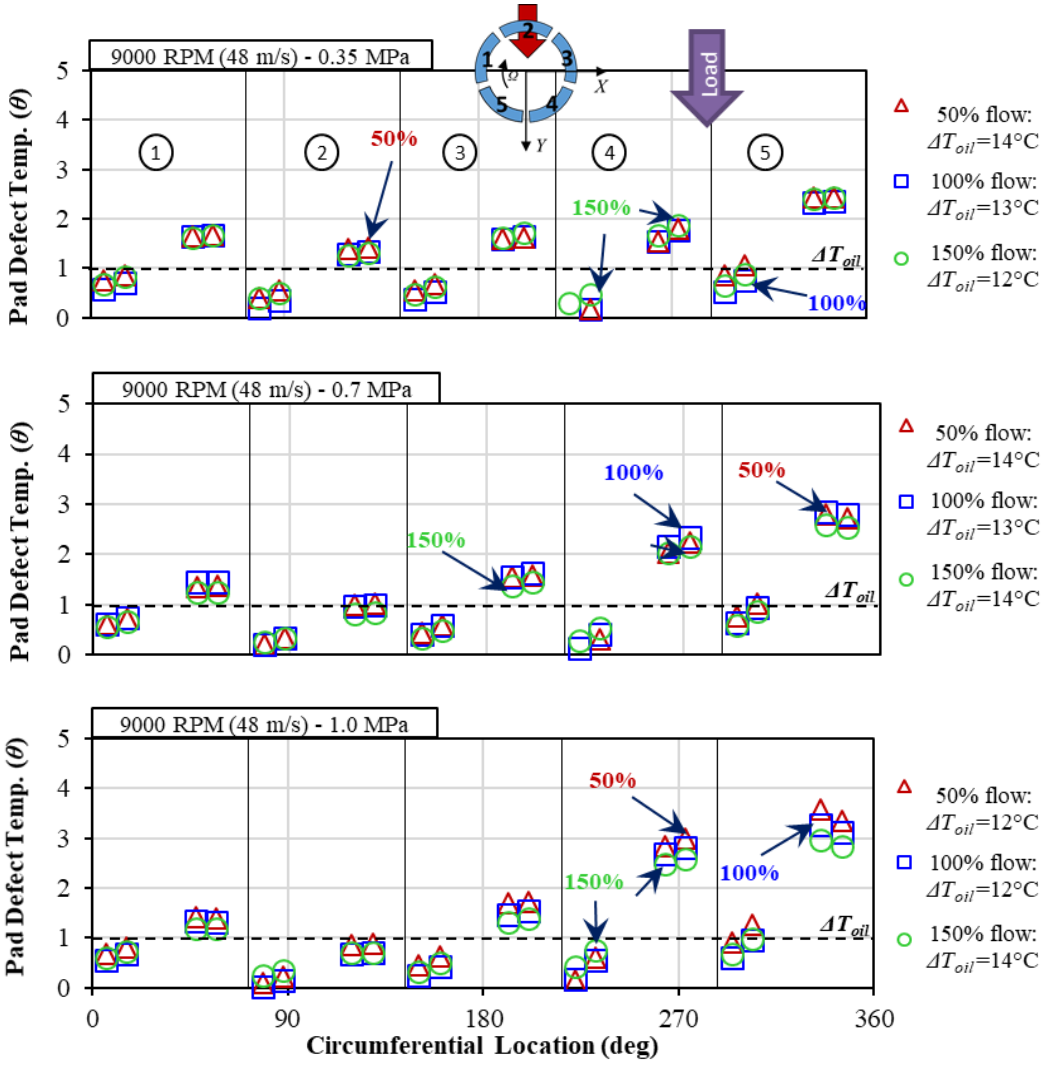

Figure 34. Measured pad defect temperature (*θ*) at 20 circumferential locations along mid-plane for operation at rotor speed (a) 9 krpm, (b) 12 krpm and (c) 14 krpm, under specific load (top) 0.35 MPa and (bottom) 1.0 MPa, and three oil flow rates (50%, 100% and 150%).

(b) 12 krpm

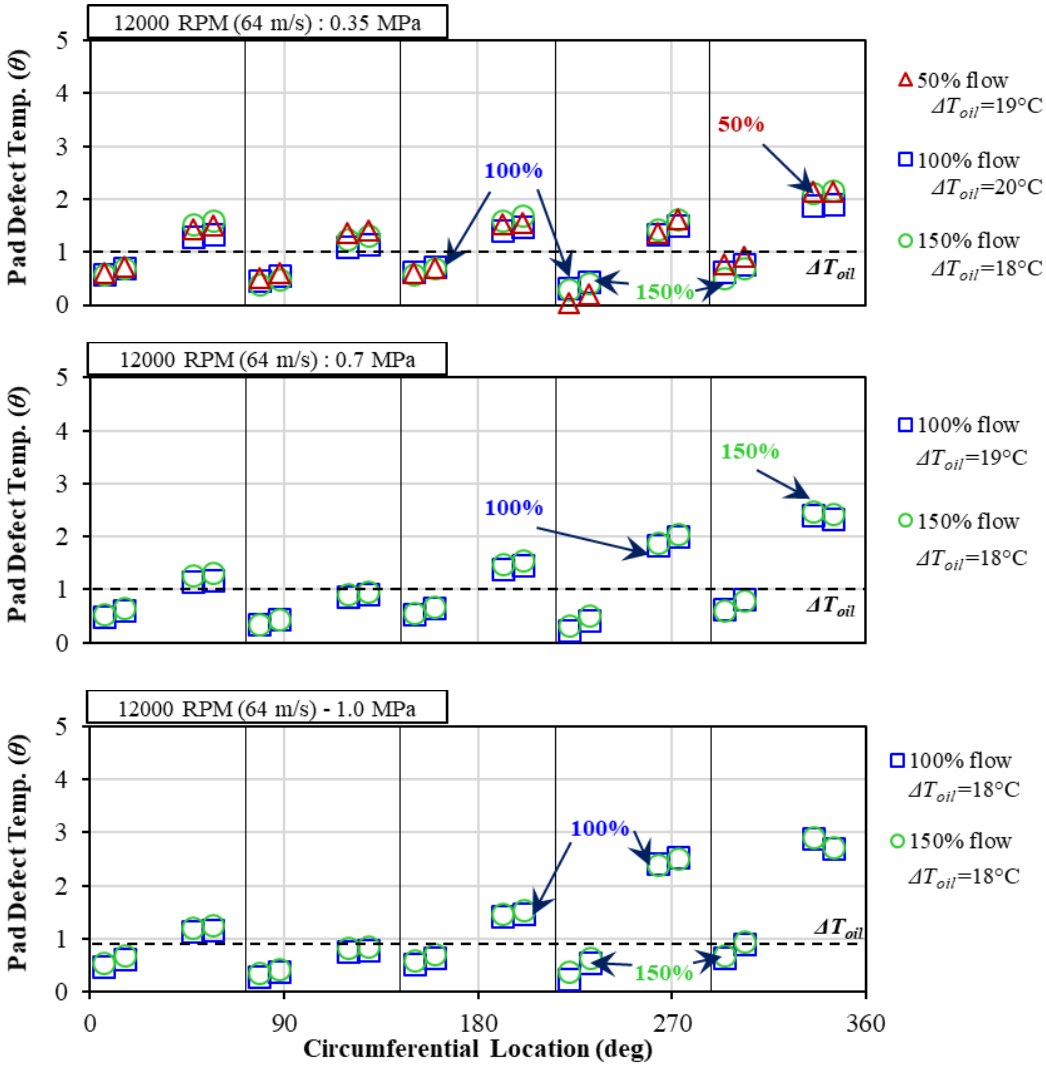

Figure 34 Continued.

(c) 14 krpm

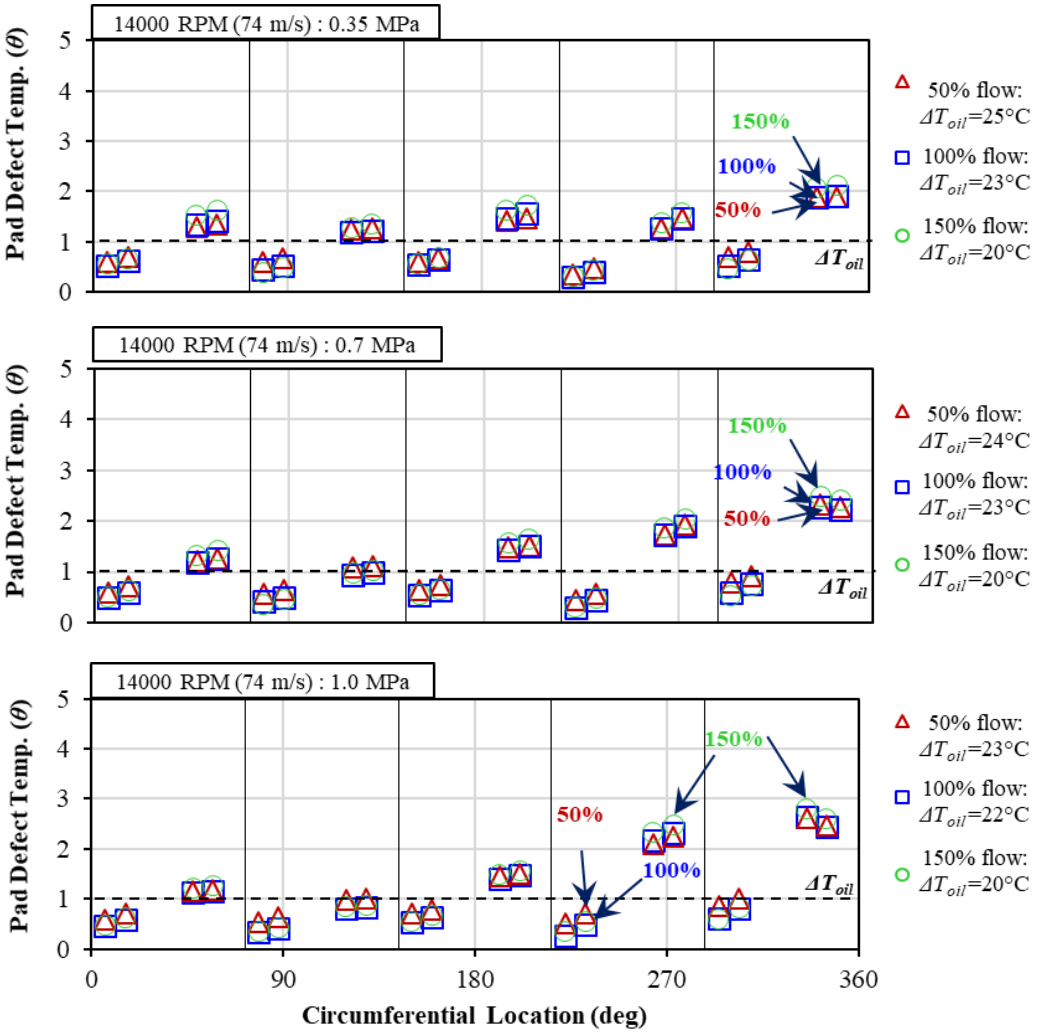

Figure 34 Continued.

Figure 35 depicts the pad defect temperature (θ) for operation at 12 krpm (64 m/s) shaft speed, three specific loads (0.35, 0.7 and 1.0 MPa), and two oil flow rates (27% and 50% of nominal). For 27% of nominal flow rate, θ_{max} increases from 2 to 3.5 on loaded pad #5, and from ≈ 1.2 to 3 on the unloaded pads #1, #2 and #3 as compared to those at nominal oil flow rate. Similar increase in θ_{max} is observed for the operation at 50% of nominal oil flow rate in the figure. Moreover, θ on the leading edge are severely impacted

on all five pads for 27% oil flow rate and thus measuring a maximum rise of 1.6 on pad #2. Please note, the supply oil temperature in the above operating conditions increases from 49°C to 59-62°C (ΔT_{oil} = 10-13°C) and thus the operation is outside normal test conditions.

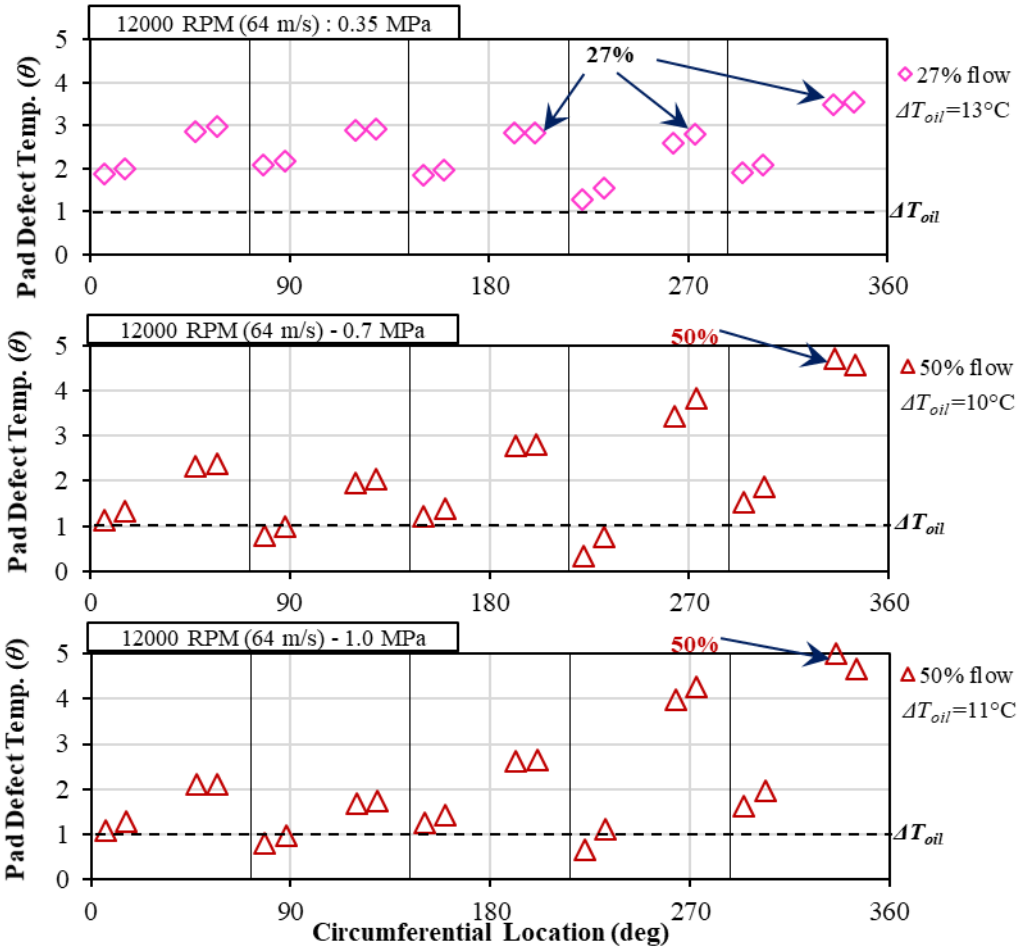

Figure 35. Measured pad defect temperature (θ) at 20 circumferential locations along mid-plane for operation at 12 krpm, under a specific load of (top to bottom) 0.35, 0.7 and 1.0 MPa and at 27% and 50% of nominal flow rate.

7.6 Closure

This chapter presents the measurements for the test bearing static force performance characteristics. These include oil temperature rise, shaft eccentricity, and attitude angle,

drag torque and power loss, and pad temperature rise. The oil temperature rise is a function of shaft surface speed and mostly independent of applied specific load. The shaft eccentricity is largely a function of both shaft surface speed and specific load. As expected in a TPJB, the attitude angle for most operating conditions is low.

The drag power loss and pad temperature are shown in a dimensionless form. The experimental drag power loss is obtained by two methods (1) a direct measurement of drag torque and shaft angular speed, and (2) an estimation based on oil flow rate and the oil temperature rise at the bearing exit plane.

A reduction in oil flow rate up to 50% of nominal magnitude causes a slight increase in the measured shaft eccentricity, pad temperature, and a decrease in measured drag power loss. In conclusion, for operation at a low flow rate (up to 50%), the bearing pad temperatures are not adversely affected while the drag power loss drops considerably, and thus provide significant energy savings. The test bearing operates safely (no significant pad temperature rise) even after reducing the oil flow rate by 50% and 73% of nominal flow for measurement at three rotor speeds. Moreover, an increase in supply oil flow rate causes a slight increase in drag power loss and an insignificant change in shaft eccentricity and pad temperatures.

The XLTPJB® model [12] delivers the prediction for the measured shaft eccentricity, attitude angle and pad temperatures. The model slightly under predicts the shaft eccentricity, over predicts the drag power loss and predicts well the maximum bearing pad temperature for the various test operating conditions.

8. DYNAMIC FORCE CHARACTERISTICS: TEST RESULTS AND DISCUSSION

This section discusses and presents the dynamic load performance of the test bearing measured at various operating conditions of static applied load, shaft rotational speed, and oil supply flow rate. The bearing dynamic properties include the four complex dynamic stiffnesses, and from them, twelve force coefficients (stiffness, damping, and virtual-mass).

8.1 Complex Dynamic Stiffness (*H*)

A multi-frequency dynamic force excitation and a frequency domain analysis, as explained in the parameter identification section, deliver the bearing complex dynamic stiffness (H), based on Eqs. 8-10, for a wide range of excitation frequencies (10-290 Hz). A frequency independent KCM model [Eq. (1)] fits the experimental complex dynamic stiffnesses to deliver four stiffness, four damping, and four virtual-mass coefficients. The real part of the complex dynamic stiffness delivers the stiffness and virtual-mass coefficients, $\mathrm{Re}(H) \rightarrow (K - M\omega^2)$; whereas the imaginary part delivers the damping coefficients, $\mathrm{Im}(H) \rightarrow (C\omega)$.

Figure 36 presents the experimental and predicted real and imaginary parts of the bearing (direct and cross-coupled) complex dynamic stiffnesses, $(H_{ij})_{i,j=x,y}$, versus excitation frequency (ω) for operation at 12 krpm (64 m/s), two specific loads (0.7 and 1.4 MPa) and 100% nominal flow. At both specific loads, the real part of (H_{xx}, H_{yy}) decreases with frequency (ω), which indicates a softening effect of the bearing. For operation at most rotor speeds (6 - 16 krpm) and at light loads (< 1.0 MPa), $\mathrm{Re}(H_{xx}) \approx \mathrm{Re}(H_{yy})$; whereas at high loads, $\mathrm{Re}(H_{yy}) > \mathrm{Re}(H_{xx})$. The real part of the bearing cross-coupled complex stiffnesses, $\mathrm{Re}(H_{xy}) \approx \mathrm{Re}(H_{yx})$, remains fairly constant, low in magnitude, both having negative signs for operation at rotor speed 6 - 16 krpm and under specific load 0.35 - 2.1 MPa.

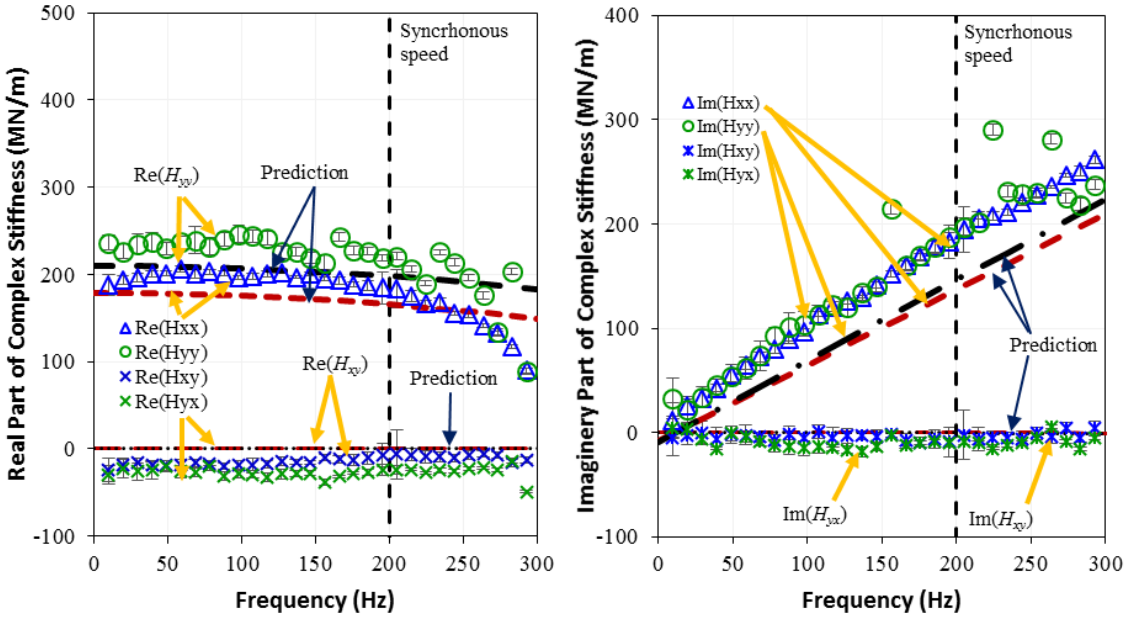

(a) Specific load: 0.7 MPa

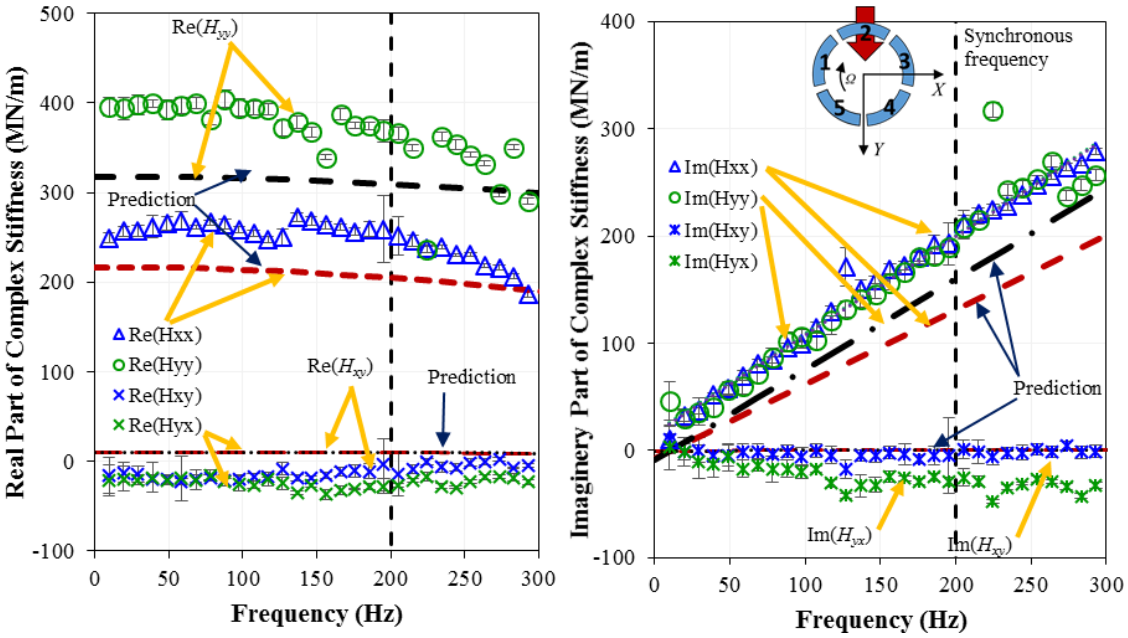

(b) Specific load: 1.4 MPa

Figure 36. Experimental and predicted real (left) and imaginary (right) parts of test bearing complex dynamic stiffnesses [$(H_{ij})_{i,j=x,y}$] for operation at 12 krpm (64 m/s), under specific load (a) 0.7 MPa and (b) 1.4 MPa, and 100% nominal flow.

The imaginary part of (H_{xx}, H_{yy}) increases linearly with frequency (ω) up to 290 Hz. The constant slope for Im(H_{xx}) and Im(H_{yy}) indicates constant damping coefficients (C_{xx}, C_{yy}). For operation at a rotor speed of 3 and 6 krpm, Im(H_{yy}) is slightly higher than Im(H_{xx}), whereas at rotor speed > 9 krpm, Im(H_{xx}) ≈ Im(H_{yy}). The cross-coupled Im(H_{xy}) and Im(H_{yx}) have a low magnitude (near zero), both having negative signs.

As mentioned earlier, the data at frequencies such as 60 Hz and its multiples, and shaft speed frequency (Ω) are neglected while fitting the KCM model as the associated uncertainties are high.

The error bars for the bearing complex dynamic stiffnesses (ΔH_{ij}), shown in Figure 36, and those for the force coefficients (discussed later in this section) represent 95% confidence intervals (2 x standard deviation) of the measured test data. Table 9 lists the measurement uncertainty (average of ΔH_{ij} over the entire ω) for the complex dynamic stiffness presented in Figure 36 over the entire excitation frequency range. APPENDIX A presents the measurement uncertainty calculations for the experimental direct complex dynamic stiffness and force coefficients.

For operation at 12 krpm (64 m/s) and under a 0.35 MPa specific load, the bearing complex dynamic stiffnesses (H) from the physical model XLTPJB® [12] and experimental procedure correlate well over the entire frequency range ω (10 - 290 Hz). However, the model under predicts Re(H_{yy}) by 20% and Re(H_{xx}) by 15% for $\omega < \Omega$ at 12 krpm and under a 1.0 MPa specific load. For the same case, the model under predicts the imaginary part of H. Note Im(H_{yy}) > Im(H_{xx}) whereas the experimental Im(H_{yy}) ≈ Im(H_{xx})

Table 9. Average measurement (%) uncertainty of the complex dynamic stiffness (H_{ij}) obtained at 12 krpm and under a specific load of 0.7 and 1.4 MPa.

Average measurement uncertainty over entire ω range (% of H_{ij})				
Specific Load (MPa)	Re(ΔH_{xx})	Re(ΔH_{yy})	Im(ΔH_{xx})	Im(ΔH_{yy})
0.7	5	6	4	5
1.4	6	6	5	7

The following sections present the force coefficients, namely K, C and M in a dimensionless form. Let k, c and m be

$$k_{ij}=\frac{K_{ij}\,C_r}{W},\ c_{ij}=\frac{C_{ij}\,\Omega\,C_r}{W},\ m_{ij}=\frac{M_{ij}\,\Omega^2\,C_r}{W};\ [i,j=x,y] \tag{23}$$

where K_{ij} is a stiffness coefficient, C_{ij} is a damping coefficient and M_{ij} is a virtual-mass coefficient (kg). Above C_r is the *cold* bearing radial clearance (C_r = 62.5μm), W is the applied static load on the bearing, and Ω is the shaft rotational speed (rad/s).

8.2 Direct Stiffness Coefficients

Figure 37 presents the experimental direct stiffnesses (k_{xx}, k_{yy}) of the test bearing along the horizontal (x- unloaded) and vertical (y- loaded) directions, respectively, as a function of shaft surface speed. The test conditions include operation at six surface speeds (16 to 85 m/s), five specific loads (0.7 to 2.1 MPa), and at 100% nominal flow rate.

Both direct stiffnesses (k_{xx}, k_{yy}) increase with an increase in rotor speed and decrease with an increase in applied specific load. For example, at a specific load of 1.0 MPa, k_{xx} increases by 95%, whereas k_{yy} increases by 30% with an increase in surface speed from 16 to 85 m/s. Overall, the uncertainty for the direct stiffness coefficients ranges from 1% to 5% of the actual magnitude indicating a good precision of the measurements.

Please note the dimensionless coefficients (k_{xx}, k_{yy}) do not represent actual physical trends. For example, with an increase in applied specific load from 0.7 to 2.1 MPa at a surface speed 48 m/s, k_{xx} decreases by 50% and k_{yy} decreases by 30%; whereas the actual K_{xx} increases by 50%, and K_{yy} increases by 110%. The ratio (W/C_r) is higher for operation at a high specific load which results in smaller k's as compared to the actual physical coefficient (K).

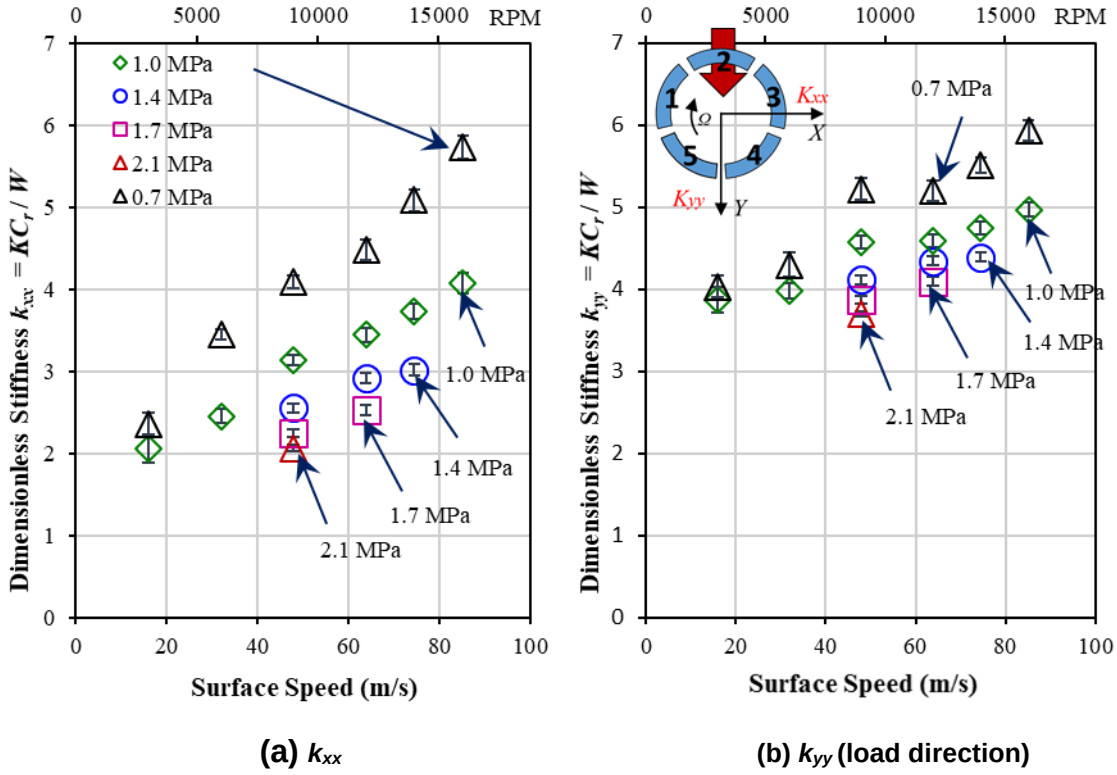

(a) k_{xx} **(b) k_{yy} (load direction)**

Figure 37. Bearing experimental dimensionless direct stiffness coefficients (a) k_{xx} and (b) k_{yy} vs. surface speed (16 to 85 m/s) for operation at five specific loads (0.7 to 2.1 MPa) and 100% nominal flow rate.

Figure 38 presents the experimental and predicted k's as a function of the Sommerfeld number (S) at various test conditions. The direct k_{xx} and k_{yy} increase; whereas k_{xy} and k_{yx} remain constant (null) with an increase in S. For $S < 2$, $k_{xx} < k_{yy}$; whereas for $S > 2$, $k_{xx} \approx k_{yy}$. The model predictions correlate well with k_{xx} and k_{yy} for $S < 4$, and under predict by up to 27% at $S \approx 4.6$.

The bearing direct stiffnesses (k_{xx} and k_{yy}) are symmetric for a typical TPJB under a LBP orientation, in particular at a light load. Refs. [24, 26] also report isotropic stiffness coefficients for lightly loaded (< 0.7 MPa) bearings under a LBP orientation. Figure 39 presents a comparison of the direct stiffnesses k_{xx} vs. k_{yy} at various rotor speeds and specific loads. As a specific load increases from 0.7 to 2.1 MPa, the stiffness orthotropy increases ($k_{yy} > k_{xx}$) and the test result moves away from the symmetry line (45°) as shown

in the figure. Conversely, with an increase in rotor speed under a constant specific load, the direct stiffnesses move slightly closer to the symmetry line. For operation at 9 krpm (48 m/s) and 2.1 MPa specific load, k_{xx} is almost half (≈ 55%) of k_{yy}, thus showcasing a significant amount of stiffness orthotropy.

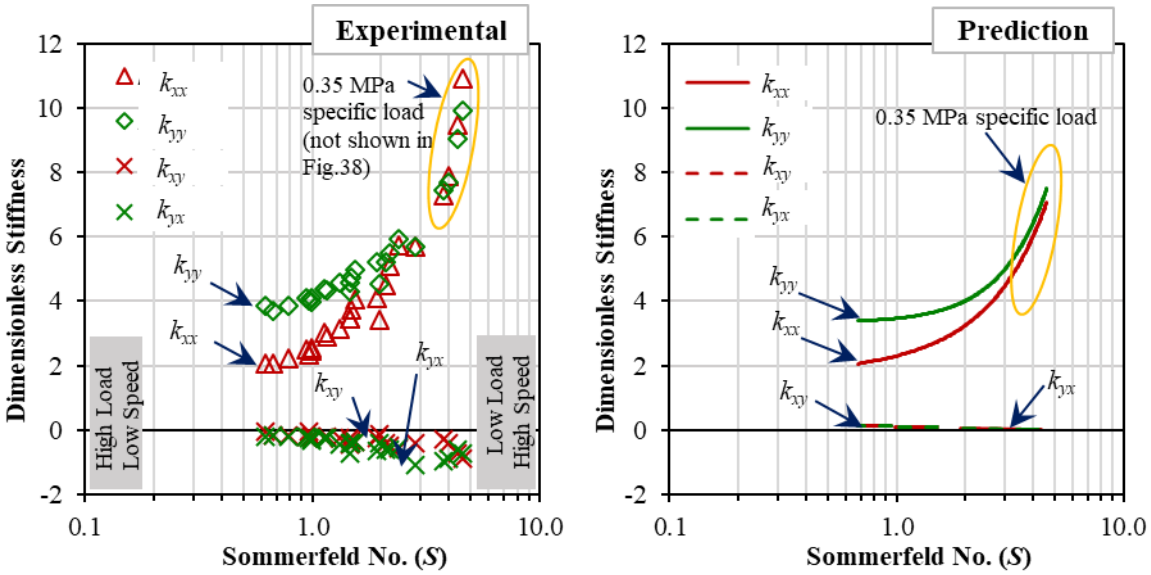

(a) Experimental (b) Prediction

Figure 38. Bearing (a) experimental and (b) predicted dimensionless stiffnesses (k_{xx}, k_{yy}) vs. Sommerfeld number (S) for operation at various shaft surface speed 16-65 m/s and specific load 0.35-2.1 MPa.

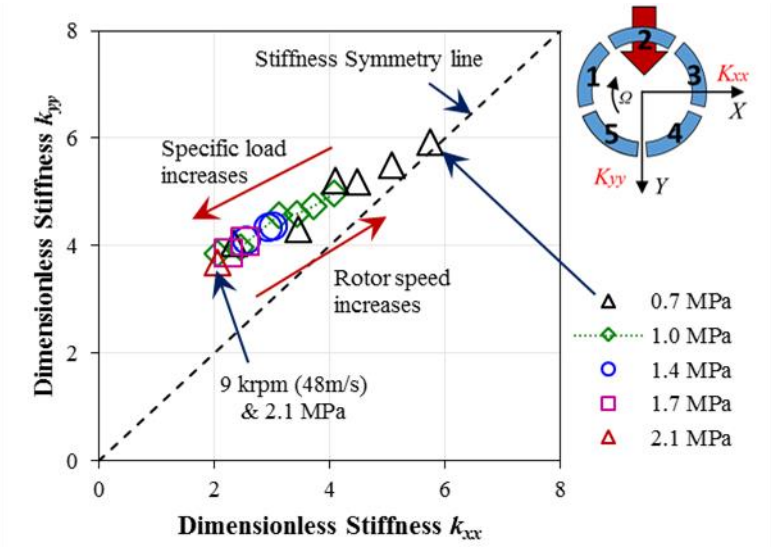

Figure 39. Bearing dimensionless stiffnesses k_{xx} vs. k_{yy} as a function of increasing surface speed (16 to 85 m/s) and specific load (0.7 to 2.1 MPa) for operation at 100% nominal flow.

Figure 40 depicts a comparison of k_{xx} and k_{yy} for operation with the test bearing supplied with oil flow rate at 27%, 50%, 100% and 150% of nominal flow. The test conditions include operation at a surface speed equal to 48, 64 and 74 m/s (9, 12 and 14 krpm), and under a specific load equal to 0.35, 0.7 and 1.0 MPa. Typically for operation at 50% of nominal flow, the measured shaft eccentricity is slightly higher compared to that at 100% and 150% of nominal flow, and thus indicates the direct stiffness should increase with a reduction in oil flow rate. For operation at 9 krpm (48 m/s) and under 1.0 MPa specific load, (k_{xx}, k_{yy}) are higher by ≈ 5% and ≈ 10% for 50% of nominal flow as compared to those for 100% and 150% of nominal flow, respectively. Mostly, with a reduction in flow rate from 100% to 50%, k_{xx} and k_{yy} either slightly increase or remain invariant. Moreover, with an increase in oil flow (150% of nominal flow), k_{xx} and k_{yy} reduce by 1% to 5% or change insignificantly.

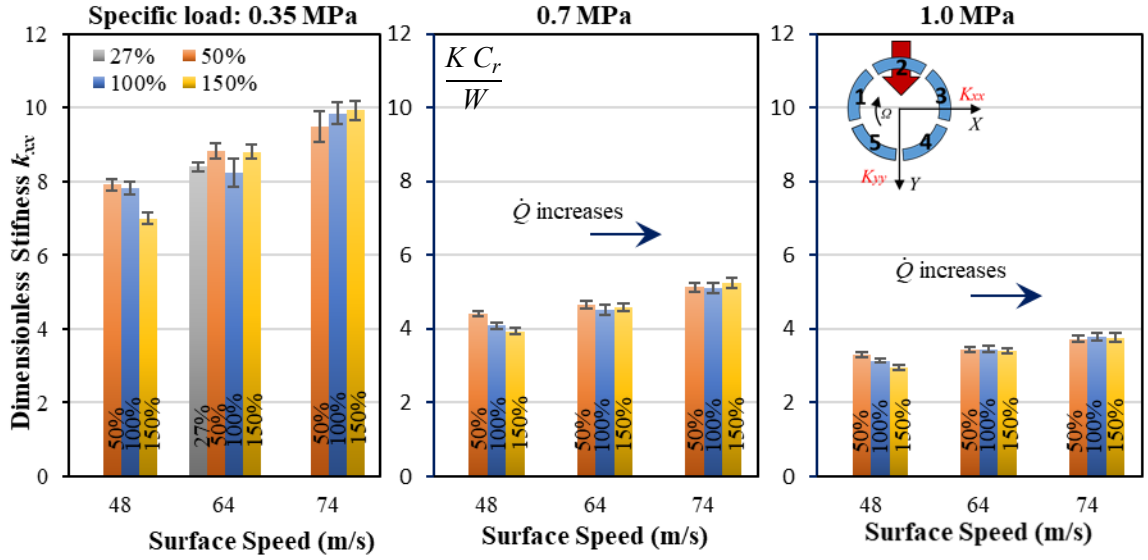

(a) k_{xx}

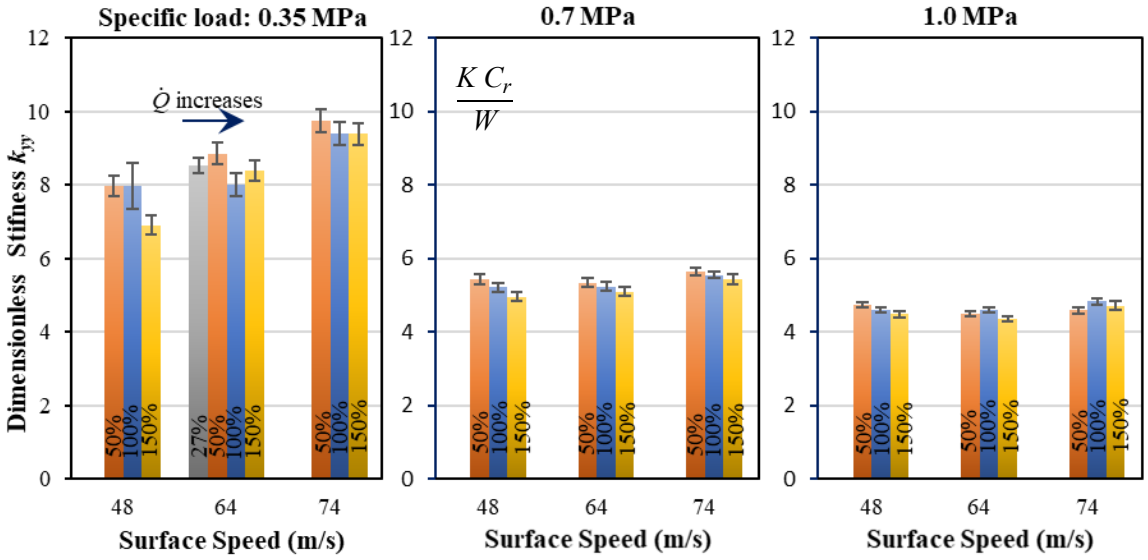

(b) k_{yy} (load direction)

Figure 40. Bearing dimensionless stiffnesses (a) k_{xx} and (b) k_{yy} vs. shaft surface speed (m/s) for operation under specific load (left to right) 0.35 MPa, 0.7 MPa and 1.0 MPa, and at four oil flow rates (27%, 50%, 100%, and 150%).

8.3 Cross-coupled Stiffness Coefficients

Figure 41 presents the experimental cross-coupled stiffness coefficients (k_{xy} and k_{yx}) versus surface speed for operation at five specific loads (0.7 to 2.1 MPa) and 100% nominal flow. k_{xy} and k_{yx} have low magnitudes (< 0.7), both have negative signs and typically $k_{yx} > k_{xy}$ for the set operating conditions. The uncertainty for k_{xy} and k_{yx} range from 6% to 30% of the actual magnitude for the test operating range. Contrary to results in this study, Refs. [21, 26] report opposite signs for the cross-coupled stiffnesses at certain operating conditions. The opposite signs for both k_{xy} and k_{yx} add energy to forward whirling motion and can cause instability to the R-B system [1].

Both k_{xy} and k_{yx} change insignificantly with a variation in the oil supply flow rates (27%-150% of nominal flow). Overall, both the coefficients have same (negative) signs and low magnitudes at most test conditions similar to those for nominal oil flow.

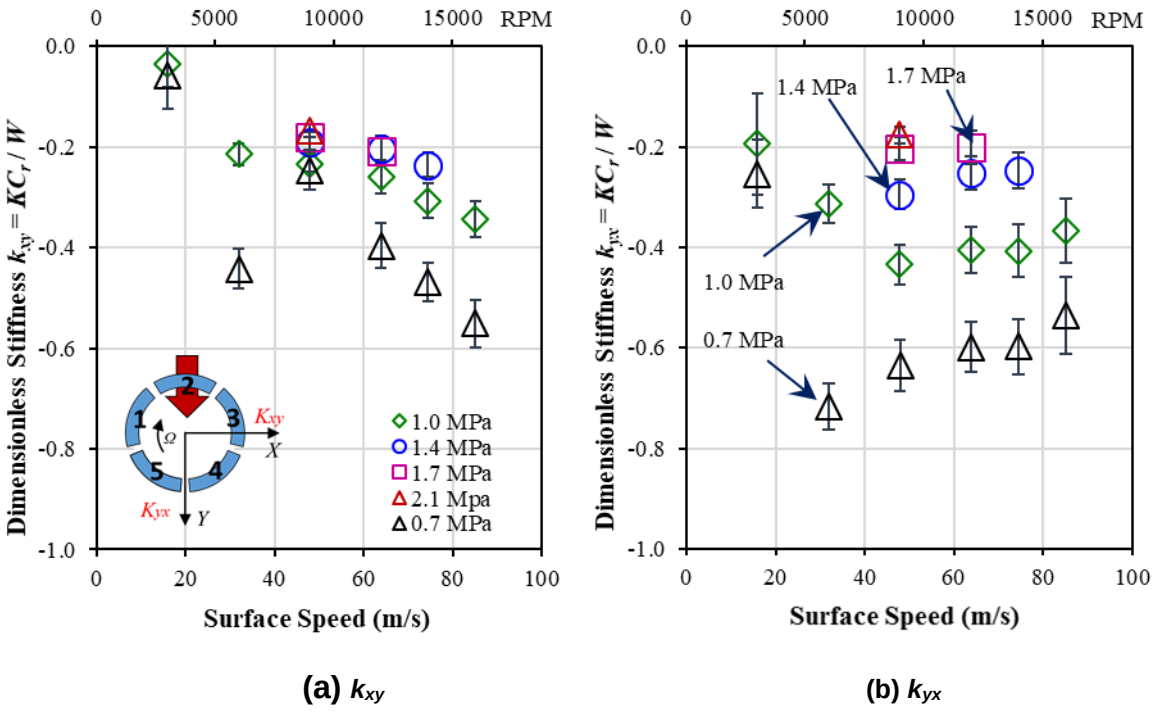

Figure 41. Bearing cross-coupled stiffnesses (a) k_{xy} and (b) k_{yx} vs. shaft surface speed (m/s) for operation at five specific loads (0.7 to 2.1 MPa) and 100% nominal flow rate.

8.4 Damping Coefficients

Figure 42 presents the experimental dimensionless direct damping coefficients (c_{xx}, c_{yy}) versus shaft surface speed for operation under five specific loads (0.7-2.1 MPa) and at 100% nominal flow. c_{xx} and c_{yy} increase proportionally with shaft surface speed and decrease with an increase in specific load. For example, under a 1.0 MPa specific load, c_{xx} and c_{yy} increase by 290% and 190%, respectively, with an increase in shaft surface speed from 16 to 85 m/s (3-16 krpm). A similar increasing trend for damping coefficients is observed at light (< 0.7 MPa) and heavy (> 1 MPa) specific loads. Overall, the measurement uncertainty for direct damping coefficients ranges from 3% to 18% of the actual magnitude.

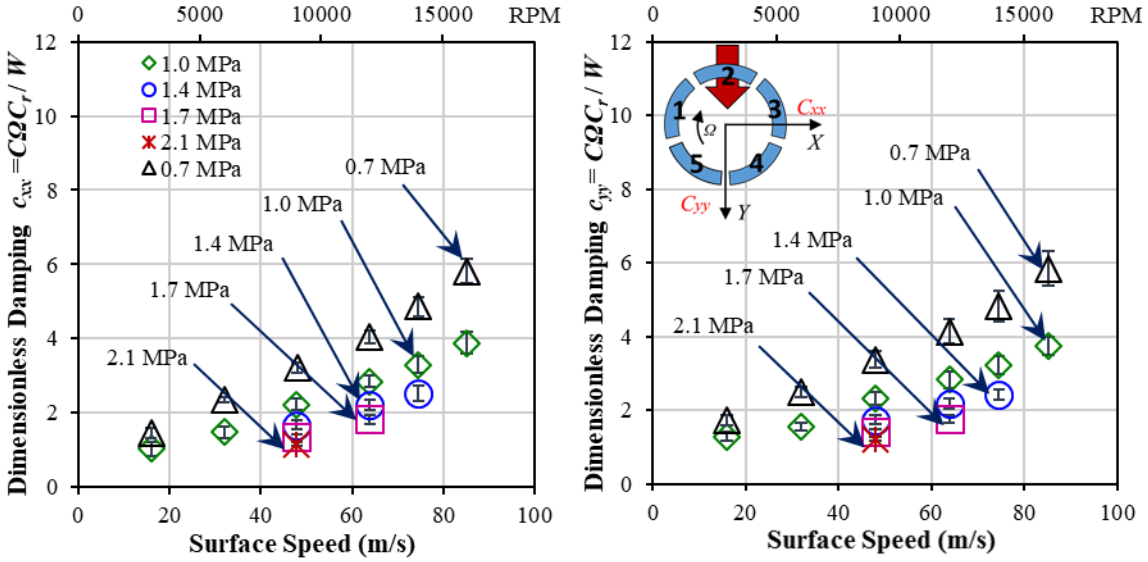

(a) c_{xx} **(b) c_{yy} (load direction)**

Figure 42. Bearing dimensionless damping (a) c_{xx} and (b) c_{yy} vs. shaft surface speed (m/s) for operation at five specific loads (0.7 to 2.1 MPa) and at 100% nominal flow.

Figure 43 presents the experimental and predicted (c_{xx}, c_{yy}) as a function of the Sommerfeld number (S) at various test conditions. The direct damping coefficients (c_{xx}, c_{yy}) increase with an increase in S; and both coefficients remain symmetric ($c_{xx} \approx c_{yy}$) over

the entire S range. The model predicts damping coefficients that correlate well for $S < 3$ and under predicts for $S > 3$ compared to the experimental (c_{xx}, c_{yy}).

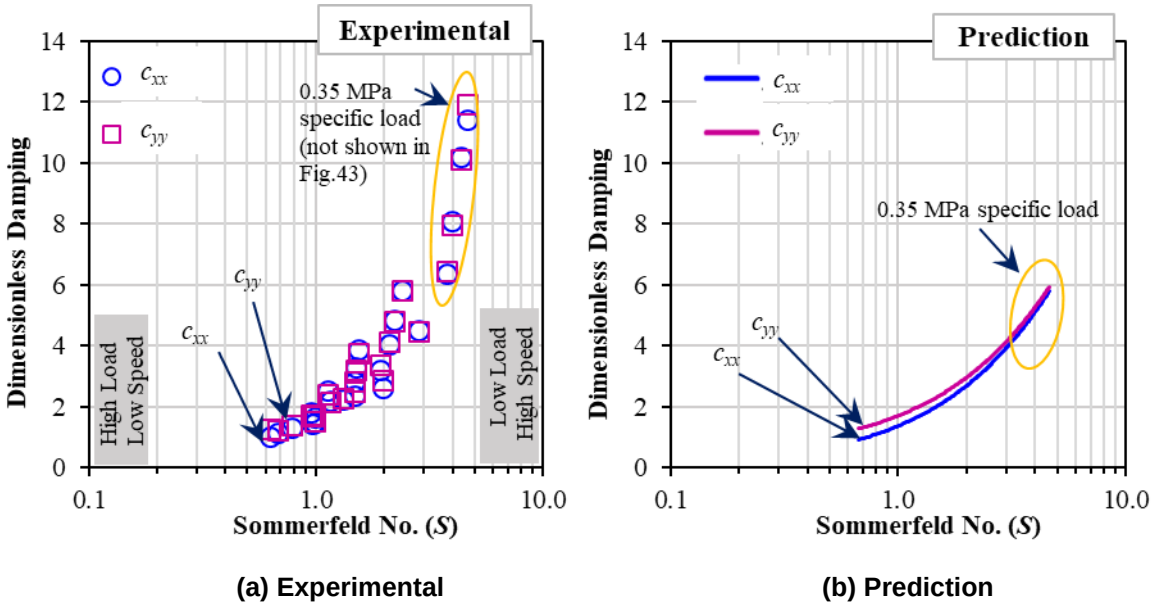

Figure 43. (a) Experimental and (b) predicted dimensionless damping coefficients (c_{xx}, c_{yy}) vs. Sommerfeld number (S) for operation at various shaft surface speed 32-65 m/s and specific load 0.35-2.1 MPa.

Figure 44 presents a comparison of c_{xx} and c_{yy} for operation with the bearing supplied with oil flow rate at 27%. 50%, 100% and 150% of nominal flow. The test conditions include operation at a surface speed of 48, 64 and 74 m/s (9, 12 and 14 krpm), and under a specific load of 0.35, 0.7 and 1.0 MPa. For 50% of nominal flow rate, c_{xx} and c_{yy} reduce by 7% (max.) compared to those with 100% nominal flow. However, c_{xx} and c_{yy} reduce by 16% for operation with 27% of nominal flow. Moreover, for an operation with 150% of nominal flow, c_{xx} and c_{yy} increase by ≈ 5% at surface speed 74 m/s and remain fairly constant or change insignificantly at other speeds (48 and 64 m/s) compared to those with nominal flow rate.

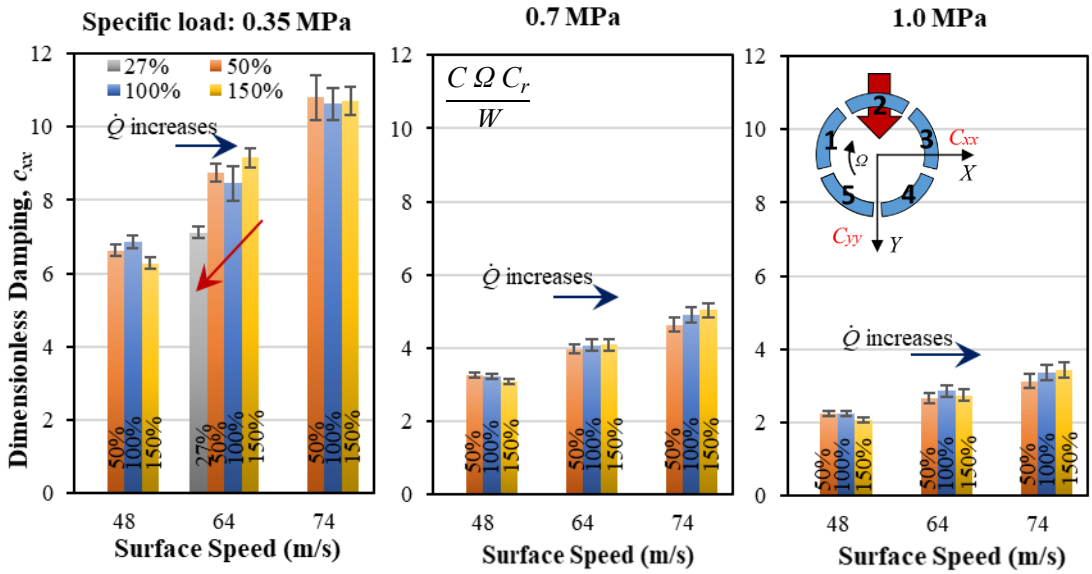

(a) c_{xx}

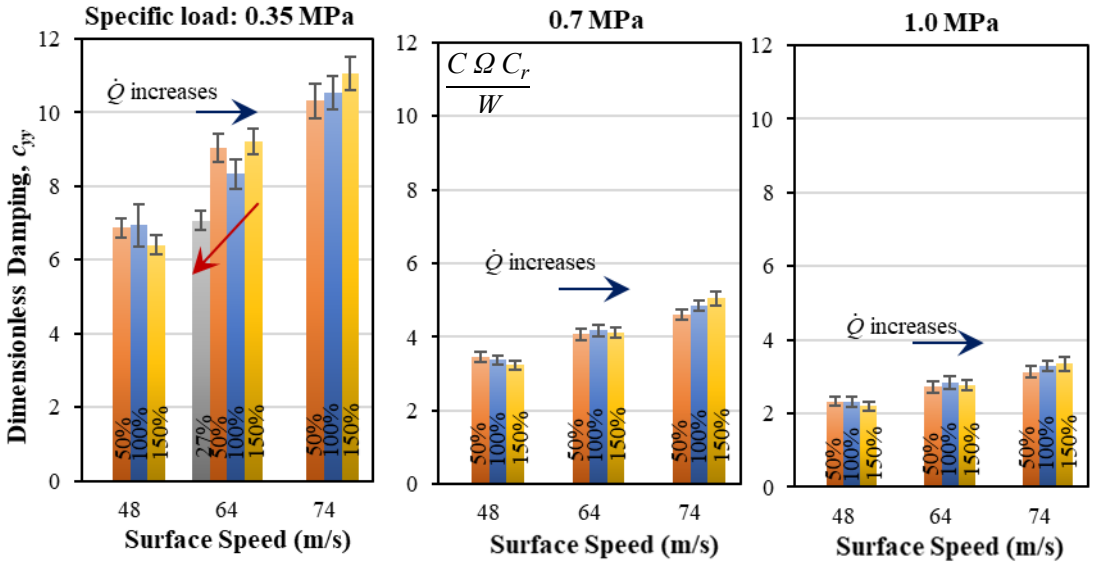

(b) c_{yy} (load direction)

Figure 44. Bearing experimental damping (a) c_{xx} and (b) c_{yy} vs. rotor speed for operation under specific load (left to right) of 0.35 MPa, 0.7 MPa and 1.0 MPa, and at four oil flow rates (27%, 50%, 100%, and 150%).

The cross-coupled damping coefficients (c_{xy} and c_{yx}) have negative signs, and both are low in magnitude. The measurement uncertainty for c_{xy} and c_{yx} is high, ranging from 30% to 100% of the actual magnitude.

8.5 Direct Virtual-Mass Coefficients

Figure 45 presents the experimental dimensionless virtual-mass coefficients (m_{xx}, m_{yy}) versus shaft surface speed for operation under six specific loads (0.7 to 2.1 MPa) and at 100% nominal flow rate. The virtual-mass coefficient in the KCM model captures the curvature of the real part of the complex dynamic stiffness (H). m_{xx} ranges from 0.1 to 0.9 and m_{yy} ranges from 0.2 to 0.5[13] for the entire operating range. Both m_{xx} and m_{yy} have a dependency on the applied specific load and rotor speed. Moreover, m_{xx} has a greater dependency on specific load as compared to m_{yy}. For example, at 48 m/s, m_{xx} and m_{yy} decrease by 65% and 35%, respectively, with an increase of specific load from 0.7 MPa to 2.1 MPa. Moreover, with an increase of shaft surface speed from 32 m/s to 85 m/s, m_{xx} and m_{yy} increase by 350% and 135%, respectively, under 1.0 MPa specific load.

The measurement uncertainty for m_{xx} and m_{yy} are quite large for operation under a light load and high shaft surface speed. Overall, the measurement uncertainties for m_{xx} and m_{yy} range from 10% to 50% of the direct coefficient magnitude.

[13] The added mass coefficient [36] from equation $M_{xx}=\rho\,\pi\left(\frac{D}{2}\right)^3\frac{L}{c}\left(1-\frac{\tan\left(\frac{L}{D}\right)}{\left(\frac{L}{D}\right)}\right)$ for open ends squeeze-film damper delivers around ≈ 13 kg which is close to the physical virtual-mass coefficients for most test conditions.

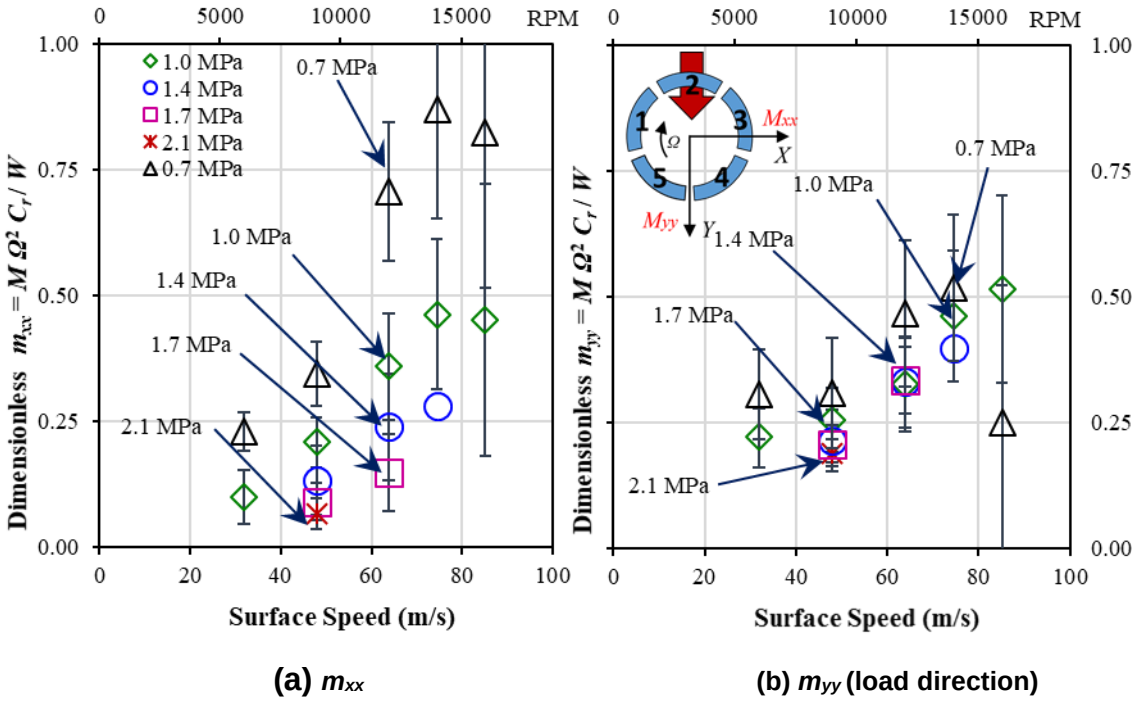

(a) m_{xx} **(b) m_{yy} (load direction)**

Figure 45. Bearing dimensionless virtual-masses (a) m_{xx} and (b) m_{yy} vs. shaft surface speed (m/s) for operation at five specific loads (0.7 to 2.1 MPa) and 100% nominal flow rate.

Figure 46 presents the experimental and predicted (m_{xx}, m_{yy}) as a function of the Sommerfeld number (S) at various test conditions. The direct virtual-mass coefficients (m_{xx}, m_{yy}) increase from 0 to 2.7 with an increase in S from 0.6 to 4.6. Please note, the model predicts negative virtual-mass coefficients, unlike measured results, for all S and ranges from 0 to -1 with an increase in S.

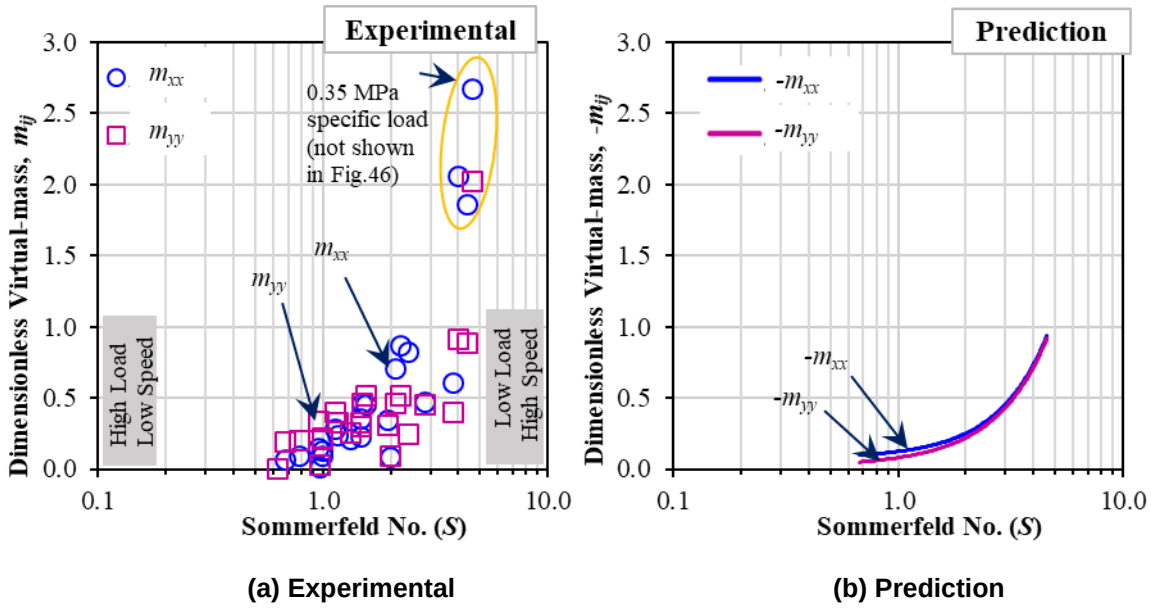

Figure 46. (a) Experimental and (b) predicted dimensionless virtual-mass coefficients (m_{xx}, m_{yy}) vs. Sommerfeld number (*S*) for operation at various shaft surface speed 32-65 m/s and specific load 0.35-2.1 MPa.

Figure 47 depicts a comparison of m_{xx} and m_{yy} for operation with the bearing supplied at four oil flow rates (27% - 150%). The test conditions include operation at a surface speed of 48, 64 and 74 m/s (9, 12 and 14 krpm), and under a specific load of 0.35, 0.7 and 1.0 MPa. Upon varying oil flow rate from 50% to 150% of nominal, m_{xx} and m_{yy} change negligibly under 1.0 MPa specific load. However, for operation at different oil flow rate (27% to 150%), both m_{xx} and m_{yy} change insignificantly or erratically under a light specific load of 0.35 MPa and 0.7 MPa and at three surface speeds (48, 64, 74 m/s).

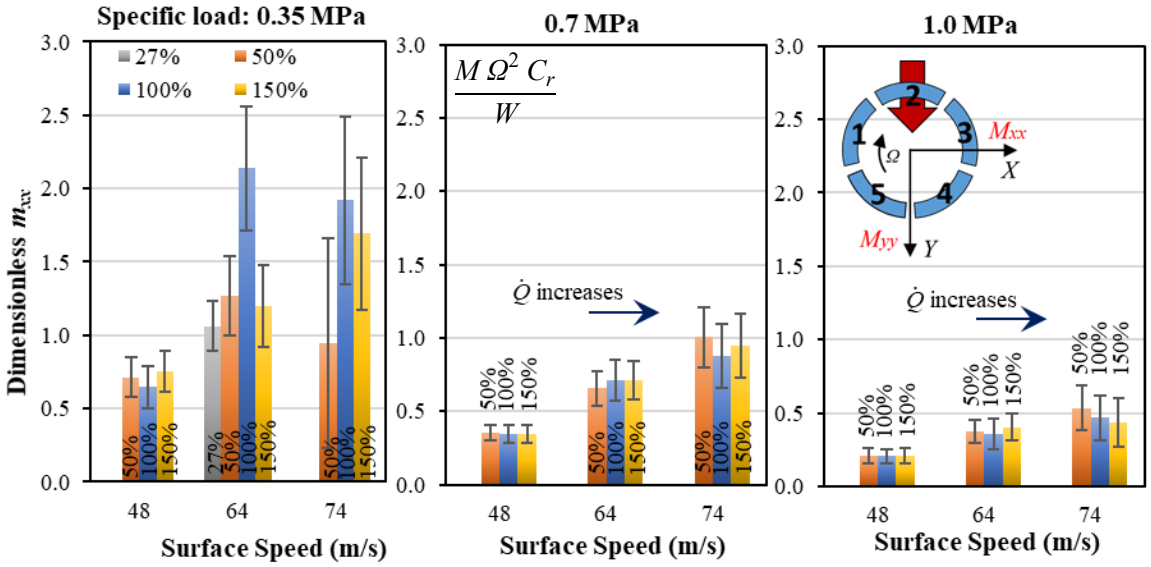

(a) m_{xx}

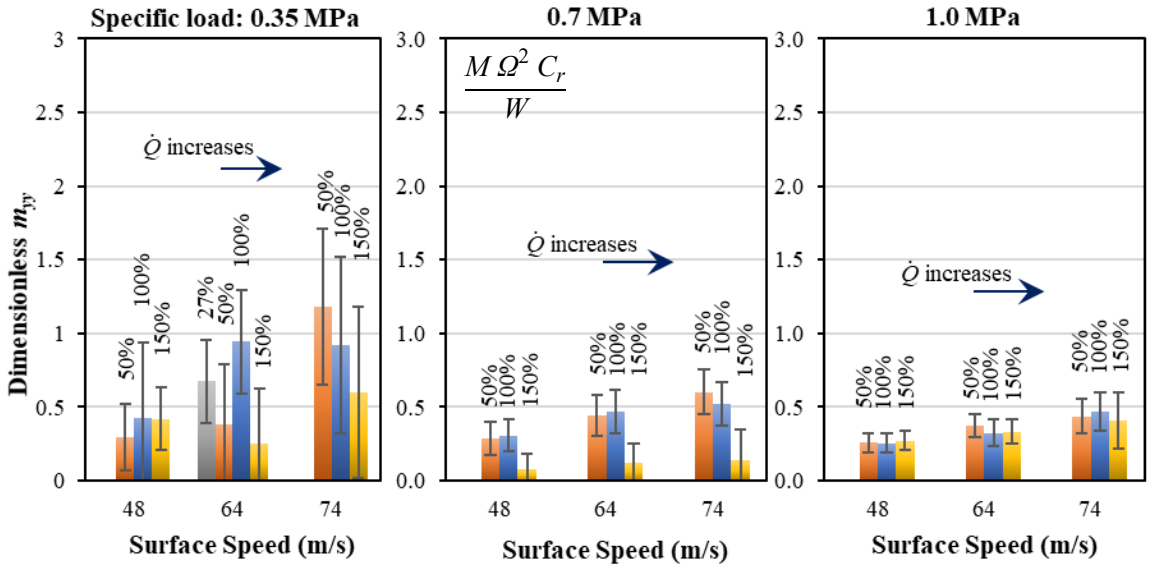

(b) m_{yy}

Figure 47. Bearing experimental dimensionless virtual-masses (a) m_{xx} and (b) m_{yy} vs. surface speed (m/s) for operation under specific load (left to right) 0.35 MPa, 0.7 MPa and 1.0 MPa, and at four different oil flow rates (27%, 50%, 100%, and 150%).

8.6 Closure

This section presents and discusses the complex dynamic stiffnesses of the test bearing obtained experimentally over an excitation frequency range from 10 Hz to 290 Hz. The stiffness, damping, and virtual-mass coefficients are shown in dimensionless form vs. shaft surface speed, applied load and the Sommerfeld number (S).

The dimensionless direct stiffness, damping and virtual-mass coefficient increase with an increase in shaft speed and a decrease in applied load (i.e. an increase of the Sommerfeld number). The stiffness coefficients, horizontal and vertical (load direction), are symmetric at a light specific load, however, both coefficients become asymmetric for W/(LD) above 0.7 MPa. The direct damping coefficients are symmetric ($c_{xx} \approx c_{yy}$) for most operating cases. As expected in a TPJB, the cross-coupled stiffness coefficients are negligible.

The XLTPJB® model [12] predicts well the stiffness and damping coefficients for low Sommerfeld number (< 2) and slightly under predicts both the stiffness and damping at high Sommerfeld number (> 2). The model delivers negative virtual-mass coefficients and hence significantly under predicts as compared to the test data.

For operation with a reduction in oil flow rate from 100% to 27% of nominal, both the dimensionless and physical direct stiffness coefficients slightly increase, the damping coefficients decrease and the virtual-mass coefficients change insignificantly. An increase in the physical bearing stiffness coefficient with a reduction in the supplied oil flow rate alters the critical speed of the R-B system, while a decrease in the bearing direct damping coefficient (dimensional) affects the bearing speed-synchronous vibration amplitude when a machine crosses a critical speed. On the contrary, for operation with an increased oil flow rate from 100% to 150% of nominal, the stiffness coefficients slightly decrease or change insignificantly, the damping coefficients increase and the virtual-mass coefficients change insignificantly.

9. SUMMARY AND CONCLUSION

This thesis presents the measurement of the static and dynamic forced characteristics on a five-pad spherical pivot tilting-pad journal bearing (TPJB) with an end seals under LBP orientation. Additionally, this study also discusses the influence of varying the supply oil flow rate to the test bearing during its operation.

The summary of major findings derived from the tests at steady-state are:

1. The measured bearing clearance becomes smaller at an elevated shaft and bearing temperatures. With an increase in rotor speed, the operating temperature becomes higher because of shear drag, and thus causes a smaller bearing clearance. The *cold* bearing diametrical clearance at 25°C is 125 μm, whereas the *hot* bearing clearance at 65°C and measured after the operation at 16 krpm is just 105 μm, i.e. a 16% reduction.
2. The journal eccentricity (e) is largely a function of rotor speed and applied specific load. The eccentricity increases slightly both at a reduced oil flow rate (50%) and increased flow rate (150%) compared to those for 100% oil flow rate. The attitude angle at most operating conditions is less than 10° which evidences low cross-coupled stiffnesses in the bearing.
3. The discharge oil temperature rise is a function of rotor speed and nearly independent of an applied load. The maximum discharge temperature rise is 26°C for operation at 16 krpm and under 1.0 MPa specific load. Oil flow variations (50-150%) have a slight impact on the discharge oil temperature (< 5°C).
4. Both the dimensionless drag power loss ($\overline{P}$), i.e. based on direct torque measurement and estimation based on the oil flow rate and temperature rise, increase with an increase in rotor speed, whereas they change negligibly with an increase in applied specific load. The direct drag power loss is lower by ≈ 20% as compared to the estimated drag power loss for most operating conditions. For operation at 50% of nominal oil flow rate, the direct drag power loss slightly

decreases as compared to that at 100% nominal flow rate for rotor speed up to 8 krpm (42 m/s) and vice versa at 150% of nominal flow rate. Interestingly, the measured drag power loss is less dependent on the supplied oil flow rate as compared to the estimated drag power loss.

5. Six thermocouples on each pad measure the pad metal sub-surface temperature and thus cover the entire periphery (circumferential and axial) of the test bearing. The maximum pad defect temperature (θ), relates ΔT_{pad} to ΔT_{oil}, is mostly measured on pad #5 (loaded) at 75% pad arc-length. θ is largely a function of both rotor speed and applied load. For Sommerfeld number $S < 1$, $\theta \approx 4$ and for $S > 2$, $\theta \approx 2$, i.e. twice the exit ΔT_{oil}. For operation at 50% of nominal oil flow rate, θ slightly varies by ≈ 0.3 while the physical pad temperature-rise increases by ≈ 5°C for various operating condition as compared to that at 100% oil flow rate. Conversely, an increase in oil flow rate to 150% of nominal flow rate causes a slight reduction in θ up to ≈ 0.3 and the physical pad temperature up to ≈ 2°C.

The summary of major findings derived from the tests under dynamic load are:

1. The dimensionless direct stiffness coefficients (k_{xx}, k_{yy}) increase with an increase in rotor speed and decrease with an increase in specific load. The physical direct stiffness coefficients (K_{xx}, K_{yy}) increase with an increase in the rotor speed and an applied specific load. On reducing the oil flow rate to 50% of nominal, (k_{xx}, k_{yy}) slightly increase and vice-versa.
2. Both the physical and dimensionless cross-coupled stiffness coefficients (k_{xy}, k_{yx}) are low in magnitude; both having a negative (same) sign. Moreover, both the cross-coupled coefficients change insignificantly for operation with a changing oil flow rate (27% to 150% of nominal).
3. The dimensionless direct damping coefficients (c_{xx}, c_{yy}) increase with an increase in rotor speed and decrease with an increase in specific load. The physical direct damping coefficients (C_{xx}, C_{yy}) slightly decrease with an increase in the rotor speed, whereas they change insignificantly with an increase in an applied specific

load. The damping coefficients are flow dependent and decrease up to 16% (max.) for operation with reduced oil flow rate (up to 27% of nominal) when compared to those at 100% nominal flow rate.

4. The virtual-mass coefficients (m_{xx}, m_{yy}) have positive magnitude. Both the coefficients are significantly dependent on rotor speed and slightly dependent on specific load. The physical direct virtual-mass coefficients (M_{xx}, M_{yy}) change erratically or negligible with an increase in the rotor speed and an applied specific load.

The summary of the comparison between the measurements and predictions from XLTPJB® model are:

1. The XLTPJB® [12] model slightly under predicts the shaft eccentricity, over predicts the drag power loss and predicts well the maximum bearing pad temperatures for most operating conditions.
2. The model predicts well the stiffness and damping coefficients for low Sommerfeld number (< 2) and slightly under predicts both the stiffness and damping at high Sommerfeld number (> 2). The model delivers negative virtual-mass coefficients and hence significantly under predicts as compared to the test data.

Based on this thesis, it is understood that reducing the supplied oil flow rate (by 50%) in the sealed TPJB has only a slight impact on its steady-state and dynamic force performance. For future recommendation, tests similar to this study on a TPJB with direct lubrication and an evacuated housing could provide further insight into its performance change due to supply oil flow rate variation.

REFERENCES

[1] Zeidan, F. Y., and Herbage, B. S., 1991, "Fluid Film Bearing Fundamentals and Failure Analysis - Tutorial," Proc. 20th Turbomachinery Symposium, The Turbomachinery Laboratory, Texas A&M University, September 17-19, Dallas, TX, USA, pp. 145-154.

[2] Childs, D. W., 1993, "*Turbomachinery Rotordynamics: Phenomenon, Modelling and Analysis*," Chapter 3, John Wiley & Sons, Inc, pp. 183-192.

[3] Nicholas, J., Gunter, E. J., and Allaire, P. E., 1979, "Stiffness And Damping Coefficients for the Five-Pad Tilting-Pad Bearing," ASLE Trans., **22**(2), pp. 113-124.

[4] Nicholas, J. C., 1994, "Tilting Pad Bearing Design - Tutorial," Proc. 23rd Turbomachinery Symposium, The Turbomachinery Laboratory, Texas A&M University, September 13-15, Dallas, TX, USA, pp. 179-194.

[5] Edney, S. L., 1995, "Pad Temperature in High Speed, Lightly Loaded Tilting-Pad Journal Bearings," Proc. 24th Turbomachinery Symposium, The Turbomachinery Laboratory, Texas A&M University, September 26-28, Houston, TX, USA, pp. 73-83.

[6] DeCamillo, S., and Brockwell, K., 2001, "A Study of Parameters that affect Pivoted Shoe Journal Bearing Performance in High-Speed Turbomachinery," Proc. 30th Turbomachinery Symposium, The Turbomachinery Laboratory, Texas A&M University, September 17-20, Houston, TX, USA, pp. 9-22.

[7] Nicholas, J., and Wygant, K. D., 1995, "Tilting Pad Journal Bearing Pivot Design For High Load Applications," Proc. 24th Turbomachinery Symposium, The Turbomachinery Laboratory, Texas A&M University, September 26-28, Houston, TX, USA, pp. 33-47.

[8] Al-Ghasem, A., 2004, "Measurement of Rotordynamic Coefficients for High Speed Flexure-Pivot Tilting-Pad Bearing (Load Between Pad) Configuration," M.S. Thesis, Texas A&M University, College Station, TX, USA.

[9] Rodriguez, L. E., 2004, "Experimental Frequency-Dependent Rotordynamic Coefficients for a Load-On-Pad, High-Speed, Flexible-Pivot Tilting-Pad Bearing," M.S. Thesis, Texas A&M University, College Station, TX, USA.

[10] DeCamillo, S., He, M., Cloud, C. H., and Byrne, J. M., 2008, "Journal Bearing Vibration and SSV Hash," Proc. 37th Turbomachinery Symposium, The

Turbomachinery Laboratory, Texas A&M University, September 7-11, Houston, TX, USA.

[11] Whalen, J. K., He, M., Cerny, V., and Polreich, V., 2015, "The Effects of Starvation on the Dynamic Properties of Tilting Pad Journal Bearings," Proc. 44th Turbomachinery Symposium, The Turbomachinery Laboratory, Texas A&M University, September 14-17, Houston, TX, USA.

[12] Abdollahi, B., 2017, "A Computational Model For Tilting Pad Journal Bearings: Accounting For Thermally Induced Pad Deformations and Improving a Feeding Groove Thermal Mixing Model," M.S. Thesis, Texas A&M University, College Station, TX, USA.

[13] Ha, H. C., and Yang, S. H., 1999, "Excitation Frequency Effects on the Stiffness and Damping Coefficients of a Five-Pad Tilting Pad Journal Bearing," ASME J. Tribol., **121**, pp. 517-522.

[14] Dmochowski, W., 2006, "Dynamic Properties of Tilting-Pad Journal Bearings: Experimental and Theoretical Investigation of Frequency Effects due to Pivot Flexibility," ASME J. Eng. Gas Turbines Power, **129**(3), pp. 865-869.

[15] Wilkes, J. C., and Childs, D. W., 2012, "Tilting Pad Journal Bearings—A Discussion on Stability Calculation, Frequency Dependence, and Pad and Pivot," ASME J. Eng. Gas Turbines Power, **134**(122508), pp. 1-17.

[16] San Andrés, L., and Tao, Y., 2013, "The Role of Pivot Stiffness on the Dynamic Force Coefficients on Tilting Pad Journal Bearings," ASME J. Eng. Gas Turbines Power, **135**(11), pp. 112505-112505-112511.

[17] San Andres, L., and Li, Y., 2015, "Effect of Pad Flexibility on the Performance of Tilting Pad Journal Bearings—Benchmarking a Predictive Model," ASME J. Eng. Gas Turbines Power, **137**(12), pp. 122503-122503-122515.

[18] Gaines, J. E., 2014, "Examining the Impact of Pad Flexibility on the Rotordynamic Coefficients of Rocker-Pivot-Pad Tilting-Pad Journal Bearings," M.S. Thesis, Texas A&M University, College Station, TX, USA.

[19] Harris, J. M., 2008, "Static Characteristics and Rotordynamic Coefficients of a Four-Pad Tilting-Pad Journal Bearing with Ball-In-Socket Pivots in Load-Between-Pad Configuration," M.S. Thesis, Texas A&M University, College Station, TX, USA.

[20] Wygant, K. D., Flack, R. D., and Barett, L. E., 1999, "Influence of Pad Pivot Friction on Tilting-Pad Journal Bearing Measurements—Part I: Steady Operating Position," Trib. Trans., **42**(1), pp. 210-215.

[21] Wygant, K. D., Flack, R. D., and Barett, L. E., 1999, "Influence of Pad Pivot Friction on Tilting-Pad Journal Bearing Measurements—Part II: Dynamic Coefficients," Trib. Trans., **42**(1), pp. 250-256.

[22] Pettinato, B., and DeChoudhury, P., 1999, "Test Results of Key and Spherical Pivot Five-Shoe Tilt Pad Journal Bearings-Part I: Performance Measurements," Trib. Trans., **42**(3), pp. 541-547.

[23] Pettinato, B., and DeChoudhury, P., 1999, "Test Results of Key and Spherical Pivot Five-Shoe Tilt Pad Journal Bearings-Part II: Dynamic Measurements," Trib. Trans., **42**(3), pp. 675-680.

[24] Delgado, A., Vannini, G., Ertas, B., Drexel, M., and Naldi, L., 2011, "Identification and Prediction of Force Coefficients in a Five-Pad and Four-Pad Tilting Pad Bearing for Load-On-Pad and Load-Between-Pad Configurations," ASME J. Eng. Gas Turbines Power, **133**(092503), pp. 1-9.

[25] Kukla, S., Hagemann, T., and Schwarze, H., 2013, "Measurement and Prediction of the Dynamic Characteristics of a Large Turbine Tilting-Pad Bearing Under High Circumferential Speeds," ASME Turbo Expo 2013: Turbine Technical Conference and Exposition, June 3-7, San Antonio, Texas, USA, Paper No. GT2013-95074, , pp. 1-12.

[26] Coghlan, D. M., and Childs, D. W., 2017, "Characteristics of a Spherical Seat TPJB with Four Methods of Directed Lubrication- Part 2: Rotordynamic Performance," ASME J. Eng. Gas Turbines Power, **139**(12), pp. 122503-122513.

[27] Coghlan, D. M., and Childs, D. W., 2017, "Characteristics of a Spherical Seat TPJB with Four Methods of Directed Lubrication- Part 1: Thermal and Static Performance," ASME J. Eng. Gas Turbines Power, **139**(12), pp. 1-13.

[28] Heshmat, H., and Pinkus, O., 1985, "Performance of Starved Journal Bearings With Oil Ring lubrication," ASME J Tribol-T, **107**, pp. 23-31.

[29] Tanaka, M., 1991, "Thermohydrodynamic Performance of a Tilting Pad Journal Bearing With Spot Lubrication," ASME J Tribol-T, **113**, pp. 615-619.

[30] Dmochowski, W., and Blair, B., 2006, "Effect of Oil Evacuation on the Static and Dynamic Properties of Tilting Pad Journal Bearings," Trib. Trans., **49**, pp. 536-544.

[31] Nichols, B. R., Fittro, R. L., and Goyne, C. P., 2017, "Subsynchronous Vibration Patterns Under Reduced Oil Supply Flow Rates," ASME Turbo Expo 2017: Turbomachinery Technical Conference and Exposition, June 26-30, Charlotte, NC, USA, Paper No. GT2017-65040, pp. 1-11.

[32] San Andrés, L., Koo, B., and Hemmi, M., 2017, "A Flow Starvation Model For Tilting Pad Journal Bearings and Evaluation of Frequency Response Functions: A Contribution Towards Understanding the Onset of Low Frequency Shaft Motions," ASME Turbo Expo 2017: Turbomachinery Technical Conference and Exposition, June 26-30, Charlotte, NC, USA, Paper No. GT2017-64822, pp. 1-15.

[33] Childs, D. W., and Hale, K., 1994, "A Test Apparatus and Facility to identify the Rotordynamic Coefficients of High-Speed Hydrostatic Bearings," ASME J. Tribol., **116**, pp. 337-343.

[34] San Andres, L., 2009, "Thermal Analysis of Finite Length Journal Bearings Including Fluid Inertia," Modern Lubrication Theory, Notes 07, Libraries Texas A&M University Repository, http://hdl.handle.net/1969.1/93247 [access date Jan. 4th, 2018].

[35] San Andres, L., 2010, "Static Load Performance of Plain Journal Bearings," Modern Lubrication Theory, Notes 04, Libraries Texas A&M University Repository, http://hdl.handle.net/1969.1/93244 [access date Jan. 29th, 2018].

[36] San Andres, L., 2009, "Annular Pressure (Damper) Seals," Modern Lubrication Theory, Notes 12(a), Libraries Texas A&M University Repository,http://hdl.handle.net/1969.1/93252 [access date Mar. 23rd, 2018].

APPENDIX A
UNCERTAINTY ANALYSIS

To measure the uncertainty of the complex dynamic stiffness (H_{ij}), the force excitation along each orthogonal direction is performed for 10 times (N) wherein each iteration includes 32 multi-frequency waveforms. The complex dynamic stiffness (h_{ij}) estimated for 10 shakes (N) at each excitation frequency is averaged and the twice of the standard deviation (σ) provides the uncertainty (ΔH) of the averaged complex dynamic stiffness (H_{ij}) with 95% confidence interval.

$$H_{ij} = \frac{1}{N}\sum_{k=1}^{N}(h_{ij})_k \tag{A.1}$$

$$\Delta H_{ij} = 2\,\sigma_{(H_{ij})} = 2\sqrt{\frac{\sum_{k=1}^{N}(h_{ij})_k - H_{ij}}{N-1}} \tag{A.2}$$

The uncertainties of the rotordynamic force coefficients is calculated as

$$\Delta m = t\sqrt{\frac{\hat{\sigma}^2}{S_{xx}}}\ \text{(uncertainty of slope)} \tag{A.3}$$

$$\Delta b = t\sqrt{\hat{\sigma}^2\left(\frac{1}{N}+\frac{\bar{x}^2}{S_{xx}}\right)}\ \text{(uncertainty of the intercept)} \tag{A.4}$$

$$S_{xx} = \sum_{k=1}^{N} x_k^2 - \bar{x}^2 \quad \text{And } \hat{\sigma}^2 = \frac{\sum_{k=1}^{N}(y_k - \bar{y}_i)^2}{N-2}$$

where S_{xx} is the sample mean, $\hat{\sigma}^2$ is the mean square error and t is the statistical variable (t=1.96 for large data set with a confidence interval of 95%).